APPROACHING EFFICIENT NANOMOTORS VIA BIOMIMICKING MECHANISMS

LIU MEIHAN

(B.Sc., JILIN UNIVERSITY)

A THESIS SUBMITTED

FOR THE DEGREE OF DOCTOR OF PHILOSOPHY

DEPARTMENT OF PHYSICS

NATIONAL UNIVERSITY OF SINGAPORE

2016

Declaration

I hereby declare that this thesis is my original work and it has been written by me in its entirety. I have duly acknowledged all the sources of information which have been used in the thesis.

This thesis has also not been submitted for any degree in any university previously.

Liu Meihan

20 January 2016

List of Publications

1. M. Liu et al., Autonomous Synergic Control of Nanomotors. *ACS Nano*. **8,** 1792–1803 (2014).

2. J. Cheng, S. Sreelatha, I. Y. Loh, M. Liu, Z. Wang, A bioinspired design principle for DNA nanomotors: Mechanics-mediated symmetry breaking and experimental demonstration. *Methods*. **67,** 227–233 (2014).

3. M. Liu et al., A bio-mimicking enzymatic nanowalker of high fuel efficiency. *Nano Lett*. under external review.

4. Nair et al., Stride-controlled dual direction of a nanowalker. submitted.

Acknowledgements

Frist and foremost, I would like to express my sincere gratitude to my advisor Prof. Wang Zhisong. His patient guidance and enthusiasm help me overcome the difficult times during my PhD study. He taught me a lot in scientific thinking and writing. It is a great fortunate to be his Ph.D. student; not only because of his guidance and support in research work, but also his constant sharing of knowledge and life experiences that are of great benefits to me. This thesis would not have been possible without his supervision and support.

I would like to thank Prof. Johan R.C. van der Maarel and Prof. Yan Jie for their valuable feedbacks during my qualification examination. I would like to thank my thesis examiners for their insightful comments and encouragement, and also the hard questions which incented me to widen my research from various perspectives.

My sincere thanks go to Dr. Hou Ruizheng, Dr. Cheng Juan, Dr. Loh Iong Ying and Tee Shern Ren for the many valuable discussions and practical advice that helped advance my research. Special thanks go to Dr. Cheng Juan and Dr. Loh Iong Ying for their encouragement and companionship throughout my Ph.D. study. I am very grateful to Dr. Srarangapani Sreelatha for her help

Last but not least, I would like to thank my beloved parents for supporting me in all my pursuits and my life in general.

Contents

Summary

Advances in nanotechnology necessitate nanomachines to perform a variety of tasks. Thriving multidisciplinary endeavours have been made to develop nanomachines that convert externally supplied energy into directional mechanical outputs such as force generation, translation, and rotation. How to control individual components of a machine to produce directional output of the machine as a whole remains an intriguing problem both scientifically and technologically. Nature has provided fabulous model systems from which we could learn from. Biological motor proteins play an essential role in a wide range of cellular functions; particularly noteworthy is the high energy efficiency they achieve. Biomimicking is an important strategy to advance the field of artificial nanomotors, which is the focus of this PhD study.

These biomotors often integrate a ratchet-like passive control and a power-stroke-like active control, and this synergic active-plus-passive control is critical to efficient utilization of energy. It remains a challenge to integrate the two differing types of control in rationally designed nanomotor systems. Recently a light-powered track-walking DNA nanomotor was developed from a bioinspired design principle that has the potential to integrate both controls. However, it is difficult to separate experimental signals for either control due

to a tight coupling of both controls. Here we present a systematic study of the motor and new derivatives using multiple fluorescence labelling and specially designed light operations. The experimental data suggest that the motor achieves the two controls autonomously through a mechanics-mediated symmetry breaking. This study presents an experimental validation for the bioinspired design principle of mechanical breaking of symmetry for synergic ratchet-plus-power stroke control. Augmented by mechanical modeling, this experimental study provides mechanistic insights that may help advance molecular control in future nanotechnological systems.

Replicating the efficient chemical energy utilization in biological molecular motors is a strategy to advance energy technology and nanotechnology. Here we report an artificial autonomous DNA nanowalker of a biomimetic design that achieves a fuel efficiency of less than two fuel molecules consumed per productive forward step, thereby breaking a general threshold for chemically-powered machines invented to date. Like its biological counterparts, this rationally designed nanowalker realizes multiple gating-like controls over the fuel reaction and mechanical motion, offering rich mechanistic insights into how pure physical effects enable effective harvest of chemical energy at the single-molecule level. As a genuine enzymatic nanomotor without changing itself nor the track, the walker demonstrates a sustained motion on an extended track at a speed comparable to burn-bridge motors. This opens the possibility of replicating the repeatable,

efficient and automatic cargo transportation seen in biological intracellular transport but beyond the capacity of current burn-bridge motors.

Table of Figures

Chapter 1 Introduction

1.1   Importance of nanomotors

Advances in nanotechnology necessitate nanomachines to perform a variety of tasks, from simple open/close switching operation and cargo transportation to sophisticated nanoscale manipulation and fabrication of a wide range of materials and products with molecular precision. The potential of nanomachines was recommended by K. Eric Dexler, who envisioned a "molecular assembler" to build objects with molecular precision in his 1986 book "Engine of Creation" (*1*) despite the later debate on technical feasibility of this molecular assembler (*2*). It is doubtless that the implementation and application of nanomachines can improve modern technologies.

Since early 1990s, thriving multidisciplinary endeavors have been made to turn single molecules into a machine that converts externally supplied energy into directional mechanical outputs such as force generation, translation, and rotation. Experimental success covers molecular shuttles (*3–6*) and rotors (*7–10*) in a localized setup, molecular walkers (*11–25*) running on open tracks, and larger systems that incorporated these "engines" for nanotechnological applications (*26–29*). The systems implementing these machines range from synthetic supramolecular compounds and engineered

biomolecules in aqueous environments to small molecules (*30*) on solid-state surfaces. The methods of energy supply include chemical fuels, fuels plus enzymes (*13–15*), light irradiation (*4–7, 20, 23–25*), and electric currents from a scanning tunneling microscope tip (*30*).

Although a variety of nanomachines have been developed, only a few can be exploited for real application. The development of nanomachine is still in its infancy, especially in the relatively new area of artificial nanomotors that are capable of converting energy into unidirectional and progressive movement along a linear track. However, these nanowalkers are being actively pursued for nanotechnological applications (*26–29*). Particularly noteworthy are recent studies (*28, 29*) that proves the feasibility of nanomotor-based multi-step chemical synthesis of organic molecules.

Artificial nanomotors are also inspired by cytoskeletal motor proteins from biology. Kinesin, myosin and dynein are the three families of motor proteins (hereafter biomotors) that are capable of moving directionally along cytoskeletal filaments (kinesins and dyneins move along microtubule, myosins on action filaments). They transport various cellular cargos and play an essential role in a wide range of cell functions such as cell division, vesicle and organelle transport and organelle synthesis (*31–34*). Dimeric biomotors, such as kinesin I and Myosin V, can walk considerable distance towards one end of their respective track before dissociation. These biomotors are unique considering that they directly convert chemical energy from ATP into

mechanical work, avoiding an intermediate such as heat and electrical energy as seen in macroscopic machines. It is noteworthy that kinesin I and myosin V can achieve efficiency ~60% and ~70% respectively, which compare favourably with 25%− 30% of gasoline engines powering a car. This is remarkable considering that they are working in the molecular world where random Brownian motion dominates the behaviour of molecules. Any directional movement in such an environment would be surprising, not to mention such a high efficiency. Biomotors achieve these superior performances by controlling individual constituent molecules so as to rectify directional outputs of a machine as a whole. Thus, we believe that previous studies on physical mechanisms of biomotors, especially kinesin I and myosin V which are relatively well studied among biomotors, can provide valuable information on the design of translational artificial nanomotors.

To date, artificial nanomotors implemented largely benefit from the theoretical studies on Brownian ratchet mechanisms (*35–41*) through which directional motion can be achieved. These nanomotors only represent characteristics of biomotors to a very limited degree and their performance is far poorer than biomotors'. By mimicking major mechanistic characters of biomotors we may have a chance of implementing efficient artificial nanomotor that is mechanistically advanced over the present ones. The implementation and systematic experimental study of such rationally designed biomimicking motors will contribute two pieces of new knowledge to the

scientific foundation of nanomotors. One is the general physical limits to nanomotor performance including directionality fidelity, speed and energy efficiency. The other is mechanistic solutions to realize the high performance. Both will advance the field of artificial nanomotors and associated technological applications and also improve our understanding of biomotors.

In the following sections, I will first review the biological studies of biomotors kinesin I and myosin V with a detailed discussion of their stepping mechanisms. Then the development of artificial nanomotors will be reviewed with a focus on DNA nanomotors. The major mechanistic characters of biomotors that should be considered to guide the design of efficient artificial nanomotors will be discussed. The last section presents the aim and framework of the thesis.

1.2   Biological motors

Underneath the superior performance of kinesin I and myosin V is the scientifically advanced walking mechanisms of these two biomotors. The walking mechanisms allow the motors to control its constituents properly to rectify the directional outputs of a machine as a whole. We may wonder how kinesin 1 and myosin V achieve directional processive movement by coordinating the actions of their two legs despite having two chemical identical legs. To answer the questions, we need to go into details about the walking mechanisms of the two biomotors.

Kinesin walks along the microtubule in a hand-over-hand manner (*42*). Its mechanical step is tightly coupled to the chemical cycle of ATP hydrolysis so that it consumes only one ATP molecule per step with its centroid moves 8 nm (*43–45*). Kinesin is capable of continuously moving (termed 'processivity') along the microtubule about 100 steps on average before derailing from the microtubule (*45–47*). Kinesin moves rapidly at speeds of 800 nm/s and above under saturate ATP concentration and zero load (*48–50*). Particularly, kinesin has high directionality as it exclusively walks towards the plus end of the microtubule (the periphery of the cell) under zero load with an average of one backward step in thousand forward steps (*51*). It can resist a back pulling force as large as 7 pN (*50–53*) with a maximum efficiency about 60% during a forward step near stall force (given by stall force×step size/energy from ATP hydrolysis, which releases energy of 62.5−90.8 pN·nm depending on solution condition (*54*)) at room temperature.

Kinesin achieves such superior performance by coordinating the mechanochemical cycles of its two heads through gating mechanisms. 'Gating' means a physically coordinated stalling of one motor leg in a specific mechanochemical state until a certain 'gatekeeper' process is completed – often at the other leg. Several gating mechanisms proposed have received experimental evidence. They are not mutually exclusive and kinesin may employ multiple gating mechanisms. Thus, I combine three experimental

supported gating mechanisms together to show a "consensus model'' (*55, 56*) in Figure 1.1b.

Kinesin is a homodimeric protein consists of two identical heads that function as the microtubule binding domain and catalytic domain (Figure 1.1a). The two heads are connected by two soft peptide chains called neck linker, which are connected to the coiled coil stalk formed by intertwining two identical heavy chains. The other end of the stalk connects to a tail that can bind cargos.

Gating I: The intramolecular strain accelerates rear head detachment (*53, 57–59*). For state ii in Figure 1.1b, ADP is bound to the tethered head of the motor with the other nucleotide-free head bound to the track. Experimental results suggest that the tethered head can weakly interact with the track to form the intermediate two-head-bound state (state i in Figure 1.1b) (*60, 61*). The neck-linker is stretched in state i, inducing certain strain in this region that may suffice to dissociate the ADP bound rear head from the track. This selective dissociation may be attributed to the stronger binding of the nucleotide-free head with the track than that of the ADP bound head (*51, 53, 60, 62*).

a. Kinesin structure
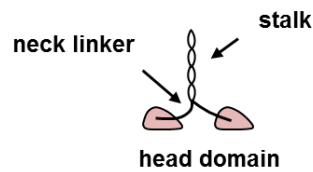
b. The mechanochemical cycle of kinesin-I

Figure 1.1 Schematic depiction of biomotor kinesin I. (a) The structural components of kinesin I. (b) The mechanochemical cycle of kinesin I. Microtubule is represented by the grey track. '+' and '−' denote the plus end and the minus end of the track. The molecular configuration of kinesin I for each state is illustrated together with bound nucleotides.

Gating II: ATP binding to the nucleotide-free front leg is inhibited through the intramolecular strain until the rear leg has detached from the track (*63–65*). Thus, ATP can only bind to the front leg in state ii since it is the only

unstrained state in the walking cycle. ATP binding releases significant energy and induces a conformational change to the neck-linker (red in state iii). This transition, termed neck-linker docking, immobilizes the neck liker onto the catalytic core and extends it towards the microtubule's plus end (*66*). The rear head then is placed perhaps 1~2nm (*56*, *66*) towards the plus end of the microtubule and the free energy change is favourable but small, about 3kJ/mol (~1.2 k_BT) (*67*). But this small docking biases the tethered head toward the plus-end of the microtubule and renders forward stepping energetically more favourable (energy barrier difference between forward and backward steps is ~6k_BT) (*56*, *62*, *68*), resulting in the diffusing head preferentially binding to the forward binding site.

Gating III: ADP release from the rear head is repressed until ATP binds to the front head (*56*, *60*, *69–71*). There is evidence that the ADP affinity for a kinesin head depends on the loading direction with rearward (against the direction of motility) tension decreasing the affinity and forward tension increasing that (*72*). After ATP binding, the ADP-bound head preferentially binds to the forward binding site and releases ADP under a backward tension, resulting in a stable two-headed binding to the microtubule (state iv). The internal strain (in state iv) again prevents premature binding of ATP to the front head before the rear head can hydrolyse its bound ATP. After ATP hydrolysis and phosphate release, one walking cycle completes and the centroid of kinesin moves 8nm toward the microtubule's plus end.

The three gatings combine to keep the enzyme cycles of the two feet out of phase with the enzyme cycle of the front leg delayed relative to that of the rear leg. This feature is called 'alternating catalysis' (*69, 70*), which is very necessary for achieving high processivity. It ensures that the two heads do not simultaneously assume a weak-binding conformation that induces premature dissociation and at least one head strongly binds to the microtubule during the walking cycle. Two key mechanisms are responsible for the unidirectional movement of kinesin. One is the selective dissociation of the weak binding rear leg (in ADP bound state i) through intramolecular strain. The other is the forward binding biased by the neck-linker zippering.

Hence, enzyme cycles of the two heads are tightly coupled to the stepping of the motor to achieve high processivity and directionality. The intramolecular strain, as the 'gatekeeper' for all the three gating mechanisms, is critical for coordinating the mechanochemical cycles of kinesin's two heads. In addition, there is growing evidence for neck-linker orientation-based gating mechanisms that contribute to keeping the two heads out-of-phase (*53, 60, 61, 71, 73*). When the neck linker is forward orientated, ATP hydrolysis is fast (*73*) and ADP release is inhibited (*60*). Conversely, when the neck-linker is rearward orientated, ATP hydrolysis is slow (*73*) and ADP release from the front head is facilitated (*60*). Furthermore, ATP binding to the leading head in state ii is inhibited where the neck linkers are separated (*61*). However, further

studies will be required to provide more experimental proof and to understand how neck-linker orientation affects the enzyme cycle.

Myosin V transports vesicles and organelles along actin filament toward periphery of the cells (plus end of actin filament) (*74–76*). It moves by taking 36nm (*74, 75, 77–81*) steps in hand-over-hand (*82, 83*) manner. The tight mechanochemical coupling in myosin is also demonstrated that ensures one ATP is hydrolysed per step (*74, 75, 77, 80*). Myosin V is a processive motor as it can travel ~2µm on average before dissociating from the actin filament (*74, 75, 80, 84*). Under saturating ATP concentrations and low loads (<1pN), the velocity is about 400nm/s (*74, 78, 84*). Myosin V can reach more than 70% energy conversion efficiency during a forward step near stall force, which is 2-3pN (*74, 75, 77–79, 81*).

As shown in Figure 1.2a, myosin V has two identical head domains responsible for ATP hydrolysis and actin binding. Each head domain is linked to the coiled coil domain via a lever arm, which consists of six IQ motifs in tandem is stiffened by six light chains bound to it. The coiled-coil domain further connects to the cargo binding domain which is not shown. Unlike the soft neck linker of kinesin I, the lever arm of myosin is relatively stiff. The mechanochemical cycle that is consistent with the current findings is illustrated in Figure 1.2b.

a. Myosin V structure
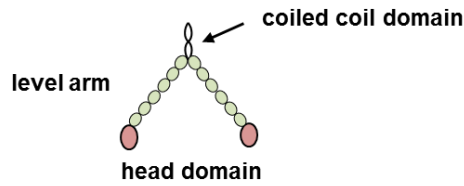
b. The mechanochemical cycle of myosin V

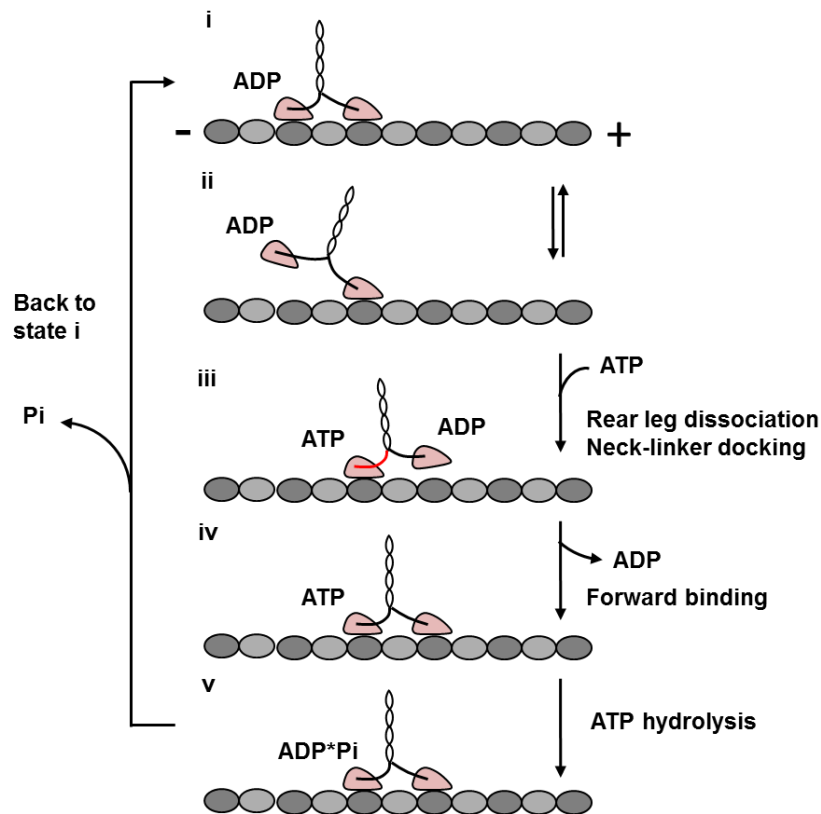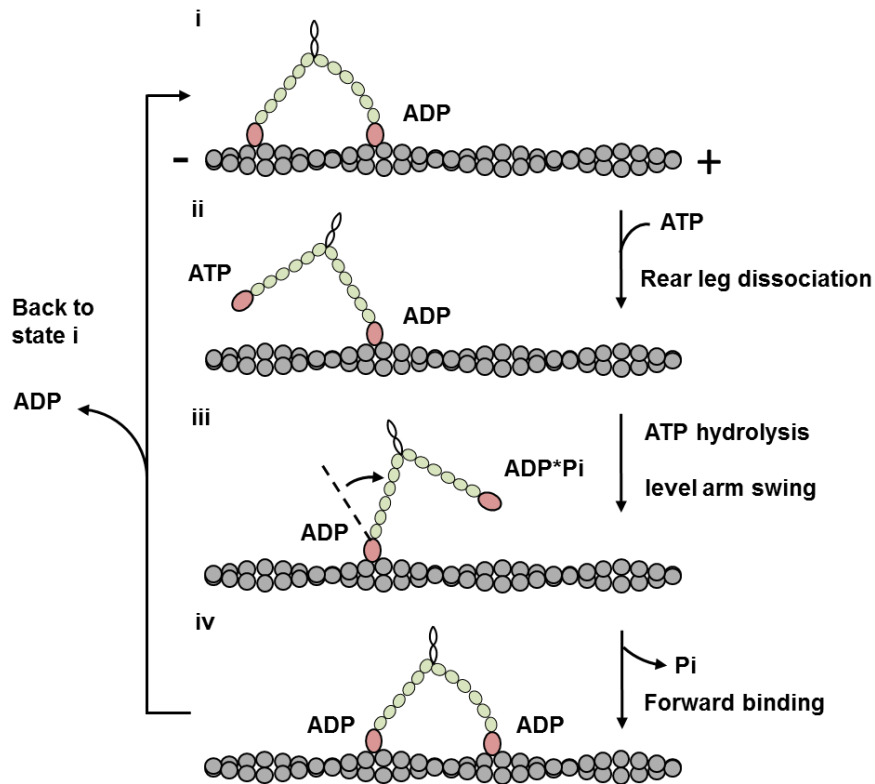**Figure 1.2 Schematic depiction of biomotor myosin V.** (a) The structural components of myosin V. (b) The mechanochemical cycle of myosin V. Actin filament is represented by the grey track. '+' and '−' denote the plus end and the minus end of the track. The molecular configuration of myosin V for each state is illustrated together with bound nucleotides.

ATP can only bind to the nucleotide-free rear head in state i and cause its detachment from the actin filament. The leading lever arm can now swing forward and move the myosin center of mass forward 20-25 nm (state ii) (*75, 76, 78, 79, 81, 85–87*). This swing step is energetically favorable (*81*) and

binding of the ADP-bound head to the actin filament is stronger in the post-swing state (*81*, *86*, *88*). This swing step renders the backward actin binding site less accessible to the mobile head. Therefore, the ATP-bound head preferentially binds to the forward binding site after diffusive search. The phosphate is quickly released upon binding of the diffusing head (state iii). ADP release from the rear head is the rate-limiting process as found by experiments (*75–77*, *89*). After this process, myosin V completes a forward step and is ready for the next ATP binding (state iv).

The intramolecular strain regulates and coordinates the mechanochemical cycles of the motor's two heads. Studies have proven that the intramolecular strain mainly retards ADP release of the lead head (*76*, *77*, *81*, *84*, *88*, *90–92*). This provides an efficient gating to ensure that the lead head is not able to bind to ATP until the rear head detaches. This gating makes great contribution to the high processivity and directionality of the motor as it suppresses motor derailment and produces selective rear head dissociation by inhibiting premature ATP binding to the lead head.

The detailed atomic mechanisms for the double-way coupling of the mechanical and chemical cycle of biomotors are largely mysterious. Nevertheless, existing experimental and theoretical studies on biomotors have provided valuable information to guide the design of artificial nanomotors as will be discussed in the following section.

1.3 Artificial nanomotors

Artificial track-walking nanomotors that mimic the behaviours of biological motor proteins are pursued in recent years, which mostly are built from DNA (*11–18*, *21–28*, *55*, *93–108*) with a few exceptions based on synthetic supramolecules (*19*, *20*, *109*). Readers who are interested in synthetic small molecule motors can consult the latest reviews (*110–113*). DNA serves as a good molecular building block for fabricating nanomotors. The base sequences of oligonucleotides encode structural information; this sequence-structure relation enables building of DNA nanomotors by self-assembly. Two complementary sequences form a duplex through base pairing and other specific sequences are able to form triplex or quadruplex structures under certain environments. For example, C-rich sequences can self-assemble into i-motif at acid pH (*114*, *115*) and G-rich sequences into G-quadruplex stabilized by monocations (*116*, *117*). The formation and breaking of these DNA secondary structures can be controlled by various methods: temperature, fuel strand displacement, enzymatic reactions, light irradiation and salt and ions in the solution, and so on. The simplicity of structures and extensively studied DNA mechanics, kinetics and thermodynamics allow us to program DNA assembly and reactions through sequence selection. This DNA nanotechnology has been used to devise different nanomotors that perform various tasks, like transportation (*101*, *102*), cargo capture/release (*26*) and

other robotic behaviours (*21*, *27*), sensing (*95*), autonomous programmed organic synthesis (*28*).

In the following subsections, the development of DNA nanomotors are reviewed and categorized according to mechanism sophistication. Advantages and disadvantages of each type of motor design are discussed.

1.3.1 Non-autonomous burn-bridge nanomotors

In 2004, Shernman and Seeman reported a non-autonomous nanomotor that moves in inchworm gait (*11*), as shown in Figure 1.3a. In the same year, Shin and Pierce reported a DNA motor similar in principle but walking in hand-over-hand gait (see Figure 1.3b), which is exactly how kinesin and myosin walks (*12*). Both motors employ a mechanism that solely depends on the specific base-pairing of DNA. The sequences of motor's two feet are different from each other and so are the footholds. These motors may be classified as burn-bridge motors because their backward motion is prevented by denying the anchor strand for the passed binding site. The difference between the two kinds of walking gait is that one foot is always leading the other one in inchworm gait. In hand-over-hand gait, the two feet exchange leading role once the motor takes a step.
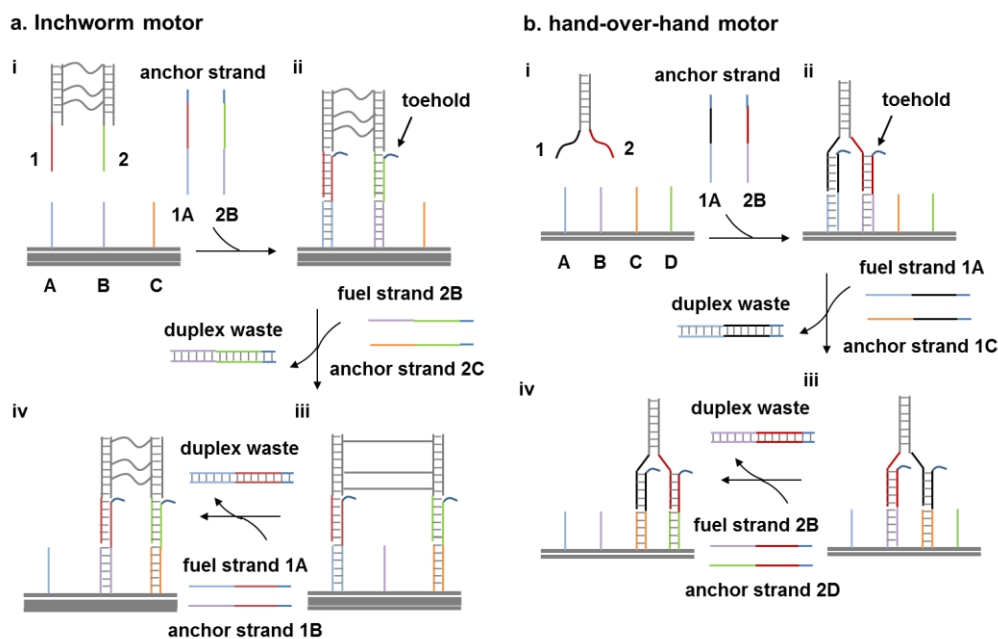
Figure 1.3 Non-autonomous nanomotors with different gaits. (a) An inchworm motor reported by Shernman and Seeman (*11*). (b) A hand-over-hand motor reported by Shin and Pierce (*12*). Initially either motor connects to the track through anchor strands (from state i to state ii) and each anchor strand is complementary to a specific foot/foothold pair. The motor's movement is triggered by adding a fuel strand 1A for hand-over-hand motor (or 2B for inchworm motor), which binds to the unpaired toehold region of anchor strand 1A (or 2B) and dissociates it from the motor foot 1 (or 2) through toehold-mediated strand displacement (*118, 119*). Then the freely foot can bind to the next foothold C through anchor strand 1C (or 2C) (state iii). Repetition of fuel strand and anchor strand addition moves the motor further down the track. Matching colours indicate complementary sequences; lines indicate base pairing instead of a particular number of bases.

Based on the motor developed by Shin and Pierce, a similar bipedal walker and its walking on a DNA origami track were demonstrated by Tomov et al. in 2013 (*96*). The mechanisms of the walker's operation were systematically studied. It was found that only 1% of the motors operated as intended (defined as the operation yield) after six consecutive steps down the track. It was also found that the operation yield decreases as the anchor strand concentration increases. This is attributed to the existence of an undesirable

trap state in which both the motor's mobile foot and the target foothold bind to an anchor strand (as indicated by red arrow in Figure 1.4), inhibiting either anchor strand from completing the reaction. This problem is solved by using a hairpin-anchor strand which binds to the motor leg and the foothold in different rates. The sequences that can bind to the motor leg are placed either inside the hairpin loop or the duplex stem. This leg-anchor binding remains unavailable until the stem is opened upon hybridization of the hairpin-anchor with the foothold. The operation yield was increased to 74% for motors operating with the hairpin-anchor, which is a dramatic improvement considering the merely 1% observed for motors operating with the non-hairpin anchor. This study also showed the possibility of improving motor speed by increasing the concentrations of the hairpin-anchor and fuel without lowering the operation yield. Another strategy to speed up this kind of motor is achieved by using DNA catalyst that accelerates the leg binding to the foothold (*97*). These two studies demonstrate that the motor performance could be improved greatly by regulating the reaction rates properly.

The hairpin-anchor design was applied in a recently study performed by the same research group, in which a similar bipedal walker strides back and forth between two DNA origami tiles (*98*). The operation yield is similar to that of the motor operating on a single origami tile, which indicates no significant dissociation while travelling between tiles. Hence, this result implicates the potential of realizing a bipedal walker that can moves

micrometer-long distance. Besides bipedal walkers, Gu et el. (2010) developed

a tripedal DNA molecular robot that can assemble three different cargos,

whose availability are controlled by three DNA machines respectively (*26*).

This robot can collect cargos while moving on an origami track from one

DNA machine to the next one.
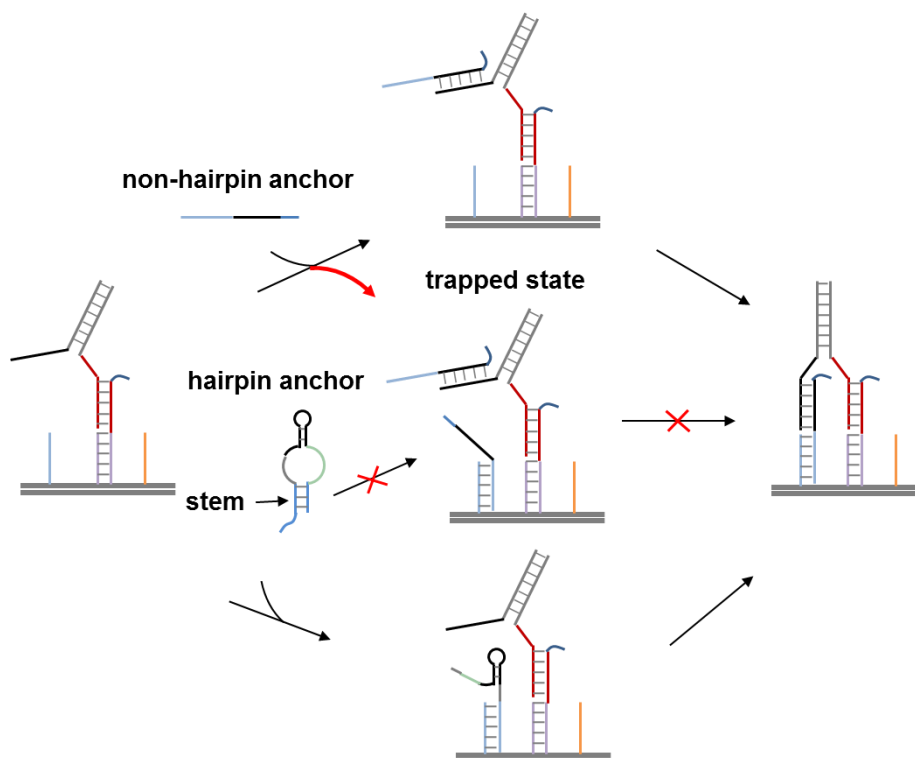
Figure 1.4 A proposed mechanism for optimizing motor operation yield by using a hairpin anchor.

Another non-autonomous DNA motor was reported by Wang et al.

(*99*). Upon changing of the pH or ions in the solution, the relative binding

strength to different footholds are changed correspondingly. The motor moves

its feet by forming a more stable binding with the next adjacent foothold

compared with the previous one. The operation and direction of every step of the motor can be controlled.

Motor systems fuelled solely by DNA strands provides superior controllability considering that every step of the motor can be manually controlled and the direction of movement can be simply reversed by rearranging the order to apply the anchor and fuel strands. In principle, these motors can travel a long distance. However, more and more anchor and fuel strands are going to be introduced into the solution as the motor moves forward. This complicates the walking environment to increase the probability of mismatching among DNA strands. This can lower the operation yield of these motors systems and thus limit the run length of the motors. Extra procedures to remove side products (*17*) may be introduced to address this problem in principle.

1.3.2 Autonomous burn-bridge nanomotors

An autonomous DNA nanomotor was reported by Yin et al. in 2004 (*13*). This motor moves two steps along a DNA track through alternating ligation and cleavage of DNA strands. Each step is achieved by first ligating the motor to the next site, and then cutting it from the previous site by a restriction enzyme. The energy is supplied by ATP hydrolysis of the restriction enzyme. This motor migrates directionally and cannot step backwards because the passed sites were 'burnt' by the motor.

a. Nicking enzyme mediated motor

b. DNAzyme motor

i

toehold

ii

foothold cleavage
product

iii

iv
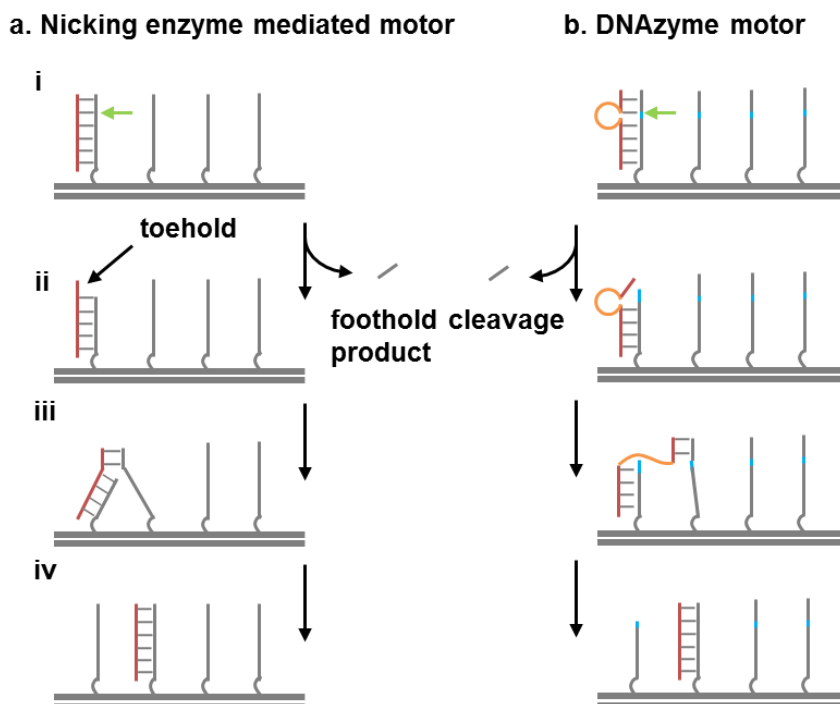
Figure 1.5 Autonomous enzyme-mediated nanomotors. (a) Reaction cascade of the motor developed by Bath et al. (*14*). The nicking enzyme N.BbvC IB recognizes the specific 7 bp sequence of the DNA duplex formed by motor-foothold binding (state i). The enzyme can then catalyse the hydrolysis of the foothold strand, which leads to the dissociation of the short fragment of the foothold since its melting temperature is well below the operating temperature of the motor (state ii). The toehold region thus exposed upon fragment release can reach the next foothold and hybridizes with it since the binding with the intact foothold is more stable (from state iii to state iv). Repeating this process, the motor can migrate to the end of the track. (b) Reaction cascade of the DNAzyme motor developed by Tian et al. (*15*). Recognition sites for nicking enzyme/DNAzyme are indicated by green arrow. Lines indicate base pairing instead of a particular number of bases.

Later in 2005, two reports (*14, 15*) of autonomous DNA motors appeared in the literature as presented in Figure 1.5. Both are single-foot motors powered by the energy extracted from cleavage of the footholds. The motor developed by Bath et al is estimated to move at a speed of ~0.1nm/s (*14*). This design has been applied in a molecular transport system later by the same research group (*22*). They observed the autonomous and consecutive

stepwise movement of the DNA motor using real-time, high-speed AFM. The motor completed 16 continuous steps along the full length of the track, which is ~100 nm long, at a speed comparable with the previously determined value.

Another conceptually similar autonomous motor was reported by Tian et al. (*15*). The motor is a DNAzyme capable of cleaving RNA strands with sequence specificity. Therefore, the sequence recognition and the foothold cleavage can be accomplished by the motor itself. The reaction cascade is shown in Figure 1.5b. This design was adapted for the development of a molecular 'spider', which is composed of three single-stranded DNAzyme legs connected to an inert streptavidin core and one loading arm (*27, 100*). This arm is used to position the spider precisely on the 'start' position of the origami track. Upon activated by a trigger strand that releases the arm, the spider is able to move towards the area rich in intact footholds and leaves cleaved footholds behind it. The spider achieves directional movement up to 100 nm at a speed of ~0.05 nm/s. In addition, the movement trajectory is predefined with instructions, such as 'follow', 'turn', and 'stop', incorporated in the track design. Hence, the spider shows elementary robotic behaviours by executing these instructions.

Transportation over micrometre-long distance of a nanomotor based on RNA-cleaving DNA enzyme was reported by Cha et al. (*101*) in 2014. The motor is observed to transport CdS nanocrystal unidirectionally along single-walled carbon nanotubue over 3µm. The maximum speed measured is ~0.1

nm/s, which is similar to the speeds of other enzyme mediated DNA nanomotors (*14*, *22*, *27*, *95*). A detailed study of the DNAzyme-based walker (*102*) reports the dependences of the walker's translocation kinetics and processivity on several key parameters. These parameters include catalytic core variations, recognition arm lengths, and divalent metal cation species and concentration. With the knowledge of the influence of these key parameters, they successfully selected a DZ7 enzyme walker that moves about 5µm along a carbon nanotube track with an average speed of ~1 nm/s. This speed is so far the highest speed achieved by DNA nanomotors.

Achieving long-range transportation is not the only reason for developing artificial nanomotors. One of the long-term goals is to use the motor to manufacture molecules and even machines precisely at molecular level. An autonomous DNA walker capable of performing a series of amine acylation reactions while stepping along a DNA track was demonstrated by He and Liu in 2010 (*28*), as shown in Figure 1.6. It is noteworthy that this multistep synthesis is completed in a single isothermal solution in a sharp contrast to the present chemical industry in which multistep synthesis often proceeds in multiple reaction vessels that each contains a different set of reactants.
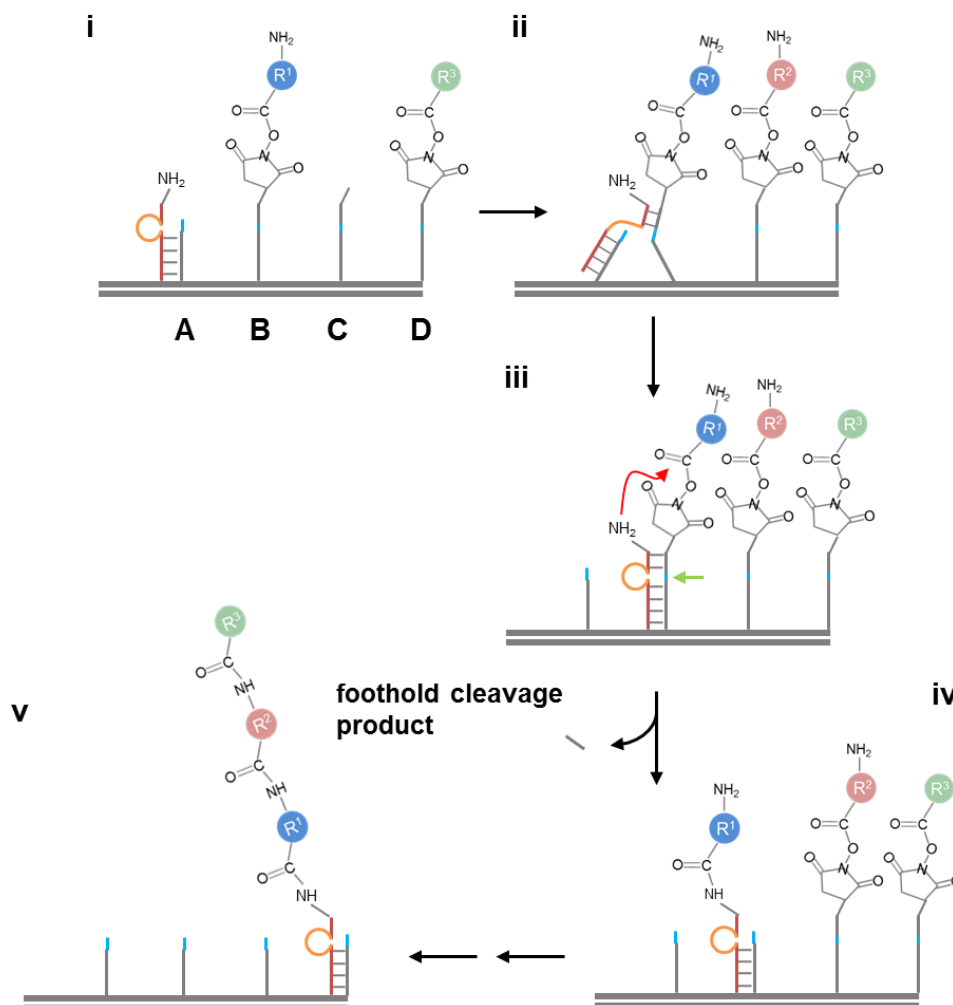
Figure 1.6 An autonomous DNA walker capable of performing a series of amine acylation reactions. (Figure adapted from ref. (*28*)). The walker carries an amine group and each foothold is attached with an amino acid NHS ester. The walker contains a 10-23 DNAzyme and migrates in the same way as the motor shown in Figure 1.5b. While moving forward, the walker brings the amine group to the vicinity of the NHS ester (state ii) and enables amine acylation reaction that transfers the amine acid building block from site B to the walker (from state iii to state iv). Repeating two more such cycles results in the synthesis of a triamide attached to the fourth foothold through the walker (state v). Detailed chemical structures of R1, R2 and R3 are omitted for clarity.

Besides the above discussed enzyme-mediated motors, an autonomous and controllable light-driven DNA motor was reported by You et al. in 2012 (*23*). The construction of motor and track and the reaction cascade are similar

to that of the motor presented in Figure 1.5b. A pyrene moiety is incorporated into the DNAzyme analogue motor, which can facilitate photolysis of the disulfide bond within the footholds upon light irradiation. Once the disulfide bond is cleaved, the short upper foothold fragment dissociates and the motor can search for the next intact foothold. It was demonstrated that movement of the motor can be regulated by light; more repaid movement was observed with increasing light intensity and the motor stopped if no light irradiation was applied. In contrast to enzyme mediated motors, the motor movement can be controlled externally by changing the intensity of light. Later in 2015, direct visualization of the movement of a similar motor on a DNA origami track using high-speed AFM is reported *(103)*.

These motors discussed above move via enzyme catalysed hydrolysis or photolysis of the backbone of the foothold. Another type of autonomous motors is powered solely by DNA hybridization which is catalyzed by the motor. Such a motor was implemented by Yin et al. (*104*). The system design and reaction cascade are depicted in Figure 1.7. The hairpin fuel is complementary to the binding site; however, their hybridization is inactivated by constraining complementary domains in the secondary structures, for example, in a double strand or in a hairpin loop (*120–122*). The motor plays the role of a catalyst that catalyzes the hybridization reaction by making the binding site accessible to the fuel strand. However, this motor system lacks of leg coordination as the motor's two legs can be displaced from the track

simultaneously. In order to achieve directional and processive movement, physical mechanisms need to be introduced to break directional symmetry and coordinate the two legs of the motor.
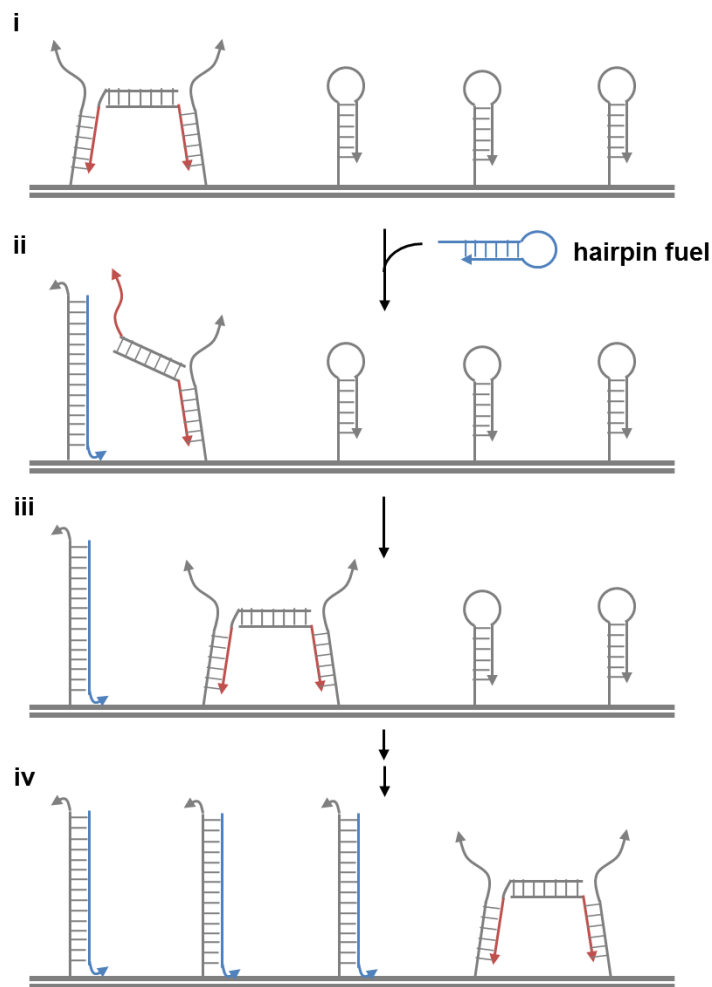
Figure 1.7 Locomotion of a homo-bipedal DNA motor without leg coordination. (Figure adapted from ref. (*104*)). The motor has two identical legs that each can bind to the toehold region of one binding site and form a duplex with it through toehold mediated stand displacement (state i). The hairpin fuel can now hybridize with the foothold and displace the motor leg (state ii). The 3' end of each strand is represented by arrow.

24

This problem was solved later by Omabegho et al. (*17*), who reported an improved hetero-bipedal motor that coordinates the action of its two legs by cyclically catalysing the hybridization of the metastable DNA fuel strands with the footholds. There are two types of fuel strands that each can hybridize with one motor leg. The binding of the motor to the track exposes a code strand on the track that can only binds to the specific fuel strand that dissociates the rear leg of the motor from the foothold. The mobile rear leg can now bind forward, which exposes a new code strand to enable the detachment of the other leg. The dissociation of the entire motor is prevented through a topological gating that renders a premature fuel binding sterically undesirable. It was demonstrated that the motor achieves autonomous and directional movement along a DNA track. In contrast to the above reviewed autonomous burn-bridge motors that can go either way if given the choice, this motor can choose the walking direction. Moreover, the motor design differs from previous ones in the realization of leg coordination and intrinsic direction. The assembly and operation of this motor were later further verified by using sm-FRET-ALEX technique which provides detailed structural dynamic information of this motor system (*105*).

A programmable DNA molecular robot that moves DNA cargos along a branched track has recently been described by Muscat et al. (*21*). The direction of the cargo can be controlled by the instructions encoded in the DNA fuel hairpins. Similar with the above DNA hybridization powered

25

motors, an autonomous reaction cycle is achieved by sequentially revealing the toeholds that initiate the subsequent reactions in the cycle. It was later demonstrated (*106*) by the same research group that the route taken by the cargo at the junction of a branched track can be controlled using a signalling molecule (adenosine) to induce blocking and unblocking of the branches of the track.

1.3.3 Autonomous motors beyond burn-bridge design

The autonomous track-walking nanomotors discussed so far rely on burn-bridge methods; the back-stepping of these burn-bridge motors are avoided by damaging or modifying the footholds behind the motor by enzyme cutting or DNA hybridization. The problem with this scenario is that repeat use of the track is either impossible or requires a non-trivial reset operation. However, biomotors can walk on their tracks repeatedly without destroying them. This would be a desirable feature too for artificial nanomotors and their technological applications.
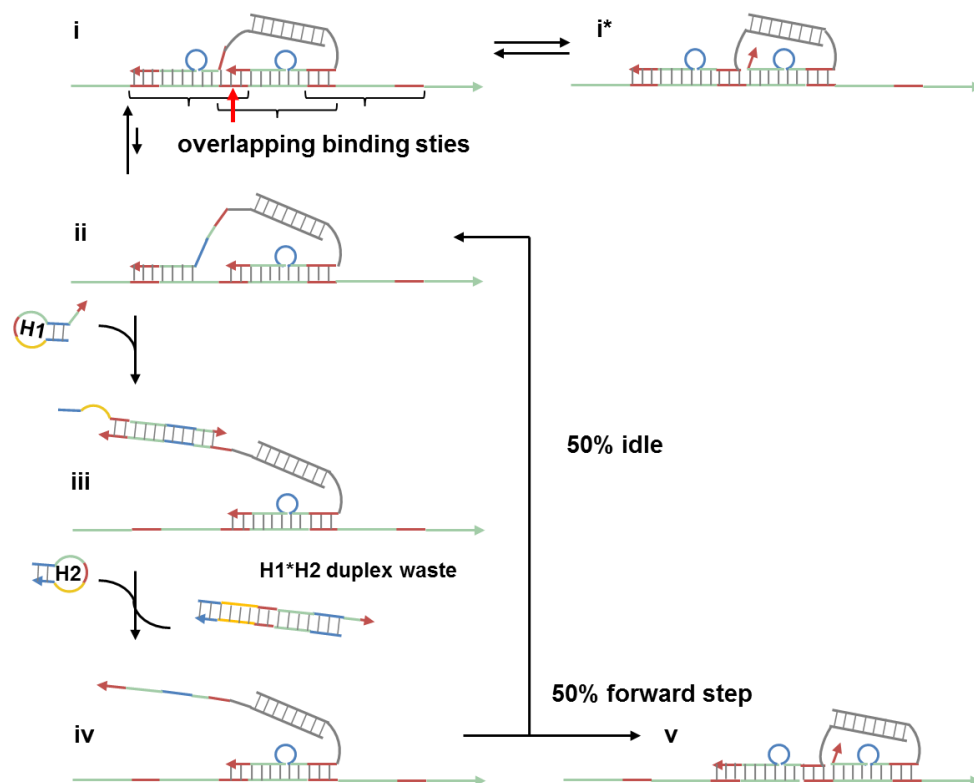
Figure 1.8 An autonomous homo-bipedal motor with coordinated legs. (Figure adapted from ref. (*16*)). Transition from state i to state ii is caused by the spontaneous dissociation of the short fragment (shown in green, 4nt for the left leg in state i versus 8nt for the right leg in state i*) next to the overlapping domain. The 3' end of each strand is represented by arrow. Matching colours indicate complementary sequences; lines indicating base pairing instead of a particular number of bases.

In 2008, Green et al. proposed and demonstrated the first design of autonomous DNA motor possessing this feature (*16*). The operation cycle of this motor is depicted in Figure 1.8. The track consists of one single-stranded DNA that features overlapping binding sites (indicated by the brackets in Figure 1.8). The motor has two identical legs that compete on binding to the overlapped domain (indicated by the red arrow in Figure 1.8). The mutually exclusive binding results in two asymmetrical ground states (state i and state i*) in which the toehold domain of either rear or front leg is exposed. This

provides discrimination between the two identical legs according to their positions so that the rear leg reacts with the fuel at a higher rate than the front leg. Hence, the hairpin fuel H1 preferentially binds to the exposed toehold of the rear leg and dissociates it from the track (state iii). Then hairpin H2 can hybridize with H1 to form a stable waste product (the H1*H2 duplex). The leg is now released and can bind to the forward or backward binding site with equal probability, which results in an idle step or a forward step (state v) correspondingly. Therefore, the motor moves forward by average. Later, the same research group reported a mechanistic similar motor powered by DNA hydrolysis (*18*).

In these motors systems, a leg competition breaks the symmetry to achieve an asymmetry equilibrium state, which results in different reaction rates of fuel strands with the two identical legs in the asymmetry state. Leg coordination and directional movement are thus achieved. In contrast, the homo-bipedal motor reported by Yin et al. (*104*) lacks of leg coordination and has no intrinsic directionality because of the symmetric equilibrium state in which the fuel strand cannot discriminate between two identical legs. However, for the motors reported by Turberfield's group (*16, 18*), only 50% of fuel molecules consumed lead to successful forward steps at best. This limitation imposes a threshold to the efficiency of this motor since at least two fuels need to be consumed to produce a forward step on average. The motor's efficiency was estimated to be ~9% (*16*).

How to promote forward stepping is an important problem in the development of nanomotors in general. To tackle this problem, two novel design principles have been derived (*62*, *86*, *123*) from biological motors and experimentally demonstrated (*24*, *25*, *107*, *108*) by the lab where the PhD study is based. The first design principle was proposed (*123*) by Wang in 2007. Its first experimental implementation was reported in 2012 in a light-driven DNA homo-bipedal walker by Juan et al. (*24*). This motor and its underlying design principle will be discussed in detail later in this thesis. The second design principle was proposed and experimentally demonstrated by in 2014 by Loh et al. (*25*), leading to a new light-driven DNA homo-bipedal nanowalker as illustrated in Figure 1.9. The walker has a modular design in which the motor's two legs are separated from the energy-consuming 'engine' part. The modular design allows flexible implementation with a wide variety of bi-state molecular switches, potentially leading to many new motors of varying performance. This modular design also has an advantage for long run length considering that the engine cannot affect the track-bound leg anymore after the other leg's dissociation and at least one motor leg remains bound to the track during motor movement.
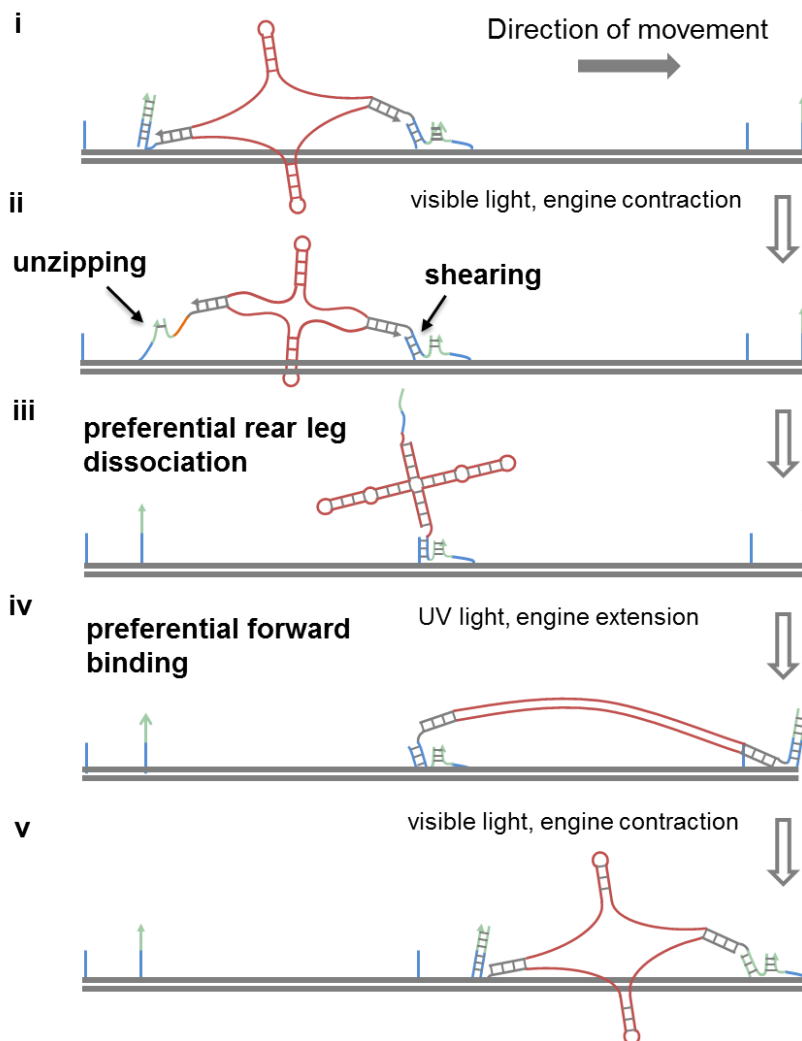
Figure 1.9 Operation of a light-driven DNA walker implementing a modular design. (Figure adapted from ref. (*25*)). The walker has a modular design in which the motor's two legs are separated from the energy-consuming 'engine' part, namely the azo-embedded double hairpin capable of light-induced extension and contraction under UV and visible light respectively. When a visible irradiation shrinks the motor, a base-by-base unzipping occurs at the rear leg versus shearing of multiple base pairs at the front leg (state ii). Hence, the pulling preferentially dissociates rear leg (state iii). Under UV irradiation, the motor extends and the dissociated rear leg preferred forward binding (state iv).

1.3.4 Mechanism integration is essential for efficient utilization of energy

Control is a hallmark of machines; effective control over a nanoscale system is necessary to turn it into a nanomachine. Two basic controls have been identified. One is a ratchet-like control (*36–38*, *62*, *71*, *123*, *124*) (termed selective dissociation bias in this thesis) that rectifies a machine's output toward a chosen direction by blocking stochastic molecular transitions conducive to the oppositely directed output. The other is power-stroke-like control (*10*, *32*, *38*, *62*, *123–126*) (termed forward binding bias in this thesis) that promotes forward stepping of a dissociated leg over backward stepping. A forward binding bias is often termed power stroke (*32*, *38*, *127*) if the bias is caused by a force-generating process associated with the energy injection/fuel consumption that directly drives the forward output as an energetically downhill transition (e.g., see a review by Vale and Milligan (*32*) in which the term "power stroke" is used to describe the neck-linker zippering in kinesin I and level arm swing in myosin). We note that the forward binding bias can be caused by a mechanism that does not necessarily involve apparent force generation. In this situation, the bias might not be qualified as "power stroke" in the strictest sense.

Artificial nanomotors developed so far have successfully implemented selective dissociation bias, but lack of forward binding bias between identical binding sites on a track. In contrast, biomotors kinesin I and myosin V achieve

directional movement by integrating the two controls. This mechanism integration is essential in achieving high directionality (or directional fidelity) as found in a recent study (*127*). Directionality (D) is introduced as a measure of the fidelity of a nanomotor's self-propelled motion towards the forward direction over backward and futile motion. Specifically, D is defined as the net probability for a forward displacement along the track per event of energy consumption. They found that D also reflects the level of advancement of a motor's inner design/working principles, which in turn determine the motor's performance. Based on the experimental results, they concluded that some biomotors achieve D > 99%, for example, $D_{max} \approx 99.5\%$ for kinesin I (*127–129*). However, either control alone cannot achieve more than 50% directionality, although either control alone is able to rectify a net directional stepping in an average sense.

Previous studies (*128*, *129*) found that the 2nd law of thermodynamics requires a least energy price for directional fidelity of isothermal nanomotors. A biomotor with ~ 100% efficiency evidently (*128*, *129*) exhausts the chemical energy to produce high directional fidelity at the 2nd law decreed least price, with the chemical energy-to-work conversion resulting from load-reduced direction. Hence a vital capability of efficient nanomotors is the effective channelling of the fuel energy into directional fidelity, which can be achieved mechanistically via complementary dissociation and binding biases.

1.4 Objectives of the study

This thesis focuses on developing and studying artificial track-walking nanomotors integrating both ratchet-like and power stroke-like controls, which is essential for achieving high directionality and high energy efficiency.

However, it is difficult to separate experimental signals for either control due to a tight coupling of both controls. This thesis presents a systematic study of a light-driven motor and its new derivatives using multiple fluorescence labelling and specially designed light operations. The results provide evidence for the existence of the two controls and demonstrate the design principle. This experimental study provides advanced motor candidates for further optimization and development and offers valuable mechanistic insights that help advance molecular control in future nanotechnological systems.

In the second part of this thesis, an autonomous DNA nanowalker is developed from a biomimietic design. This motor replicates some key features of the efficient chemical energy utilization in biological molecular motors, and thereby breaks two-fuel-per-step threshold for chemically-powered machines invented to date, and facilitate sustainable and repeatable autonomous motion beyond the capability of burn-bridge motors. This biomimetic system may thus provide an access to the science governing efficient chemical energy utilization at a single-molecule level, which is important to nanotechnology

and energy technology but remains difficult to decipher from the complex bio-systems.

1.5 Overview of the thesis

Chapter One of the thesis reviews biomotors kinesin I and myosin V with their stepping mechanisms presented in details after briefly stating the importance of artificial nanomotors in nanotechnology. The artificial nanomotors developed to date are also reviewed with a focus on DNA track-walking nanomotors and its applications. These DNA motors are categorized according to their levels of mechanistic sophistication. The mechanistic characters of biomotors that should be considered on devising efficient artificial nanomotor are discussed. At last, the aim and framework of the thesis are outlined.

Chapter Two presents the materials and methods used in this study, including DNA sequences design, methods for fabrication and verification of DNA motors and tracks, and methods for characterizing motor operation. More details on the materials and methods specifically for each study are described in the Materials and Methods section of the corresponding chapters.

Chapter Three presents the first part of this PhD study, namely a systematic study of a light-driven motor and its new derivatives. Chapter Four presents the second part of this PhD study, which is about the development of

a biomimicking enzymatic nanomotor. In each chapter, the design and operation of the motor-track system, its experimental results and data analysis methods are included.

Chapter Five concludes the studies. Limitations and recommendation for further studies are discussed.

Chapter 2 Materials and Methods

2.1   DNA sequence design

The nucleotide sequences for the double-stranded backbone of tracks were taken from lambda DNA; the sequences for the motor and other parts of the tracks were generated using CANADA software (*130*). The secondary structures were checked using Mfold (*131*) (for single strands) and NUPACK (*132*) (for motor/track formation), with unwanted structures removed by manually adjusting the sequences.

We design the track in a way similar to DNA origami: a long single strand DNA (ssDNA) selected from lambda DNA serves as the template, and several short ssDNAs partially form duplex with the template to produce the duplex track with single-stranded overhangs. On selecting the long template sequence from lambda DNA, several constrains are imposed to reduce undesired secondary structures and enhance track rigidity. For example, sequences containing GGGGG should be avoided because such sequence may form G-quardruplex. In addition, GC content is important for track rigidity and stability. G-C base pair is stronger as it is held together by three hydrogen bonds compare with two for A-T base pair. Therefore, DNA duplex with a high GC content is often more stable than that with a high AT content. Many

DNA library searches require each strand to have a 50% GC-content to balance the requirement of stable matched hybridizations for identification purposes with the requirements of denaturation (*133*). Hence, GC content for the track templates selected for this PhD study varies between 50% and 55%.

The secondary structures and thermodynamics details of the selected sequences were predicted by using Mfold web server (*131*), which is based on a dynamic programming algorithm. The computation time is within 15 seconds for the sequences used for this PhD study. In this method, a single strand is presented as a semicircle with its nucleotides equally spaced on the semicircle (*134*). The nucleotides, base pairs (G-C and A-T hydrogen bonds) and base-base bonds are defined as vertices, interior edges and exterior edges. To produce admissible secondary structures of single strands, a nucleotide forming base pair with more than one other nucleotide and pseudoknotted structures are prevented. Hairpin loops, stacking regions, bulge loops, interior loops and bifurcation loops can be characterized by the different number of interior and exterior edges that bound them. The free energy of a secondary structure of a single stranded DNA is the summation of free energies of these substructures. The free energies of impossible substructures are set to infinity (e.g., hairpin loop with fewer than four nucleotides) so that no time is wasted on computing energies of these substructures. The minimum free energy is computed recursively: starts from all five nucleotide subsequences and

increase one nucleotide at a time, which saves a lot of time as the minimum energy of all subsequences is already known.

In the Mfold web server, several constraints and folding parameters (e.g. ionic conditions and folding temperature) can be manually changed and then be considered for computing the optimal folding structure. Mfold outputs the suboptimal secondary structures within ten percent of the minimum free energy of the input sequence. These structures were scrutinized in order to remove undesired substructures (e.g., more than four base pairing in the binding sites and loops in the enzyme recognition sites). Depending on the amount and size of substructures, the sequence may be manually adjusted to remove the substructures or selected again from lambda DNA. This procedure was repeated several times until the sequence satisfied the criterion.

However, Mfold can only predict the unpseudoknotted secondary structures of one single strand. NUPACK web server (*132*) was employed instead for predicting that of the motors and tracks since they have several constitutive single strands. The secondary structure model used for developing the algorithm presents the secondary structures in a way similar to Mfold (*135*): the constitutive strands are ordered and drawn in succession from 5' to 3' in a circle with a nick separate adjacent strands and base pair is represented by straight line joining complementary bases. NUPACK employs dynamics programming which recursively calculate the partition function of a complex

containing multiple strands. The algorithm also address distinguishability issue arises as some of interacting strands maybe identical. For real application in DNA self-assembly annealing, NUPACK can take the sequences, concentrations of constitutive strands and ionic concentrations as input and output equilibrium fractions of particular base pair species and equilibrium concentrations of each secondary structure. Once the prominent secondary structure is the desired one, the sequences selection is done.

2.2   Fabrication of DNA motor and track

The normal DNA strands were purchased from Integrated DNA Technologies, Inc. DNA strands that tethered with azobenzene molecules were ordered from Nihon Techno Servie Co. Ltd. The strands were shipped in lyophilized form. To resuspend oligonucleotides for further use, the oligonucleotides were spinned down at a speed of 13000 rpm using centrifuge before opening the tube. Then suitable amount of Tris-EDTA buffer (10 mM Tris-HCL; 1 mM disodium EDTA; pH 8.0) were added to reach a stock concentration of 100 μM. The stock solutions were then vortex thoroughly and stored at -20 ℃.

The motors and tracks were fabricated separately via self-assembly using their constituent strands. The strands were mixed stoichiometrically in

appropriate buffer to produce the final products. (Please refer to individual chapters for detailed annealing conditions and procedures.)

2.3 Special materials for motor operation

Azobenzene molecule can be incorporated into DNA via D-threoninol linker (*136*). Azobenzene can reversibly switch between *trans* form and *cis* form upon light irradiation (see Figure 3.2). The planar *trans*-azobenzene intercalates between DNA base pairs and stabilizes the duplex by a stacking interaction (*137*). Conversely, the duplex favors dissociation due to steric hindrance when azobenzene is in its non-planar *cis*-form. Moreover, *cis* form azobenzene gradually reverts to *trans* from in the dark as it is thermal unstable (*138*, *139*). This occurs much slower than photoisomerization, so the two processes are well separated in time.

The first photo-regulation of hybridization and dissociation of DNA duplex by azobenzene was reported in 1999 (*140*). It is achieved by alternate irradiation of UV and visible light: light absorption by the azo-moieties in the UV (300 nm < λ < 400 nM, absorption maximum of *trans* azobenzene at 330 nm (*136*)) creates a high-energy *cis* form that breaks the duplex; visible light (λ>400 nM) absorption returns the moieties to the ground-state *trans* form that maintains a stable duplex. Multiple azobenzenes have been incorporated into DNA strands to increase photo-regulation efficiency (*141*, *142*). By introducing nine azobenzenes, efficiently photo-control of a 20 mer

oligodeoxynucleotide can be achieved (*142*). This 20 mer oligodeoxynucleotide is used as the leg component of the first motor in this study. Later in 2009 (*143*), the effective photo-regulation was further improved by incorporating azobenzenes into both the two complementary strands of the DNA duplex.

Nicking endonuclease Nt. BbvCI (New England BioLabs Inc.) is used for the operation of the second motor studied in this thesis. Its nicking property has been specifically engineered by modifying naturally occurring heterodimeric restriction enzyme BbvC I (*14*, *144*, *145*). Nt. BbvCI binds to the DNA duplex and recognizes specific seven base pair sequence (5'-CC^TCAGC-3' with ^ indicates the cutting site). The amount of free energy released from DNA backbone cleavage is estimated to be ~5.3 kcal/mol (*146*).

2.4   Characterization methods

2.4.1   Native polyacrylamide gel electrophoresis (PAGE)

Gel electrophoresis is a method that uses electricity to separate macromolecules by molecular weight, conformation and charge as they migrate through the gel. Native polyacrylamide gel electrophoresis (PAGE) was employed due to its ability of preserving the DNA structures formed and the high resolving power for small DNA fragments as used in this study. It is common to use DNA ladder which contains a set of standards as reference to

estimate the size of other DNA duplex. The motors and tracks fabricated consist single-stranded parts which will result in different mobility compared with pure duplexes (*147, 148*). The sizes of these structures are thus hard to decide. Instead, the formation of motors and tracks are confirmed by molecular weight comparison among DNA samples (see individual chapters for details).

Native polyacrylamide gel medium is a mixture of acrylamide and bisacrylamide. Bisacrylamide can crosslink various polymer chains, which are formed by acrylamide in head-to-tail fashion, to from the gel with porosity. Polymerization chain reaction can be greatly accelerated by the free radicals from ammonium persulfate (APS). TEMED (tetramethylethylenediamine) catalyzes the formation of the free radicals which in turn catalyzes polymerization. For small DNA, a better resolution is obtained for high percentage of acrylamide/Bisacrylamide mixture due to its small pore size, and vice versa.

Mini-PROTEAN Tetra Cell System and PowerPac Basic Power Supply purchased from Bio-Rad are used for PAGE experiment throughout this study. The detail procedure as follows. Glass plates with gel thickness of 1.5mm and comb are rinsed with distilled water and 70% ethanol before wipe-dried. The plates are then aligned properly on a flat surface, clamped together by the

casting frame and placed on the casting stand to form a cassette for gel casting.

Prepare the 10% gel solution according to Figure 2.1, which gives the amount of each component required. Dilute 10×TBE buffer with distilled water, then add 29:1 30% Acrylamide and 10% APS. After mixing the solution throughout, TEMED is added. The solution is then vortex-mixed thoroughly and immediately pours into the cassette using pipette (Eppendorf Reference® 2, single–channel, fixed volume of 1 ml) until it fills the short plate. Immediately inserted the 10-well comb into the gel, be careful not to allow air bubbles to be trapped in the gel or under the comb teeth.

Gel percentage	29:1 30% Acrylamide	H_2O	10×TBE	10% APS	TEMED
10%	4ml	6.8ml	1.2ml	200µl	10µl

Figure 2.1 Native polyacrylamide gel conditions.

While waiting for gel polymerization, which takes about 30 minutes, prepare the DNA samples. The final working volume for each DNA sample is ~ 4 µL including 1 µL loading dye (Gel Loading Dye, Purple (6X), no SDS by New England Biolabs). DNA ladder (Low molecular weight DNA ladder by New England BioLabs) is prepared in the same way. The loading dye contains Ficoll-400 that renders the DNA sample denser than the running buffer to ensure the sample sink to the bottom of the well.

After polymerization is complete, take out the glass plates and gently remove the comb. Rinse the wells thoroughly with distilled water to remove any gel remnants. Then place the polymerized gel into one side of the clamping frame with the short plate facing inward. If running only one gel, use buffer dam for the other side. Put the assembly into the tank with electrodes match with the markers on the top inside edges of the tank. Then fill the wells with running buffer (1×TBE) and make sure no air bubbles in the wells, continue the filling till the buffer level reaches the 2-gel marker labeled on the tank. Load the DNA sample-loading buffer mixture into the wells using pipette (Eppendorf Reference® 2, single–channel, fixed volume of 10 μL). Connect the electrodes to the power pack and turn on the power. For 10% gel, select constant voltage mode, set voltage to 90 V, set time to 70 minutes, and begin the electrophoresis run.

After gel electrophoresis finishing, remove the glass plates from the assembly and pour the running buffer back into the container for further use. Then detach the short glass plates carefully and transfer the gel to a plastic box while keep the gel intact. 50 ml 3×GelRed (Biotium Inc.stain) is poured into the box to stain the gel. After 10 minutes, take out the gel and then scan it using Gel-documentation system (Gel Doc™ EZ Imager, Bio-Rad) to take image.

2.4.2 Motor motility detection by fluorescence measurement

The motor's motility was detected using fluorescence measurement. The motor legs and track was labelled with two identify quenchers and different dyes respectively (please refer to individual chapters for details). Upon light irradiation, the dyes will emit light of lower energy (longer wavelength) than the excitation light after a brief interval (1ns~100ns). This phenomenon is termed fluorescence. When the quencher is close enough to the dye (e.g., motor-track binding), the quencher is able to absorb light emitting of the dye and dissipates the energy absorbed as heat instead of light. The changes of fluorescence intensities of the dyes indicate the motor's movement on the track.

Chapter 3   Systematic Study of A Light-driven Motor and Its Derivatives

3.1 Introduction

As far as bipedal nanomotors are concerned, either a bias for rear leg dissociation (ratchet) or a bias for forward leg binding (sometimes called power stroke) is able to rectify a net directional stepping in an average sense. But the chance of either control alone making a successful forward step per event of energy consumption or per fuel molecule consumed is subject to a fundamental upper limit of 50%, as a recent theoretical study (*127*) suggests. Breaking the limit is necessary for a nanomotor's efficient utilization of energy, and a viable route (*127*) is integration of the two complementary biases. Indeed, two biological nanmotors, F1-ATPase rotor and kinesin walker, are known to integrate (*32*, *62*, *71*, *124*, *127*) both controls to achieve more than 99% fidelity (*50*, *51*, *54*, *128*, *129*, *149*) of forward stepping per fuel molecule consumed, a trait underlying efficient (*49*, *150*) utilization of fuel energy by both motors.

The detailed mechanisms of biological nanomotors attaining the synergic control of passive ratchet plus active stroke remain largely unclear

due to complexity of the biological systems. Artificial nanomotors reported to date mostly implemented the ratchet, (*13–18, 23, 39, 41, 151*) and many adopted a burn-bridge method (*13–15, 17, 23*). It remains a challenge to integrate the two differing types of control in a rationally designed motor-track system without modifying its irreversibly. Recently a track-walking bipedal DNA nanomotor (*24*) powered by light was developed from a bioinspired design principle (*123*) that has the potential to implement both controls simultaneously. However, it is difficult to obtain direct experimental signals for either control separately, partly due to a tight coupling of the two controls. In this study, we carry out a systematic study of the motor and new variations. The experimental data plus a simplistic mechanical modeling are used to analyze mechanistic integration of the motors.

3.2 Motor-track system

3.2.1 Motor-track construction

As illustrated in Figure 3.1A, the normal motor is a DNA double-strand helix (D3-D3*, two helical turns) connecting two identical single-strand legs. Either leg is a 20-nucleotide-long D2 segment followed by a 5-nucleotide-long D1 segment. For mechanical flexibility, a 4-nucleotide long single-strand linker (S1) is introduced at the junction of the leg and the D3-D3* helix. The two longer motor variations are obtained by making their D3-D3* duplex one or two helical turns longer than the normal motor. The track is

made of double-strand helices D4-D4* (25.5 nm long), D5'-D5'* and D5-D5*

(5.1 nm), which supports repeated pairs of D1* and D2*overhangs (Detailed

sequences of the motor variations and the track can be found in section 3.7).

A. Motor

D3
S1 (4nt)
D3*
D2 (20nt)
D1 (5nt)

Motor	D3-D3*
Normal	6.8nm
Longer	10.2nm
Longest	13.6nm

B. Track

TAMRA   FAM
D2*
D5'*   D4*   D1* D5*
Minus end   Plus end
D5'   D4   D5
5.1nm   25.5nm   5.1nm
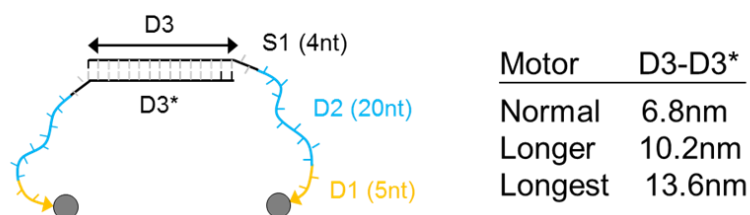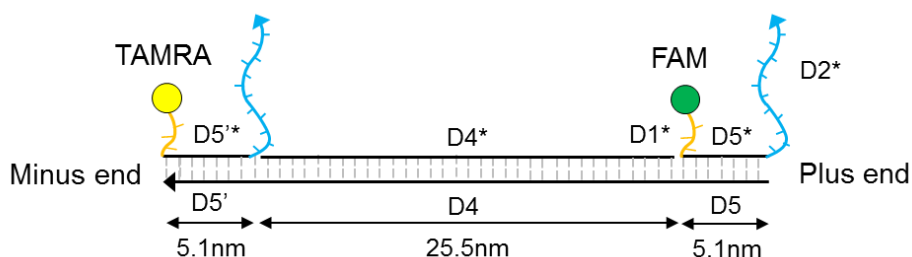
Figure 3.1 Schematic illustration of the motor variations and track construction.
The normal motor and two variations (with a longer D3-D3* duplex as indicated) are
labeled with quenchers (BHQ-2, marked by black spheres), and the two-site track is
labeled with two dyes at the minus and plus ends (TAMRA and FAM, marked by
yellow and green spheres, respectively). The motor is made of two DNA strands and
has two identical single-stranded legs with sequences D1-D2. The track is made of
four species of DNA strands and supports two binding sites that are each formed by
two adjacent single-strand overhangs D1* and D2* (stars indicate complementary
sequences).

A leg of the motor binds to the track by forming double-strand helices

with either a D1* or D2* foothold. The ensuing D1-D1* and D2-D2* helices

are ~1.7 and ~6.8 nm long, respectively. Each pair of D1* and D2* footholds

sandwiching a D5'-D5'* or D5-D5* helix may be regarded as a composite

binding site, since it is the only track domain capable of forming thermodynamically stable helices with the motor's legs. Drawing from the D1* to D2* within a composite site points to a unique end of the track, which will be called the plus end hereafter. The motors carry two quenchers (BHQ-2) at their legs, and the track carries two different dyes (Figure 3.1B, FAM and TAMRA with excitation/emission wavelengths of 495 nm/520 nm and 559 nm/583 nm respectively). Hence, the motor's movement is indicated by the fluorescence changes of the two dyes when the motor is moving on the track.
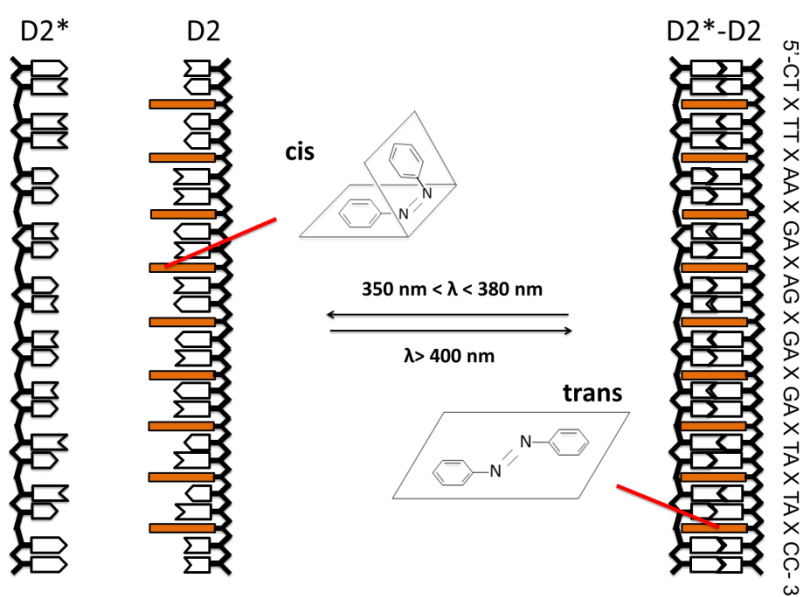
Figure 3.2 Light-controlled hybridization of motor leg with binding site. The motor leg segment (D2) is tethered with azobenzene moieties. Its hybridization with the complementary D2* segment from the track is controlled by light. Also shown are the *cis* and *trans* configurations of the azobenzene moieties (represented by long rectangles and marked as "X" in the given nucleotide sequence for D2).

The motor can be operated through any technical means that breaks the D2-D2* helix without destabilizing the chemically different D1-D1* duplex.

We develop a light-powered version in which the leg's D2 segment contains light-responsive azobenzene moieties (*136*) in the nucleotide backbone. The operation is achieved by alternate irradiation of UV and visible light: Light absorption by the azo-moieties in the UV creates a high-energy *cis* form that breaks the D2-D2* duplex; visible light absorption returns the moieties to the ground-state *trans* form that maintains a stable D2-D2* duplex.

3.2.2   Design principle
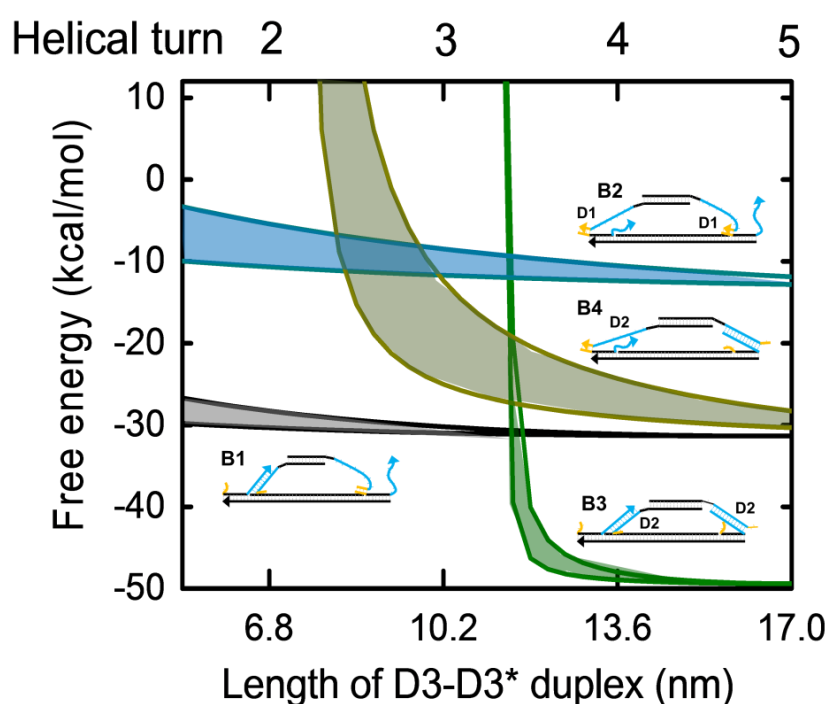
Figure 3.3 Free energies of the motor's bridge states predicted by a simplistic mechanical model *versus* length of the motor's D3-D3* duplex. The shadows indicate the upper and lower boundary due to uncertainty of the persistence length for single-stranded DNA (between 1-3 nm from ref (*152*)). The zero value for free energies corresponds to the motor with both legs derailed off the track.

The motors are an implementation of a design principle (*123*) that is inspired by biomotors (*62, 86*). A key character of this bioinspired design principle is that a motor of symmetric legs may gain a net direction from proper free-energy gaps between motor-track binding states of differing geometric features. As schematically illustrated in Figure 3.3, a motor of the present study has four possible intersite bridge states in which the motor's two legs are bound to two adjacent composite sites. Two are symmetric in that the motor's two legs hybridize into identical helices with the track (i.e., states B2 and B3 in Figure 3.3). The other two are reversely asymmetric; the D1-D1* helix leads the D2- D2* toward the plus end in one state (B1) and toward the opposite end in the other (B4).

There must exist a regime of small size of the motor where the B1 state becomes the lowest in free energy among the intersite bridge states, as suggested by a qualitative analysis (*24*). This conclusion is supported by a simplistic mechanical model for the DNA motor. Figure 3.3 shows the free energies for the four bridge states predicted by the mechanical model versus the motor's size as the latter is hypothetically changed by assuming a different length for the D3-D3* duplex. When the duplex is long, e.g., more than five helical turns, the B4 and B1 states are almost equal in free energy, and the symmetric B3 state is even lower. When the D3-D3* duplex becomes short, e.g., two helical turns as for the motor, the free energies for B4 and B3 are elevated beyond that for B1, rendering it the most accessible bridge state.

Qualitatively speaking, the trend of size dependence is meaningful and largely decided by geometry of the states, despite the limited power of the mechanical model for quantitative prediction (see below for the reasons). Overall, the model predicts that the symmetry breaking exists in the motors but deteriorates for the elongated motor variations. This size dependence is a character of the design principle.

3.2.3 Motor operation mechanism

If the motor's B1 state has a lower free energy and thereby occurs more often than B4 by Boltzmann's law, the symmetry of motor-track binding is broken in the sense that the leg to the plus end (referred to as leading leg hereafter) is in the D1-D1* helix and the trailing leg is in D2-D2*.

For a motor initially in the B1 state, as shown in Figure 3.4A, the UV irradiation has a chance to dissociate the trailing leg off the track but not the leading leg, though both are chemically identical. This position selective dissociation of the rear leg is a Brownian ratchet effect. The leg dissociation triggers a migration of the front leg from the D1* foothold to the nearby D2* to form a longer, *i.e.*, more stable, helix. The visible light irradiation stabilizes this intrasite downhill migration (state C in Figure 3.4A), which places the dissociated leg closer to the forward composite site than to the backward site. Thus the dissociated leg is biased to bind the forward site under visible light to resume the stable B1 state at a location one step forward. The migration-

induced bias for forward binding is a power stroke. The full mechanical cycle

A→B→C→D→A translocates the motor a step to the plus end.
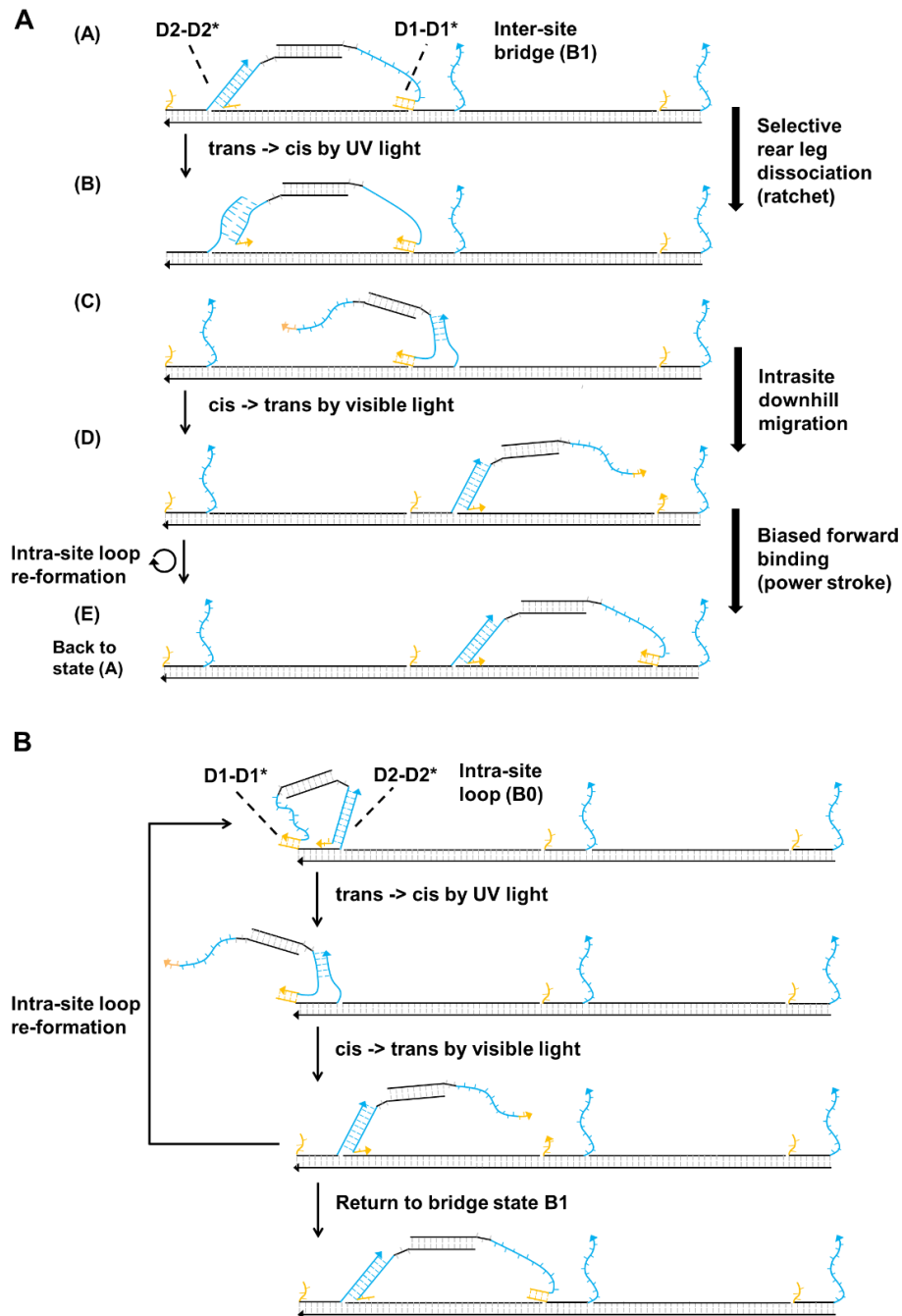
Figure 3.4 Stepping pattern of the motor. Shown are the major intermediate states and transition pathways for the light-driven motor starting from an intersite bridge state (A) and from an intrasite loop state (B).

Previous study on this light-driven motor found that it is possible for the motor to form the intrasite loop state B0 with its two legs hybridize with the D1* and D2* footholds within a composite site (*24*). As illustrated in Figure 3.4B, the loop state is asymmetric also: the trailing leg is in the D1-D1* helix and the leading leg in D2-D2*. Although both loop state B0 and bridge state B1 have the same leg hybridizations, the single-stranded segments of B0 are less stretched than that those of B1, which renders lower free energy of B0 compare to B1. The pre-operation fluorescence signals yield the intersite bridge over intrasite loop state population ratio R=0.138, indicating a nontrivial presence of the loop state (*107*).

The loop state can be transferred to bridge state B1 by light operation as shown in Figure 3.4B. The UV irradiation selectively dissociates the leading leg, but the freed D2* foothold is occupied again via the downhill migration of the trailing leg under visible irradiation. The dissociated leg either binds forward to form a bridge state or binds backward with the D1 foothold to form a loop again at the same site. The backward binding makes a futile step, while the forward binding returns the motor to the forward stepping pathway. The loop formation does not compromise the motor's direction, but competes with the motor's power stroke and reduces the motor's speed. Besides, the loop may form repeatedly at the plus-end site under rounds of light operation, effectively preventing a forward-moving motor from falling off the track's end.

The two motor variations with longer duplex bridge may achieve better performance than the normal motor by lowering the population of the loop state which maybe sterically harder to form for longer motor.

3.3 Materials and Methods

3.3.1 Motor variations and track fabrication

The motor variations and tracks were fabricated separately via self-assembly using their constituent strands (see section 3.7 for DNA strands and sequences). The strands were mixed stoichiometrically at 5 uM in a buffer containing 10 mM Tris-HCl, 1 mM EDTA and 500 mM NaCl. The samples were then incubated in a water bath at 95 °C for 20 minutes, after which the water heater was turned off to gradually cool down the samples from 95 °C to 25 °C over a period of 5 hours. The two-site track was assembled following the same annealing procedure in the same buffer, except for 1.5 M NaCl. The annealing products were analyzed using 10% native polyacrylamide gel electrophoresis (PAGE) against a low molecular weight DNA Ladder (New England BioLabs Inc.). The formation of motors and track is confirmed by one prominent band of expected molecular weight.

3.3.2 Fluorescence detection of motor motility

The motor's light-driven motility was detected using a fluorescence method. An equimolar mix of the motor and track sample was incubated at final concentration of 10 nM over a long time (24 h) to ensure thermodynamic equilibration of the motor-track binding. The long incubated sample was then used for light operation and fluorescence measurement. The motility experiments were conducted using a RF-5301PC spectrophotometer (150 W Xenon lamp, Shimadzu Corp.). A walker-track sample was first irradiated by visible light to collect the intensities of the two dyes before light operation. For each round of irradiation operation, a walker-track sample was first irradiated by UV light through a filter of narrow wavelength window (wavelengths of 350 nm over 5 nm excitation slit width) for a period of time, followed by visible irradiation (excitation wavelengths of the two dyes are 495 nm and 549 nm for FAM and TYE respectively, both over 5 nm excitation slit width) and fluorescence measurement. Both the incubation and the motility experiments were done at 25 °C for 10 nM motor-track concentrations in a buffer containing 5 mM Tris-HCl, 150 mM NaCl and 1 mM EDTA. The low concentrations suppress the possibility of one motor cross-linking more than one track.

The motility experiments were each accompanied by a control experiment in which the same light operation was applied to the same amount

of track sample alone. The light irradiation resulted in a slight photobleaching in the control experiments. Influence of the photobleaching is removed from the fluorescence data of a motility experiment by dividing the data by the fluorescence data from the corresponding control experiment. The control-calibrated data are further analyzed as detailed in the following section and the analysis results are shown in Figure 3.6 – 3.8.

3.3.3 Extracting direction, dissociation and rate ratios from the normalized control-calibrated fluorescence data

The control-calibrated fluorescence data is obtained by dividing the fluorescence data by the corresponding normalized control data

$$I(t) = \frac{I_f(t)}{I_c(t)/I_0} \tag{1}$$

in which $I_f(t)$ is the fluorescence data, $I_c(t)$ is the corresponding control experiment, and I_0 is the initial fluorescence of the control. In the motility experiments, the percentage fluorescence change of the dye against its preoperation signal is

$$I_V(t) = \frac{I(t)}{I(0)} - 1 \tag{2}$$

in which $I(t)$ is the control-calibrated fluorescence data from the dye of a motility experiment at a time t. The motor's directional motion from the minus end to the plus end can be quantified by the percentage fluorescence change of

57

the minus-end dye minus that of the plus-end dye at the end of each operational cycle, which is

$$I_{V-,\ i} - I_{V+,\ i} \tag{3}$$

Here $I_{V\pm,\ i}$ is the data point immediately after the visible irradiation of i th operation cycle as shown in Figure 3.6, with + or - marks the plus-end or minus-end site. The sum of both percentages likewise quantifies the level of leg dissociation during the motor's operation. Thus the average leg dissociation of the motor is

$$\frac{I_{V-,\ i} + I_{V+,\ i}}{2} - 1 \tag{4}$$

The probability for a site to be occupied by a motor leg, $P(t)$, is linked to the fluorescence from the dye as

$$P(t) = \frac{1}{\gamma}\left(1 - \frac{I(t)}{I_0}\right) \tag{5}$$

in which γ is the quenching efficiency. The average rate for leg dissociation from the start of a UV irradiation t_1 to its end at a later time t_2 is

$$k_{d\pm} = \frac{P_{\pm}(t_1) - P_{\pm}(t_2)}{t_2 - t_1} = \frac{1}{I_{0\pm}\gamma_{\pm}}\frac{I_{\pm}(t_2) - I_{\pm}(t_1)}{t_2 - t_1} \tag{6}$$

The dissociation rate ratio of the rear leg to the front leg is

$$\frac{k_{d-}}{k_{d+}} = \alpha\frac{[I_-(t_2) - I_-(t_1)]/I_-(0)}{[I_+(t_2) - I_+(t_1)]/I_+(0)} = \alpha\frac{I_{U-,i} - I_{V-,i-1}}{I_{U+,i} - I_{V+,i-1}} \tag{7}$$

in which

$$\alpha = \frac{I_-(0)/I_{0-}\gamma_-}{I_+(0)/I_{0+}\gamma_+} \tag{8}$$

$I_{U\pm,\ i}$ is the data point immediately after the UV irradiation of i th operation cycle. The term after α is just the ratchet signal shown in Figure 3.8B and Figure 3.9D. Since the quenching efficiency at either site is close to 100% due to the contact quenching (*153*), $\gamma_-/\gamma_+ \approx 1$ and

$$\alpha \approx \frac{I_-(0)/I_{0-}}{I_+(0)/I_{0+}} \tag{9}$$

The average rate for leg binding from the start of a visible irradiation t_1 to its end t_2 is

$$k_{b\pm} = \frac{P_\pm(t_2) - P_\pm(t_1)}{t_2 - t_1} = \frac{1}{I_{0\pm}\gamma_\pm} \frac{I_\pm(t_1) - I_\pm(t_2)}{t_2 - t_1} \tag{10}$$

The binding rate ratio of leg binding to the front site over back site is

$$\frac{k_{b_+}}{k_{b_-}} = \frac{1}{\alpha} \frac{[I_+(t_1) - I_+(t_2)]/I_+(0)}{[I_-(t_1) - I_-(t_2)]/I_-(0)} = \frac{1}{\alpha} \frac{I_{U+,i} - I_{V+,i}}{I_{U-,i} - I_{V-,i}} \tag{11}$$

with the term after α as the power stroke signal shown in Figure 3.8A and Figure 3.9C.

3.3.4 Simplistic mechanical model

In the mechanical model, we estimate the free energy for a motor-track state as the leg-track hybridization energy associated with the helix formation plus the stretching energy of the remaining single-stranded component of the motor. Any other nonspecific motor-track interactions are ignored, which is a rather crude approximation. The hybridization energies for helices D1-D1*

and D2-D2* are estimated as -6.65 and -24.7 kcal/mol (25 °C) for the sequences adopted in this study using the nearest-neighbour thermodynamics (*154*) for DNA. The strand-stretching energy is estimated using a worm-like chain formula (*62*): $F(l, d) = k_B T(l/l_p)[x^2(3 - 2x)/4(1 - x)]$. Here T is the temperature in Kelvin, $x = d/l$, l is the total contour length of the single-stranded portion of the motor ($\sim$0.7 nm per nucleotide from ref (*155*)), and d is the extension required of the single-stranded portion to form the motor-track binding state. l_p is the persistence length for single-stranded DNA (1-3 nm from ref (*152*)).

3.4 Results

3.4.1 Formation of motors and track

The motors and track with two binding sites were assembled separately from their constitute DNA strands. The formation of motors and track are confirmed by one prominent band of expected molecular weight using polyacrylamide gel electrophoresis (PAGE), as shown in Figure 3.5.
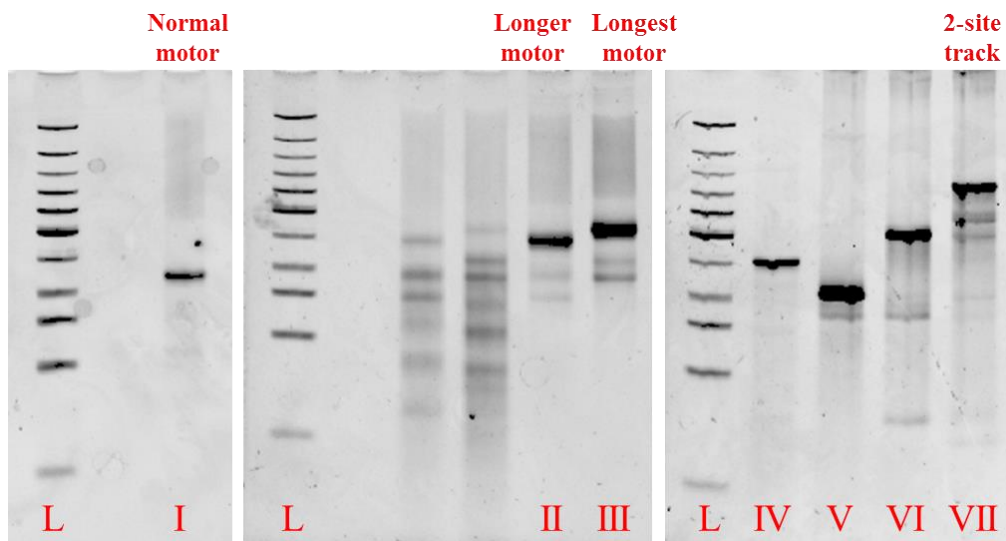
Figure 3.5 The motor variations and track formation. Shown are gel images obtained using native PAGE. Lane Ls are low molecular weight DNA ladder. Lanes I, II and III are the motor variations with increasing length. Lane IV-VII show stepwise assembly of the two-site track: Lane IV is the track template strand TwT; Lane V is the annealing product of TwT with the 75nt linker strand TL; Lane VI is the annealing product of TwT, TL and TBM2; Lane VII is the annealed complete two-site track.

3.4.2 Motility experiments

The two elongated motors plus the normal one were tested. Motor operation on the fully labelled two-site track offers many details of the motor's working mechanisms. Figure 3.6 shows a typical fluorescence data (for the normal motor) that calibrated against a bare track control and then normalized to the initial value. The application of light irradiation exposes a zigzag pattern for the fluorescence from dye labeled at both the plus-end and minus-end sites. The fluorescence signals rise after each UV irradiation and drop over the course of ensuing visible irradiation. The rise indicates the UV-induced leg dissociation, and the drop indicates the subsequent leg-track binding under

61

visible light. Signals for directional motion (Figure 3.7A, Figure 3.9A), leg

dissociation (Figure 3.7B, Figure 3.9B), power stroke (Figure 3.8A, Figure

3.9C) and ratchet (Figure 3.8B, Figure 3.9D) can be extracted from the

normalized control-calibrated fluorescence data as exemplified by Figure 3.6

(see section 3.3.3 for details).
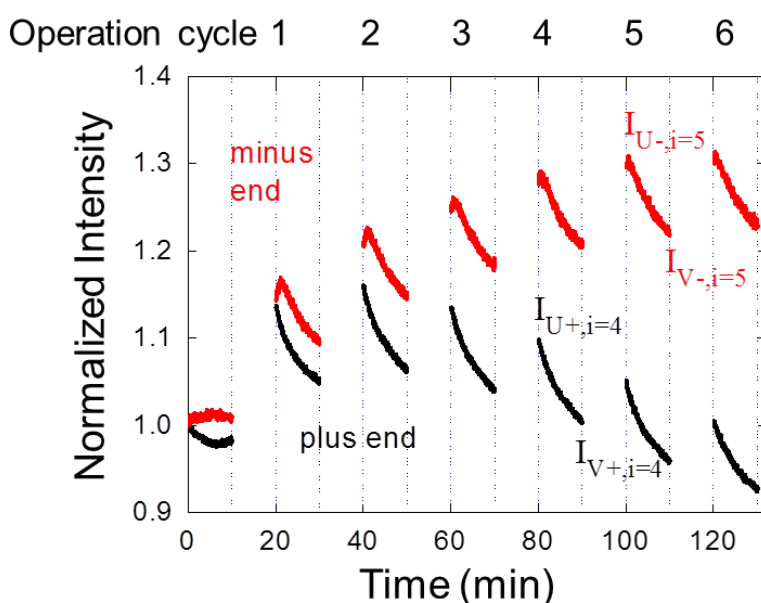
Figure 3.6 Motility experiments. Operation of the three motors on the track under six operation cycles of 10 min UV irradiation followed by 10 min visible light per cycle. The experiments are done usin*g* equilibrated, equimolar motor-track mix, and a half cycle of visible irradiation is applied before the first full cycle. The blank intervals are the time of UV irradiations when no fluorescence is collected.

The motor's directional motion from the minus end to the plus end can

be quantified by the percentage fluorescence change of the minus-end dye

against its preoperation signal (e.g., the data at time zero of Figure 3.6) after

the operational cycles minus the thus-defined percentage change of the plus-

end dye. The sum of both percentages likewise quantifies the level of leg dissociation during the motor's operation.
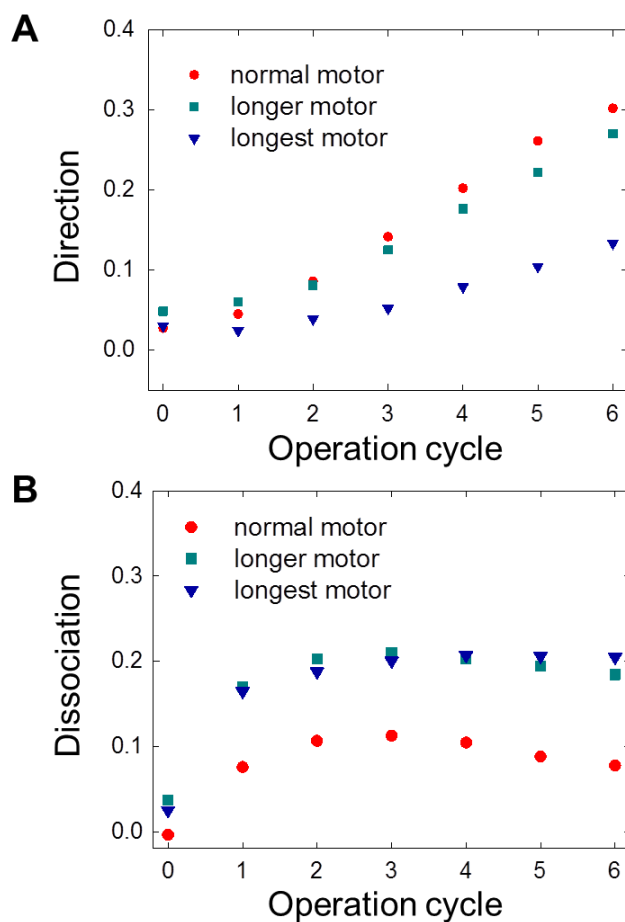
Figure 3.7 Directional motion and leg dissociation. (A) The motor's directional motion from the minus end to the plus end at the end of each operation cycle estimated from the fluorescence data. (B) The average leg dissociation of the motor during operation at the end of each operation cycle estimated from the fluorescence data.

The signal of directional motion increases with successive irradiation cycles for all three motors (Figure 3.7A). A comparison of the motors under the same irradiation cycles shows that the signal drops in magnitude from the normal motor to the longer variation and further to the longest one (Figure

3.7A). The observation of poorer directional motion for longer motors is consistent with the prediction of deteriorating symmetry breaking by motor elongation, which is a character of the motor design principle.

The signal of leg dissociation from the above mentioned percentages increases within the first one or two irradiation cycles and becomes flat afterward (Figure 3.7B). The saturation behavior indicates a low chance for the entire motor to derail off the track during successive irradiation cycles. Nevertheless, the elongated motors yield a higher dissociation signal than the normal motor. The observation is again compatible with deteriorating symmetry breaking by elongated motors as they access more bridge states to have less selectivity in UV-induced leg dissociation (hence more dissociation).

3.4.3   Ratchet and Power Stroke

The zigzag patterns of fluorescence data yield signals for biased forward binding and selective rear leg dissociation. During visible irradiation, the ratio of the percentage fluorescence drop of the plus-end dye (against the preoperation fluorescence) over the percentage drop of the minus-end dye is an indicator of possible imbalance in forward and backward leg binding. The higher the ratio, the more bias for forward binding over backward binding. Similarly, the ratio of the percentage fluorescence rise of the minus-end dye (against the preoperation fluorescence) by UV irradiation over the percentage rise of the plus-end dye is an indicator of possible imbalance in rear or front

leg dissociation. The higher the ratio, the more preference for dissociation of the rear leg over the front leg. Under the same irradiation cycles, the three motors operating on the same two-site track show three features in their ratchet and power stroke signals (Figure 3.8).
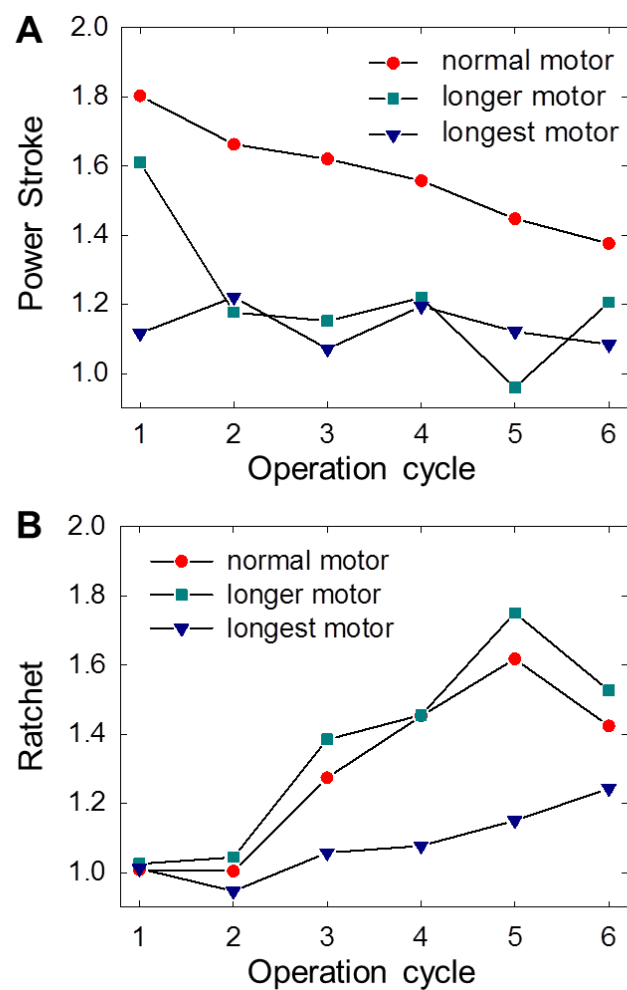
Figure 3.8 Power stroke and ratchet. The shown ratio per cycle is for the average binding or dissociation rates during a cycle's visible or UV irradiation. (A) Rate ratio of visible induced leg binding of the plus-end site to the minus-end site estimated from the fluorescence data (as in Figure 3.6) immediately before and after the visible irradiation. (B) Rate ratio for UV induced leg dissociation of the minus-end site to the plus-end site estimated from the fluorescence data immediately before and after the UV irradiation.

First, both the ratchet and power stroke signals tend to be lower for a longer motor, an observation compatible with the deteriorating symmetry breaking by motor elongation. Accessibility of more bridge states to a long motor tends to reduce its dissociation selectivity as mentioned above. The forward bias tends to be reduced too if a motor is long enough to reach the back site anyway from a postmigration single-leg binding.

Second, the power stroke signal drops with successive irradiation cycles, especially for the normal motor that exhibits the highest power stroke signal. This feature is in line with the expectation that the signal for unbalanced forward and backward binding comes from the operation-induced transitions from the loop state at the plus-end or minus-end site to intersite bridge states. The loop population diminishes at the minus end by successive irradiation cycles, rationalizing the trend of the power stroke signal.

Third, the ratchet signal rises within the first few irradiation cycles and drops afterward. This is compatible with the expectation that the signal for unbalanced leg dissociation comes from the UV-induced transitions from bridge states to a single-leg state at the plus-end or minus-end site. The loop-to-bridge transitions by the early irradiation cycles tend to increase the bridge population, but more operation cycles later may transfer the bridge population to a loop at the plus end. Hence the bridge population first rises and then drops, rationalizing the trend of the ratchet signal.

The dissociation rate ratio of the rear leg to the front leg can be estimated from the ratchet signal. The time-zero fluorescence for the motility experiments and corresponding control experiments yield the same value of α ≈ 0.73 for the three motors. Hence k_{d_-}/k_{d_+} is more than 1 for any ratchet signal above 1.37. The data in Figure 3.8B show that the preferential rear leg dissociation (namely, $k_{d_-}/k_{d_+} > 1$) exists for the normal motor (and also for the motor variation with a 10.2 nm long D3-D3* duplex).

Similarly, the rate ratio of leg binding to the front and back sites can be estimated from the power stroke signal. Since α is less than 1, k_{b_+}/k_{b_-} is more than 1 for any power stroke signal above 1. The data in Figure 3.8A indicate the existence of preferential forward binding (namely, $k_{b_+}/k_{b_-} > 1$) for all three motors. Combining the rate analyses for leg binding and dissociation, we can conclude that the normal motor achieves both ratchet and power stroke.

3.4.4 Operational variations
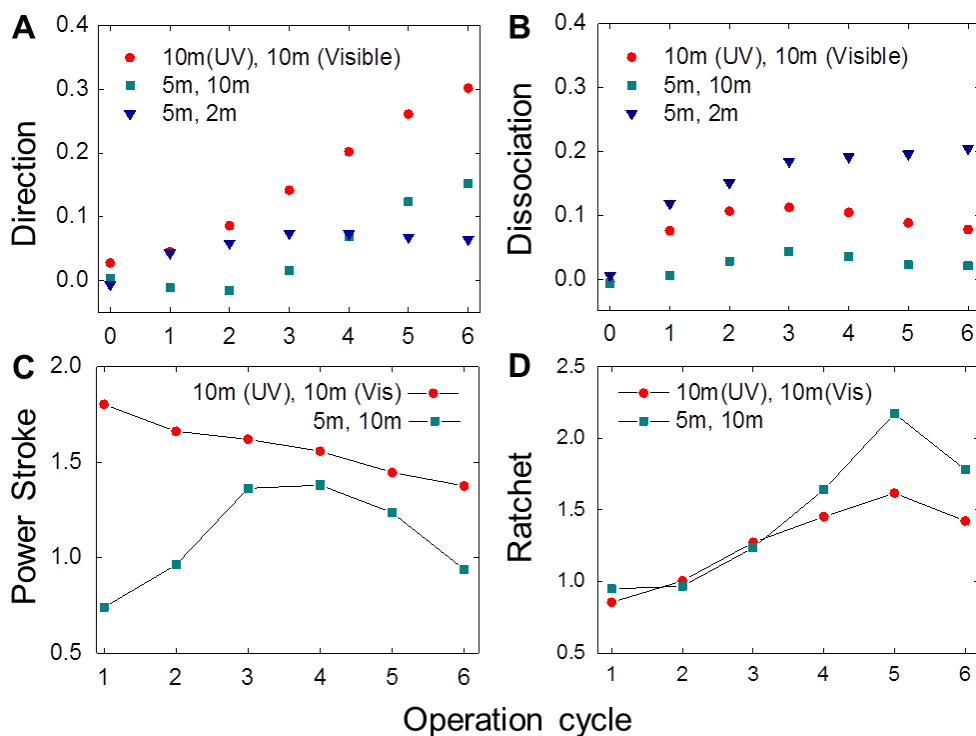
Figure 3.9 Operational variations. Operational variations for the same motor-track system and two-color motility experiments as for Figure 3.6. The data were obtained for the normal motor for operation cycles of different UV and visible irradiation duration as indicated. The variations are estimated in the same way as for Figure 3.7 and Figure 3.8.

Figure 3.9 shows the results of two-color motility experiments on the normal motor for different UV/visible irradiation time per operation cycle. When the visible irradiation is kept as 10 min and the UV irradiation shortened from 10 min to 5 min, the signals for directional motion and leg dissociation both drop. This is understandable since the UV-induced D2-D2* breaking amounts to the driving force for the motor. The power stroke signal also decreases as the shorter UV irradiation induces less loop-to-bridge

transition. The ratchet signal for later operation cycles is slightly higher for the shorter UV irradiation, since the bridge population is better preserved during the later operation cycles with shorter UV irradiation. When the UV irradiation is kept as 5 min and the visible irradiation is shortened from 10 min to 2 min, the signal for directional motion changes little, but the dissociation signal is more than doubled. This is consistent with the role of visible irradiation to stabilize leg-track binding.

3.5 Discussions

Brownian ratchet and power stroke contribute additively to motor performance. The position-selective dissociation of the rear leg is a Brownian ratchet effect: the dissociated leg might bind back to resume the D2-D2* helix, but the ensuing asymmetric bridge B1 subjects the trailing leg to UV-induced dissociation yet again. The bridge-forming backward binding produces a futile step, which is prevented by the ratchet from developing into a full backward step. The migration-induced forward bias is a power stroke, because it uses the energy gained from forming a longer helix to actively place the dissociated leg ahead to favor a binding forward over backward. The power stroke advances a forward step at the cost of a futile one.

The power stroke and the ratchet contribute additively to the motor's performance: the stroke suppresses the chance of futile steps that waste energy and reduce the motor's speed; the ratchet prohibits backward steps that

compromise the motor's direction. Therefore, integrating a ratchet-like passive control and a stroke-like active control is a key to making advanced nanomachines that perform better yet consume less energy. We notice an ongoing debate (*156*) on suitability of the term "power stroke" for molecular motors from the perspective of microscopic reversibility. In this study, we follow the conventional use (*38*) of this term to denote biased forward binding. Whatever you may call it, it is an extra effect different from but complementary to the ratchet effect (i.e., selective dissociation). As far as the motors of this study are concerned, the two effects are linked to different experimental signals, which have been separately obtained from the zigzag patterns of two-color motility experiments.

Both ratchet and power stroke can be implemented via a design principle of mechanics-mediated symmetry breaking. The ratchet and stroke share the same mechanistic root in the design of a distinct free-energy hierarchy for motor-track intersite binding states, which are intermediate states for a motor's motion down the track. The ratchet originates from asymmetry breaking, namely, dominance of the asymmetric state B1 in a motor's intersite binding, which is ensured by this state attaining the lowest free energy among all possible intersite bridge states. The power stroke involves different free-energy gaps associated with forward and backward binding of the dissociated leg of a postmigration motor: The forward binding forms the lowest energy bridge B1 and hence stretches the motor least; the backward binding must

form a high-energy bridge (i.e., B3 or B4) and stretch the motor more. Hence the power stroke originates from the symmetry breaking also. The close relation of the symmetry breaking with the ratchet/stroke is compatible with the multiple correlations observed between the signals of directional motion, ratchet and power stroke.

A major character of the motor design principle in this study is that the symmetry breaking is caused by tuning the motor's size. Such a mechanics-mediated symmetry breaking can be clarified by considering the limit of a long motor whose single-stranded segments are mechanically relaxed in the two reversely asymmetric bridge states B1 and B4. The free energy for either state is then dominated by the leg-track helix formation, which is identical for both states. Hence the free energies of the twin states converge to the same value in the long-motor limit, rendering the overall motor-track intersite binding symmetric. The two symmetric bridge states B2 and B3 cannot produce any selective dissociation (i.e., ratchet) anyway under the UV irradiation; neither can the two reversely asymmetric states because they occur by equal chance according to Boltzmann's law so that the selective dissociation from one state is perfectly canceled by that from the other. A short motor deviating from the long-motor limit must be stretched in the two states to affect their free energies. A free-energy gap then arises between the twin states because their reversed asymmetry requires different stretch of the motor. Consequently, the asymmetric B1 becomes the single, lowest lying

bridge, breaking the motor-track intersite binding symmetry. The size dependence of the symmetry breaking is confirmed by the experiments of the normal motor versus the two elongated motor variations.

The design principle (*123*) for the present motors was derived from biological nanomotors kinesin (*62*) and myosin V (*86*). The two biomotors and the present artificial motors are all symmetric bipeds on tracks of identical binding sites that each host an internal, local asymmetry. As this study suggests, such a highly symmetric motor-track system attains a direction not necessarily by burn-bridge methods (*13–15*, *17*, *23*); instead the direction can be produced by a mechanics mediated symmetry that amplifies the intrasite asymmetry into intersite ratchet and power stroke.

3.6 Summary of Chapter 3

A light-powered DNA nanomotor and new variations are systematically studied using multiple fluorescence labeling and specially designed light operation. The experimental data suggest that the motor achieves a ratchet-plus-power stroke synergic control through a mechanics-mediated symmetry breaking, in a way similar to biological nanomotors. This study presents an experimental validation for the bioinspired design principle of mechanical breaking of symmetry for integrated passive-active control. Using the rationally designed DNA motors as a model system and augmenting the data with mechanical modeling, this study provides valuable mechanistic

insights that may help advance molecular control in future nanotechnological systems.

3.7 DNA strands and sequences

The DNA strands forming the motors and tracks are all marked in Figure 3.10. Below are their sequences given in 5' to 3' direction. The asterisk * marks a complementary sequence.

A. Motor

MS1   MS2

B. Track

TAMRA   TBM1   FAM
TBM2
TL
TwT
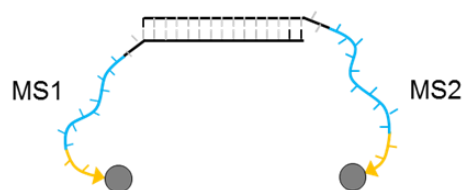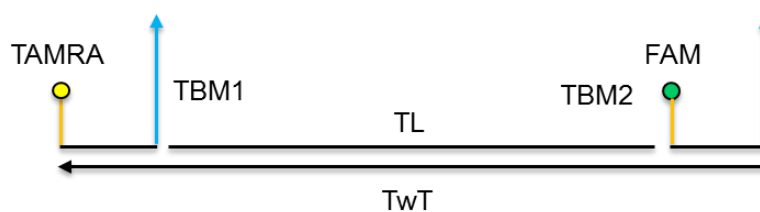
Figure 3.10 DNA strands of motors and track.

A. Motor strands

X indicates azo-moiety covalently inserted into the backbone of the oligonucleotides**.**

A1. The normal motor

MS1 = D3-S1-D2-D1 (20+4+20+5 = 49 mer) with quencher:

5′ - GAGTTACCATCTAGGTAGAG+AGTC

+CTXTTXAAXGAXAGXGAXGAXTAXTAXCC+ATTCC - 3′ - BHQ2

MS2 = D3*-S1-D2-D1 (20+4+20+5=49 mer) with quencher:

5′ - CTCTACCTAGATGGTAACTC+AGTC

+CTXTTXAAXGAXAGXGAXGAXTAXTAXCC+ATTCC - 3′ - BHQ2

The two elongated motor variations contain in their D3 and complementary D3* segments extra nucleotide sequences (underlined in their corresponding sequences).

A2. The longer motor

MS1E1 = D3-S1-D2-D1 (30+4+20+5 = 59 mer) with quencher:

5′ - <u>GGGGATTTCGG</u>AGTTACCATCTAGGTAGAG+AGTC

+CTXTTXAAXGAXAGXGAXGAXTAXTAXCC+ATTCC - 3′ - BHQ2

MS1E1 = D3*-S1-D2-D1 (30+4+20+5=59 mer) with quencher:

5′ - CTCTACCTAGATGGTAACTC<u>CGAAATCCCC</u>+AGTC
 CTXTTXAAXGAXAGXGAXGAXTAXTAXCC+ATTCC - 3′ - BHQ2

A3. The longest motor

MS1E2 = D3-S1-D2-D1 (40+4+20+5 = 69 mer) with quencher:

5′ – <u>ATGTCGGGGATTTCGTCACA</u>GAGTTACCATCTAGGTAGAG

+AGTC+CTXTTXAAXGAXAGXGAXGAXTAXTAXCC+ATTCC-3′-

BHQ2

MS2E2 = D3*-S1-D2-D1 (40+4+20+5=69 mer) with quencher:

5′ – CTCTACCTAGATGGTAACTC<u>TGTGACGAAATCCCCGACAT</u>

+AGTC+CTXTTXAAXGAXAGXGAXGAXTAXTAXCC+ATTCC-3′-

BHQ2

B. Track strands

TwT = D5+D4+D5′ (15+75+15 = 105 mer):

5' - GCACAAGTAATCGCT+GCTATAATGGCTGGGGCTTTGTCATGC

AAAATACTACGATCCCCTTGGACTAGCTCGGAGCCTCTCGCAGAAA

TT+CGAACATTGCTGTTG-3'

TL = D4* (75 mer):

5′- AATTCTGCGAGAGGCTCCGAGCTAGTCCAAGGGGATCGTAGT

ATTTTGCATGACAAAGCCCCAGCCATTATAGC-3′

TBM1 = D1*+D5′*+D2* (6+15+20 = 41 mer) with dye:

TAMRA-5′-

GGAATG+CAACAGCAATGTTCG+GGTATATCTCCTTCTTAAAG-3′

TBM2 = D1*+D5′*+D2* (6+15+20 = 41 mer) with dye:

FAM-5′-

GGAATG+AGCGATTACTTGTGC+GGTATATCTCCTTCTTAAAG-3′

Chapter 4   A Bio-mimicking Enzymatic Nanowalker of High Fuel Efficiency

4.1   Introduction

Nanotechnology has long pursued the invention of rationally designed nanowalkers (*11–15, 17–19, 22–25, 27, 28, 101, 107*) to replicate the chemically powered biomotors that autonomously transport cargos in the cell. The biomimetic systems also will provide an access to the science governing efficient chemical energy utilization at a single-molecule level, which is important to nanotechnology and energy technology but remains difficult to decipher from the complex bio-systems. Indeed, the biomotors consume one fuel molecule at a time, and may convert the chemical energy to work by ~ 100% efficiency (*54*) or drive directional motion up to one forward step per fuel molecule (*45*). Furthermore, the biomotors are enzymes in the strictest sense as they catalyze fuel reaction without changing themselves and tracks, thus enabling repeatable transport seen in biology but yet to be done by synthetic motors. Chemically powered synthetic nanowalkers reported to date are predominately burn-bridge motors (*13–15, 17, 22, 27, 28, 101*) that consume the traversed track in an unrepeatable, domino-like chemical cascade.

An enzymatic nanowalker beyond the burn-bridge design was reported in 2009 by Bath et al. (*18*); but each forward step costs no less than two fuel molecules, which turns out to be a general threshold (*127*) for nanomotors. And sustainable motion by any synthetic enzymatic motor has yet to be demonstrated since this walker relies on a soft, single-stranded DNA track that coils to halt the walker between non-adjacent binding sites. Six years after its publication, the motor of Bath et al. remains the sole synthetic system qualified as a strict enzymatic nanomotor. This fact reflects some obstacles impeding this important research direction. One major obstacle is to find generally applicable physical mechanisms for harvesting chemical energy at single-molecule level. These mechanisms should be scientifically advanced to break the two-fuel-per-step threshold and facilitate sustainable autonomous motion. We report here a new enzymatic nanowalker that meets the requirements by replicating key mechanistic features of biomotors.

4.2   Motor design

The walker is a DNA biped made of a 7 nm double-helix bridge connecting two identical single-stranded legs (Figure 4.1A). The track is a double helix hosting identical binding sites, spaced ~ 20 nm apart, with each site comprising two single-stranded segments ~ 5 nm apart (D1* and D2*′, with the D2*′ to D1* pointing to a unique end of the track, henceforth termed "plus end"). Each leg of the motor can bind to a site by forming two helices

(D1-D1* and D2-D2*′, ~ 2 and 5 nm long respectively). Should either helix break, a single-stranded fuel can perform a toehold-mediated strand displacement to dissociate the leg from the track. The leg-bound fuel is then recognized and cut by nicking enzyme N.BbvC IB (*18*), which is prevented from cutting the track via a point mutation (*18*) in D2*′. The motor and track were self-assembled from constituent DNA strands and confirmed by native PAGE. The experimental methods is described in section 4.4 and DNA sequences is given in section 4.7.
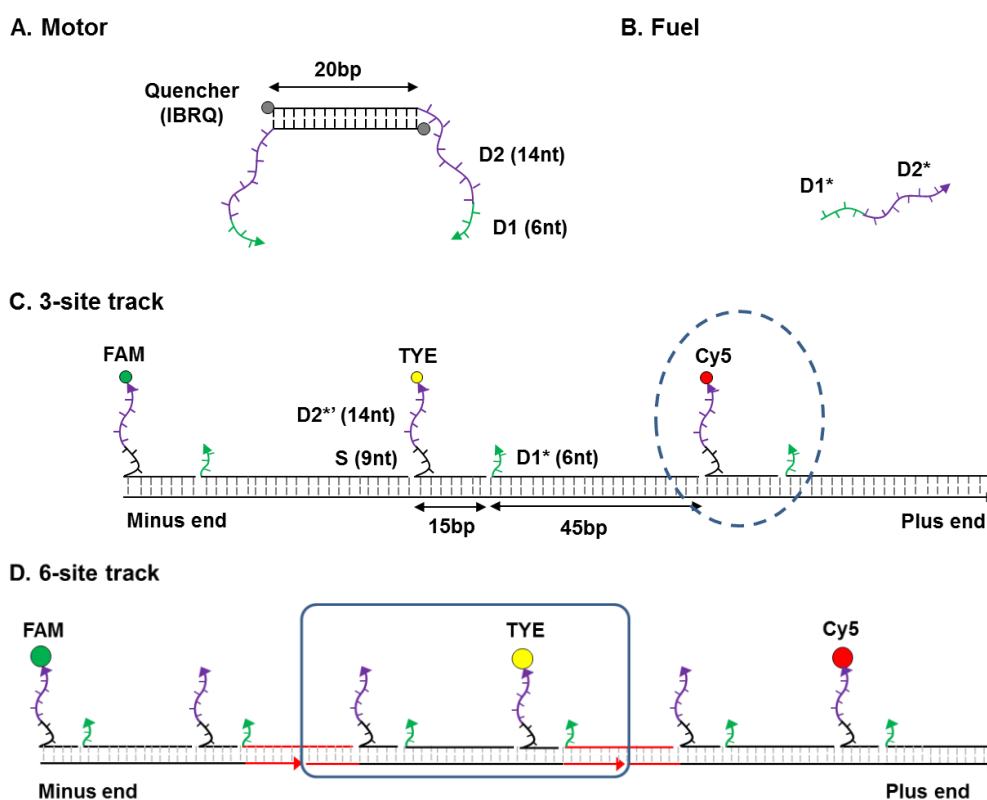
Figure 4.1 Motor and tracks design. Asterisk (*) marks complementary sequences; "nt" marks nucleotides in single-strand DNA. The track carries three fluorescent dyes (colored spheres) at different composite site (dashed circle); the motor carries two quenchers (dark grey spheres).

For characterization purpose, the track carries three different fluorescent dyes (colored spheres in Figure 4.1C) at each D2*′ segment and the motor carries two quenchers so that the leg-track binding subjects a dye to a ~ 100% effective contact quenching (*153*). Figure 4.1D shows the six-site track designed for testing the sustainable motion of the motor. The track is labelled with three different fluorescent dyes at the 1st site located at the minus end, the 4th site, and the 6th site at the plus end, respectively. The track is formed by connecting three modules with each module holds two composite binding sites (the rounded rectangle surrounds one module). To precisely control the track length, the sequences of the two ends (shown in red) of each module are different. The sequences of the middle part (shown in black) of each module are the same (except for the strands holding specific dye molecules). This modular design can be used for devising even longer track.

4.3 'Gated' chemomechanical coupling

The motor is designed to move directionally via three automatic gating mechanisms regulating leg-track interaction and fuel turnover. Following biomotor studies (*71*), 'gating' means a physically coordinated stalling of one motor leg in a specific mechanochemical state until a certain 'gatekeeper' process is completed – often at the other leg.
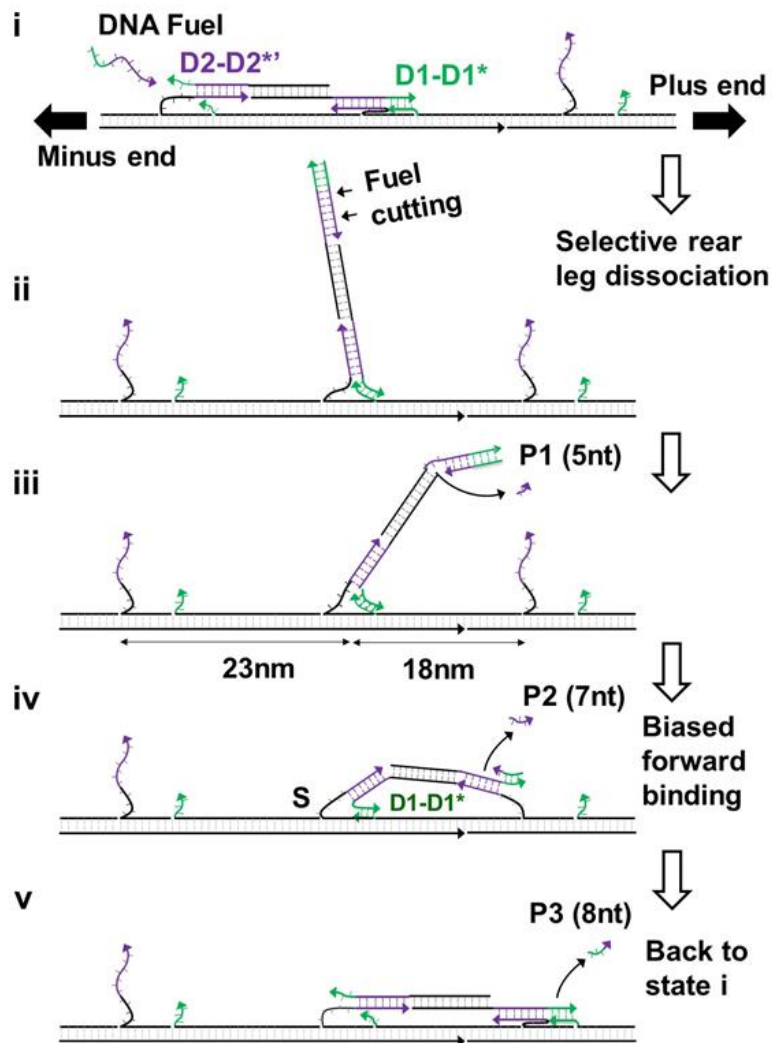
Figure 4.2 Operation mechanism of the motor. Asterisk (*) marks complementary sequences, 'nt' for nucleotides and 'bp' for base pairs.

Gating I: Fuel binding to a track-bound leg and the ensuing leg dissociation are gated by the other leg's forward binding to the track. This gating is site-selective because the track-bound leg is fully protected in a single-leg motor-track binding state, but the short D1 segment – a recognition site for the fuel – is exposed preferentially at the rear leg over the front leg in a two-leg state due to a mechanical asymmetry between the two legs. By its

small size, the motor needs be fully stretched to form a stable two-leg state, resulting in a nontrivial intra-motor stress (see Figure 4.2, state i). The stress pulls the front leg's D1-D1* and D2-D2*′ helices collinearly backward in a shearing mode, which known to require a large force (*157*) for duplex breaking. But the two helices are bent at the rear leg because its D2-D2*′ is pulled forward but the D1-D1* remains backward (state iv). This twists the rear leg into a loop-like form, which requires minimally ~ 4 nucleotides (*158*) in the single-stranded form due to DNA rigidity. Hence the 6 base-pairs long D1-D1* is readily broken for fuel binding at the rear leg but not the front leg.

Gating II: Leg-track binding is gated by controlled product release – again with a site-selectivity that ensures preferential leg binding to the front site over the back site. The fuel's cutting by the nicking enzyme are so arranged that a 5 nt-long product (P1 in Figure 4.2) and a 7 nt-long product (P2) cover the leg's D2 segment, and a third, 8 nt-long product (P3) covers the D1 segment plus the two adjacent nucleotides of D2. The hybridization free energy for the products and the leg is ~ 8.6, 15.2, 12.7 $k_B T$ for P1, P2, and P3, respectively, as predicted from the DNA nearest-neighbour thermodynamics (*154*) for the experimental temperature (T = 25 °C, k_B is Boltzmann constant). The free-energy gaps between the duplexes suggest that the shortest P1 is released from the leg by thermal fluctuations before P2 and P3 on average. The diffusing leg free of P1 but still retaining the longer products can hybridize with the D2*′ overhang of the front site but not the equally distant

D1* at the back site, while the back site's D2*′ is ~ 5 nm further than the front site's D2*′ from the track-bound leg (counted from the leg's D1-D2 junction, see state iii). Hence the diffusing leg binds preferentially forward.

Gating III: Full product release is gated by consolidated forward leg binding. The two longer products (P2, P3) are actively displaced as the D2*′ and D1* overhangs complete their hybridization with the incoming leg. This suppresses premature fuel turnover at the diffusing leg independent of the motor's motion, thereby prohibiting uncontrolled decay of the chemical energy into heat.

The three gatings ensure a coordinated chemomechanical cycle that facilitates autonomous and sustainable walking of the motor towards the plus end. Gating I causes an asymmetric state (state i) in which the fuel preferentially dissociates the rear leg instead of the protected front leg (by D1* or fuel products). In the ensuing single-leg state (states ii, iii), the diffusing leg undergoes fuel cutting and binds preferentially to the front site after spontaneous P1 release (gating II). The forward binding creates a new two-leg state in which the previously front leg becomes a twisted rear leg (state iv). The complete D2-D2*′ hybridization at the front leg raises the inter-motor stress to expose the rear leg for fuel recognition, bringing the motor back to the initial state i after P2 and P3 dissociation. The full chemomechanical cycle i→ii→iii→iv→i consumes one fuel molecule and translocates the motor a

step to the plus end. The motor's processive stepping is ensured by gating I that suppresses fuel-induced derailment from a single-leg state. Gatings I, III combine to delay the enzymatic cycle of the front leg relative to the rear leg – a feature called 'alternating catalysis' for biomotors (*69*) and proven crucial for processivity of bipedal enzymatic motors. The motor's sustainable walking is further supported by the double-stranded track, which is rather rigid despite the presence of nicks as found by previous studies (*159*) of nicked DNA.

The leg-track binding configuration obtained from oxDNA (see section 4.4.4 for details) confirms that the leg is bent at the junction of D2-D2*' and D1-D1* duplexes when the D2-D2*' tilts towards the plus end (e.g., as caused by the other leg's forward binding). The probability for pulling force-induced breaking of any base pair in the D1-D1* duplex is higher for forward pulling than backward pulling for each value of force simulated (0, 2, 5, 10, 20 pN in Figure 4.3). The forward-to-backward ratio of base pair breaking is ~ 8 for 5 pN and ~ 7 for 10 pN. The results confirm that the D1-D1* duplex is far more likely to be dissociated on the rear leg than the front leg when the motor forms a two-leg binding with the track. Moreover, the disparity of base-pair breaking probability for forward pulling versus backward pulling is far larger for the triplet adjacent to the D2-D2*' duplex than the other triplex of the 6-bp D1-D1* (Figure 4.4). This supports the bending-induced D1-D1* dissociation in which the largest destabilizing effect is felt in the vicinity of the twisted junction of the D1-D1* and D2-D2*' duplexes.
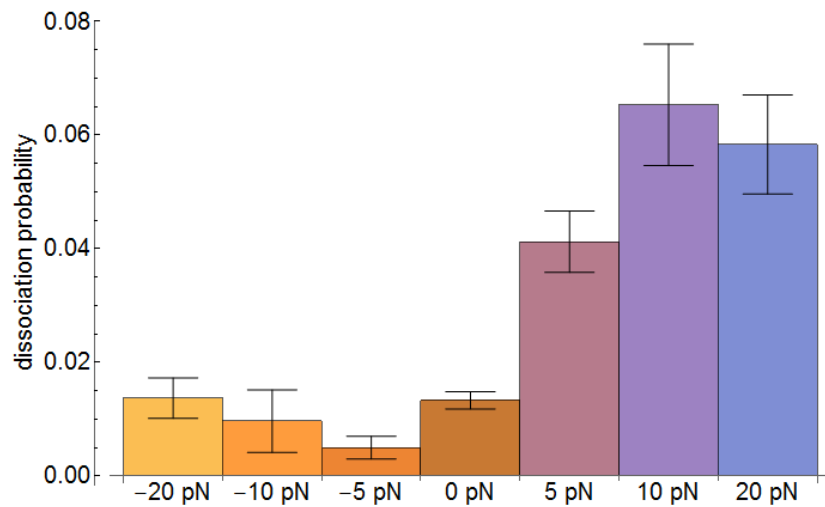
Figure 4.3. Dissociation probabilities obtained from Monte Carlo simulation of the leg-track binding complex under different values of pulling force. Shown are the probabilities for breaking of any base pair of the D1-D1* duplex. Forces directed towards the track's plus (minus) end are labelled as positive (negative).
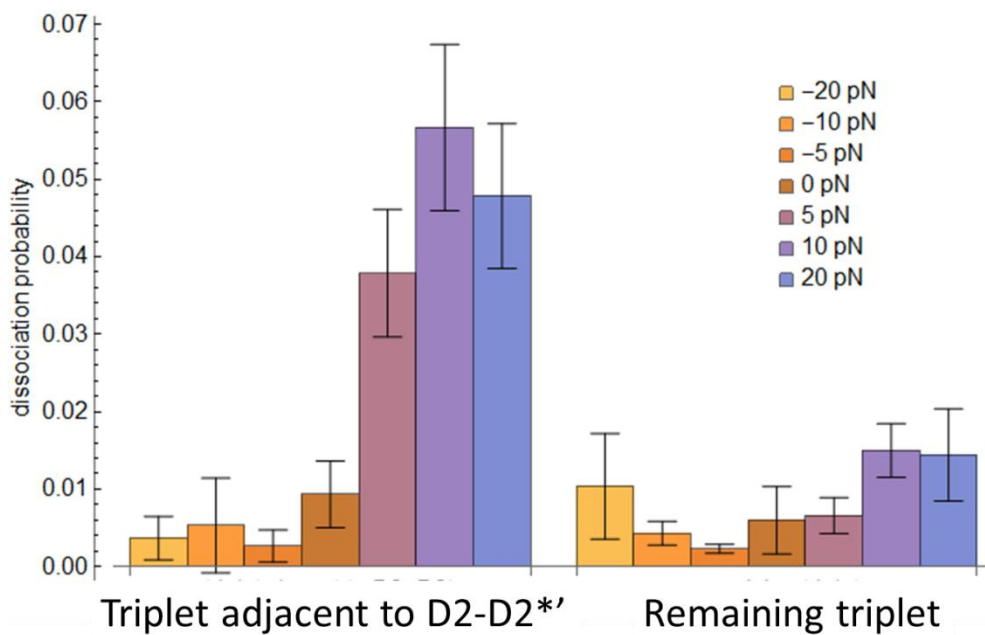
Figure 4.4. The probability for breaking of any base pair within each of the two triplets of the D1-D1* duplex.

4.4   Materials and Methods

4.4.1   Motor-track fabrication

The nucleotide sequences for the double-stranded backbone of tracks were taken from lambda DNA; the sequences for the motor and other parts of the tracks were generated using CANADA software (*130*). The secondary structures were checked using Mfold (*131*) (for single strands) and NUPACK (*132*) (for motor/track formation), with unwanted structures removed by manually adjusting the sequences. The motors and tracks were fabricated separately using constituent DNA strands (from Integrated DNA Technologies, Inc.). The strands were mixed stoichiometrically at 5μM in TE buffer containing 10 mM Tris-HCl, 1 mM EDTA, 200 mM NaCl (or 400 mM NaCl for 6-site tracks). The mixed samples were incubated in a heating block, and gradually cooled down from 95°C to 20°C over a period of 14 hours using PCR (C1000 Touch™ Thermal Cycler, Bio-Rad). The PCR annealing protocol is shown in Figure 4.5. The final products were analyzed using 10% native polyacrylamide gel electrophoresis (PAGE) against a low molecular weight DNA Ladder (New England BioLabs, Inc.).

Temperature (°C)	Time (min)	Temperature (°C)	Time (min)	Temperature (°C)	Time (min)	Temperature (°C)	Time (min)
95	20	75	60	55	60	35	60
90	20	70	60	50	60	30	60
85	20	65	60	45	60	25	60
80	60	60	60	40	60	20	60

Figure 4.5 PCR annealing protocol

4.4.2 Motor operation and fluorescence detection

For motor operation, an equimolar mix of motor/track was prepared at submicromolar concentrations in a buffer containing 40 mM Tris, 20 mM acetic acid, 2 mM EDTA and 12.5 mM magnesium acetate (pH 8.0). The mixed sample was incubated for at least 15 hours to ensure thermodynamic equilibration before operation. A fuel-enzyme mix was separately prepared from 100 µM stock solution for the fuel (TE buffer) and 3.25 µM N.BbvC IB enzyme with specific activity 48,000 units/mg (New England BioLabs, Inc.). The motor operation was started by quickly mixing the fuel-enzyme with the incubated motor-track sample, and was monitored by detecting fluorescence from track-tethered dyes with a Cary eclipse spectrophotometer (Varian, Inc.; kinetic mode, at excitation/emission wavelength of 495 nm/520 nm (FAM), 549 nm/563 nm (TYE) and 648 nm/668 nm (CY5)). The sample incubation and later operation were all done at 25 °C.

Adding the fuel-enzyme and their associated buffer to the motor-track sample affects the optical properties of the dyes. This effect is removed by dividing the fluorescence from an operation experiment by that from the corresponding control experiment, carried out using the same procedure of fuel-enzyme addition and fluorescence detection, but with the solution containing the same amount of tracks without any motor. The control-calibrated fluorescence also removes the influence of photobleaching (a negligible effect in this study as confirmed by the control experiments).

4.4.3 Extracting occupation probability, translocation probability, speed, and rate ratios from the control-calibrated fluorescence data

Following a previous study (*107*), the probability for a site to be occupied by a motor is related to the fluorescence of the dye tethered to the site as

$$P(t) = \frac{1}{\gamma}\left[1 - \frac{I_{MT}(t)}{I_T(t)}\right] = \frac{1}{\gamma}[1 - I_M(t)] \tag{1}$$

Here, $I_M(t) = I_{MT}(t)/I_T(t)$ is control-calibrated fluorescence, $I_{MT}(t)$ is the fluorescence collected from an operated motor-track sample at a time t, $I_T(t)$ is the fluorescence of an equal amount of bare tracks from the accompanying control experiment, γ is the quenching efficiency of the dye by

the motor-carried quencher. $\gamma = 1$ holds for all the three dyes due to their ~ 100% effective contact quenching (*153*).

The change of occupation probability from time t_1 to a later time t_2 is

$$\Delta P = P(t_2) - P(t_1) = \frac{I_M(t_1) - I_M(t_2)}{\gamma} \qquad (2)$$

The rate for leg dissociation off a site from t_1 to t_2 is

$$r_d = -\frac{\Delta P}{t_2 - t_1} = \frac{I_M(t_2) - I_M(t_1)}{\gamma(t_2 - t_1)} \qquad (3)$$

For motor operation on a fully labelled 3-site track, the rate for overall leg dissociation off track (shown in Figure 4.9A) is

$$r_{d,tot} = r_{d+} + r_{d-} + r_{dm} \qquad (4)$$

in which the subscripts $+$, $-$ and m mark the plus-end site, minus-end site and the middle site. The probability for a motor initially at the minus end to translocate to the plus end (shown in Figure 4.9B) is

$$P_{trans} = \frac{\Delta P_+}{P_-(t_1)} = \frac{I_{M+}(t_1) - I_{M+}(t_2)}{1 - I_{M-}(t_1)} \qquad (5)$$

The average speed of the motor's fuel-driven translocation is

$$v = \frac{P_{trans} \times d}{n_f} \qquad (6)$$

in which d is the motor's step size and n_f is the number of fuel molecules consumed per motor. The v data shown in Figure 4.10A are a lower limit obtained using the supplied fuel molecules per motor, which is an upper limit of n_f. The rate ratio for leg dissociation from the minus-end site over the plus-end site (Figure 4.12A-C), is

$$\alpha = \frac{r_{d-}}{r_{d+}} = \frac{\gamma_+}{\gamma_-} \left[\frac{I_{M-}(t_2) - I_{M-}(t_1)}{I_{M+}(t_2) - I_{M+}(t_1)} \right] \tag{7}$$

Similarly, the rate for leg binding from t_1 to t_2 is

$$r_{b\pm} = \frac{P_\pm(t_2) - P_\pm(t_1)}{(t_2 - t_1)} = \frac{I_{M\pm}(t_1) - I_{M\pm}(t_2)}{\gamma(t_2 - t_1)} \tag{8}$$

and the rate ratio for leg binding to the plus-end site over the minus-end site (Figure 4.13C, D and Figure 4.14C) is

$$\beta = \frac{r_{b+}}{r_{b-}} = \frac{\gamma_-}{\gamma_+} \left[\frac{I_{M+}(t_1) - I_{M+}(t_2)}{I_{M-}(t_1) - I_{M-}(t_2)} \right] \tag{9}$$

Thus the probability occupation change ΔP, overall dissociation rate $r_{d,tot}$, translocation probability P_{trans}, speed v, and rate ratios α and β can be extracted from the control-calibrated signal $I_M(t)$.

4.4.4 Computer simulation of motor-track binding (performed by Tee Shern Ren)

The oxDNA coarse-grained simulation package (*160*) was used to simulate a leg (i.e., the 20 nt-long D1-D2 segment) bound with the middle site of a 3-site track at the experimental temperature (25 °C). To exert a pulling force to the leg, we applied two harmonic traps ~ 12 nm apart to immobilize a 35-bp segment of the track that sandwiches the 15-bp binding site in the middle. Following ref. (*161*), a Monte Carlo simulation was done to sample base-pair breaking events at the leg-site complex under a forward or backward force, which is parallel to the track segment and placed at the other end of the D2-D2*' duplex to model the intra-motor stress in a two-leg state. Monte Carlo simulations of ~ 10^8 steps were performed for each value of force (results shown in Figure 4.3 and Figure 4.4).

4.5 Results and Discussions

4.5.1 Motor-track formation

The motor and track were self-assembled from constituent DNA strands and confirmed by native polyacrylamide gel electrophoresis (native PAGE), with the sequences of the strands given in section 4.7. To measure the motor's performance and elucidate its working mechanisms, the motor and a few variants/mutants were operated on an extensive, six-site track as well as on truncated three- and two-site tracks. The six-site track follows the design shown in Figure 4.1D, while the three- and two-site tracks follow a similar design except for use of a single-stranded template to form the track's entire helical backbone hosting the binding sites. Each of the motors and tracks was assembled through a single-pot annealing at a low cooling rate (~ 5.4 °C/hour from 95 °C to 20 °C, see section 4.4.1 for details). The typical gel images of the assembled motors and tracks are shown in Figure 4.6 below. In almost every case, the annealing method resulted in a single prominent band that can be identified as the targeted product by molecular weight comparison. For example, the motor band is slightly lower in molecular weight than an elongated variant; the track bands lie far above and follow the right order according to their lengths; and the track template is lower than the corresponding track product.

I.   Native motor
II. Elongated motor variant
III. 6-site track
IV. 3-site track
V. Mutated motor
    (for binding experiments)
VI. 2-site track
VII. Mutated 3-site track
    (for binding experiments)
VIII. Mutated elongated motor
    (for binding experiments)
IX. Longest template (180 nt)
    for 3-site track
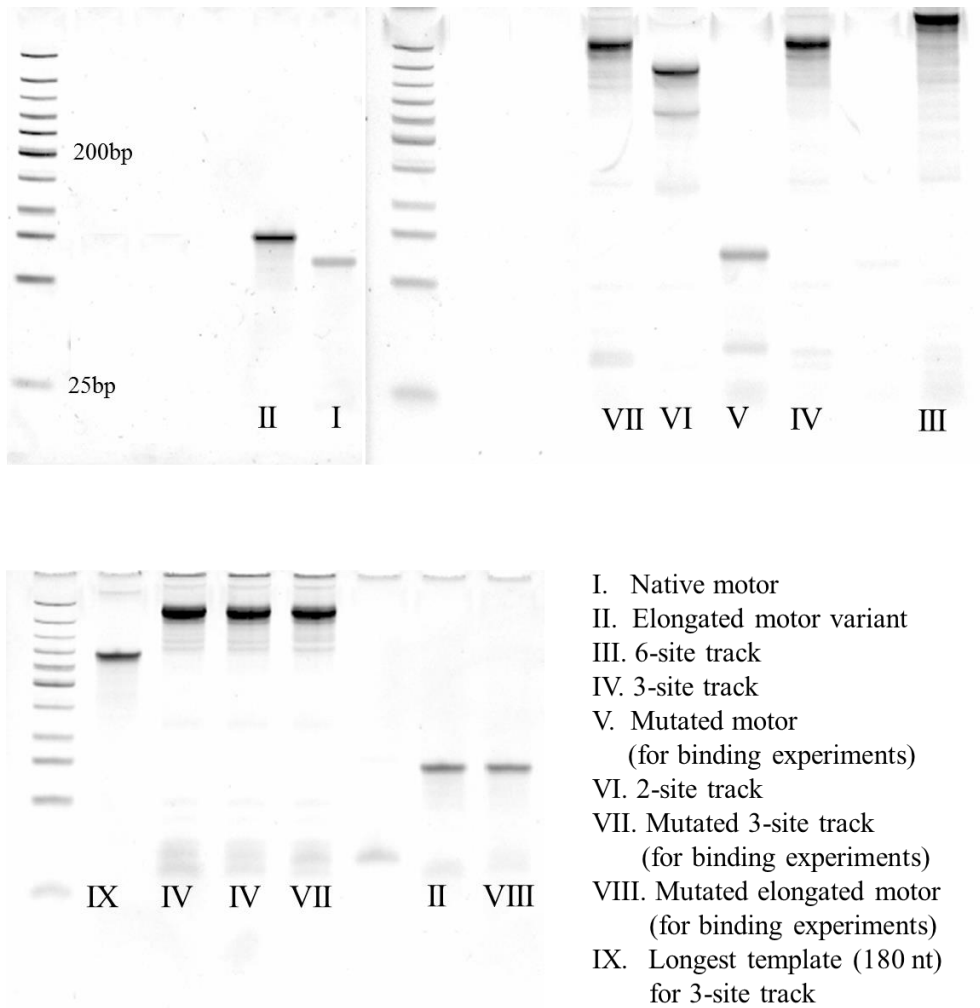
Figure 4.6. Native PAGE gel images for motors and tracks. The leftmost lane of each gel image is the low molecular weight DNA ladder (purchased from New England BioLabs Inc., with 25 bp and 766 bp as the lowest and highest band).

4.5.2 Sustainable directional motion

Figure 4.7 Motor operation on a 6-site track. (A) The fluorescence signals calibrated against a bare-track control experiment indicate the motor's plus-end-directed motion. (B) The change of occupation probability at individual sites, which is extracted from fluorescence in A. The fuel was added twice for the 6-site operation (each at a ratio of one fuel per motor). (C) The average change of occupation probability per site of the motor during operation. The shown results are obtained by averaging the data in B. The concentrations used are: 40 nM motor/track, 560 nM enzyme.

The motor's sustainable motion was tested by operating it on a six-site track. Adding the fuel and enzyme to a long incubated equimolar motor-track mix started the motor's operation, which was monitored by fluorescence detection. Each operation is compared to a control experiment in which the same procedure of fuel/enzyme administration and dye excitation was applied to an equal amount of tracks without any motor. The fluorescence of the operated motor-track mix divided by that of the bare tracks yields site occupation by the motor, which increases most at the plus end, increases moderately at the intermediate site, and decreases at the minus end (Figure 4.7A, B). This trend indicates a processive motor flow across these three sites towards the plus end. The same trend is observed upon a second addition of fuel, demonstrating repeatability of the motor's operation. The average occupation over the three sites reaches a final value after operation which is close to the initial value (Figure 4.7C), indicating a negligible derailment of the motor throughout the operation. The on-track flow and low derailment support the motor's processivity, and thereby gatings I, III. The motor was also tested on a truncated three-site track with each site labelled by a dye. The motor's direction and a low derailment are confirmed again (Figure 4.8A-F).
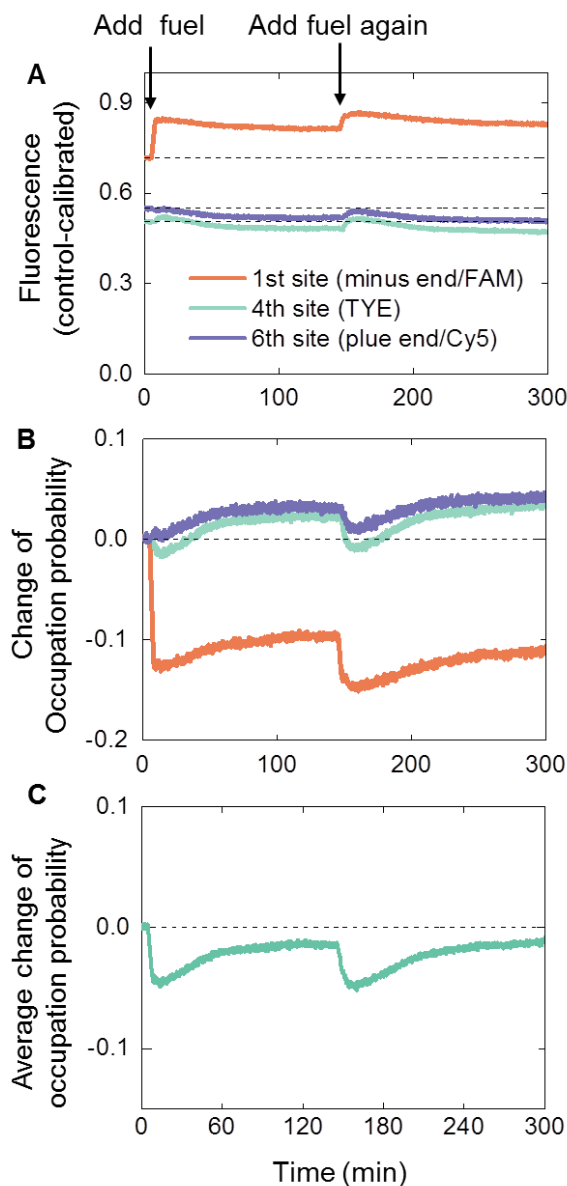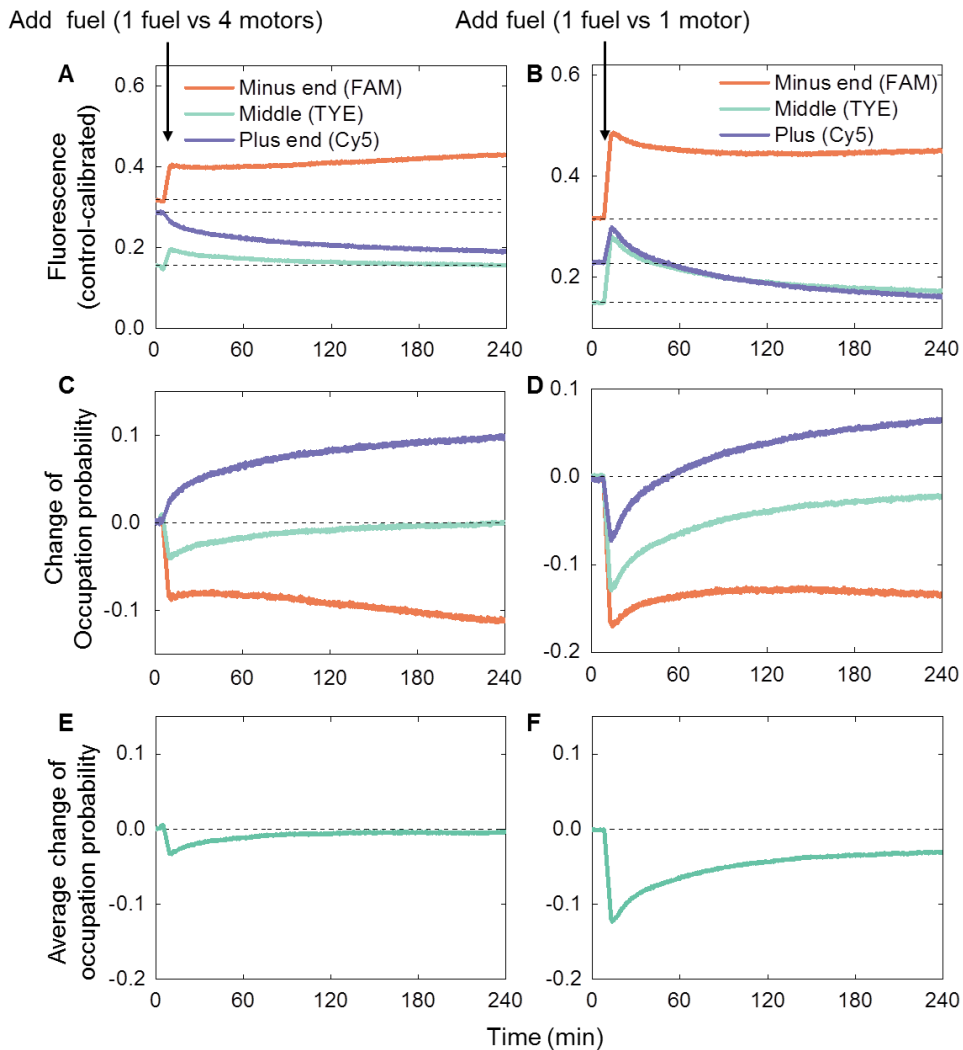
Figure 4.8 Motor operation on a 3-site track. (A, B) The fluorescence signals calibrated against a bare-track control experiment indicate the motor's plus-end-directed motion. (C, D) The change of occupation probability at individual sites, which is extracted from fluorescence in upper ones. (E, F) The average change of occupation probability per site of the motor during operation. The shown results are obtained by averaging the data in C, D respectively. The concentrations used are: 80 nM motor/track, 560 nM enzyme.

4.5.3 Stepping fidelity and Speed

Notably, the middle-site signal (hence the site's occupation) recovers to the initial value quickly, especially for a low initial fuel concentration (Figure 4.8A, C). This feature suggests that the fluorescence drop and rise at the plus and minus ends are caused primarily by a full-step, minus-to-plus end swing of the motor. This offers a chance to estimate the motor's fidelity and speed for minus-to-plus translocation. Motor operation on this fully labelled track offers many details of the motor's working mechanisms.

Following the control-calibrated signal in Figure 4.8A, the plus-end drop yields the net increase of leg population, which is ~ 0.1 at the end of operation. The initial motor population bound between the minus-end site and the middle site is the initial minus-end value of the control-calibrated signal subtracted from one (~ 0.68). Since the motor's actual fuel consumption is capped by the fuel supply (i.e., one fuel molecule per four motors), the fidelity of a motor making a full-step translocation to the plus end, per fuel molecule consumed, is at least $D = 0.1 / (0.68 \times 1/4) = 58.8\%$.

The motor's rate for overall leg dissociation immediately following fuel addition rises linearly with the initial fuel concentration (Figure 4.9A), consistent with fuel-induced leg dissociation. The minus-to-plus translocation probability (i.e., net increase of the plus-end population divided by the initial

minus-end population) follows a Michaelis-Menton-like saturation with increasing enzyme concentration (Figure 4.9B).
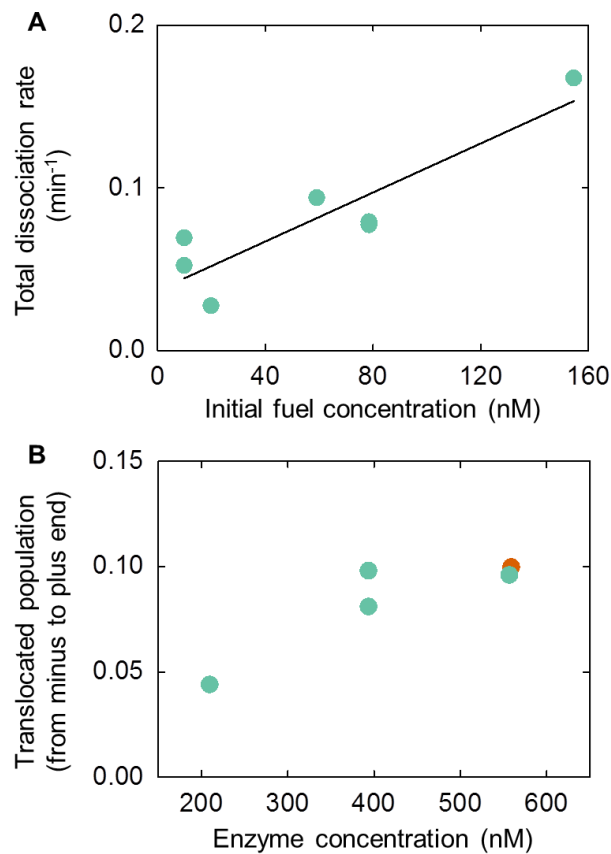
Figure 4.9 Motor dissociation rate and translocation population. The data are for 80 nM motor/track, 560 nM enzyme unless stated otherwise. (A) The rate for overall dissociation off the track versus fuel concentration shortly after the fuel addition (i.e., the initial, highest fuel concentration for an operation experiment). The rate data are obtained by summing slopes of three dyes in Figure 4.8A, B from the last data point before the fuel addition to the first data point after. The line is a linear fit to the data. (B) The probability for a motor initially located at the minus end to translocate to the plus end throughout an operation. The translocation probabilities are extracted from the fluorescence signals obtained at different enzyme concentration but for a fixed fuel-motor ratio (greenish blue for 1:1 and orange for 3:4).
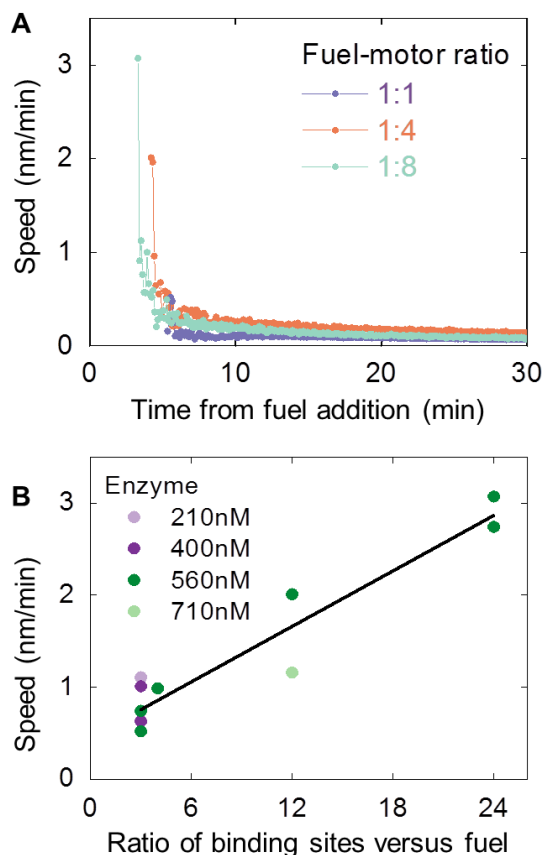
Figure 4.10 Motor speed extracted from operation on a fully labelled 3-site track. The data are for 80 nM motor/track, 560 nM enzyme unless stated otherwise. (A) Speed of fuel-driven translocation of the motor collected for the same enzyme concentration but different values of fuel-motor ratio. (B) The highest speed detected (i.e., the first data point after fuel addition in A) versus the ratio of the number of binding sites over the number of fuel molecules initially supplied in an operation. The line is a linear fit to all the data.

The speed of the minus-to-plus translocation drops quickly with fuel consumption (Figure 4.10A). The peak speed scales linearly with the number ratio of binding sites over supplied fuel molecules (Figure 4.10B). The highest detected speed is ~ 3 nm per minute, which is of the same magnitude as previously achieved by burn-bridge nanowalkers (*22, 101*). The present motor is limited by the enzyme turnover. The reported turnover rate (*145*) of ~

0.0037/s caps the motor's speed to ~ 4.5 nm per minute at best, which is 50% higher than the achieved speed. The low turnover rate is due to the enzyme's slow dissociation (*145*). But the fuel product release (and leg binding) might possibly occur before full dissociation of the enzyme from a leg, since a single enzyme likely catalyzes both cuttings by a sliding mechanism (*162*) due to the close proximity of the two nicking sites.

4.5.4   Preferential rear leg dissociation and its dependence on fuel

The preferential fuel binding to the rear leg and the resultant leg dissociation bias (i.e., gating I) are verified by the faster fluorescence rise at the minus end than the plus end shortly after the fuel addition, which is a common pattern of the six-site operation and the three-site operation (Figure 4.7 and 4.8). The same pattern was also observed in a specially designed dissociation experiment using a truncated track with only two binding sites (Figure 4.11B).
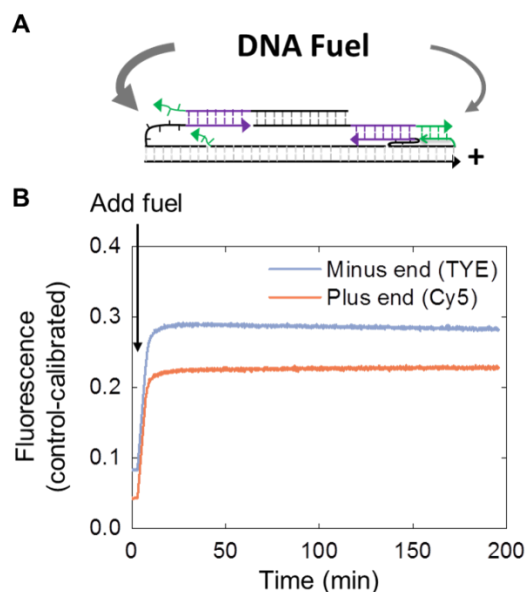
Figure 4.11 Bias for rear leg dissociation on truncated 2-site track. (A) Illustration of the motor's binding to the 2-site track, which is subjected to fuel dissociation. (B) Control-calibrated fluorescence data of a dissociation experiment in which a two-leg motor-track binding state (i.e., state i in Figure 4.2) was prepared on a truncated 2-site track (1:1 fuel-motor ratio, 100 nM motor/track).

This truncated 2-site track is designed to detect leg dissociation bias directly (Figure 4.11A) comparing with the operation experiments in which the dissociation events are from different two-leg bound motors on the same track. The track is fully labeled by two dyes, TYE and Cy5. Same as the previous operation experiments, equimolar motor and track samples were incubated before starting the dissociation experiment. Then the motor leg dissociation was triggered by quickly adding the fuel to the incubated motor-track sample. The fluorescence emitted from the two dyes were monitored.
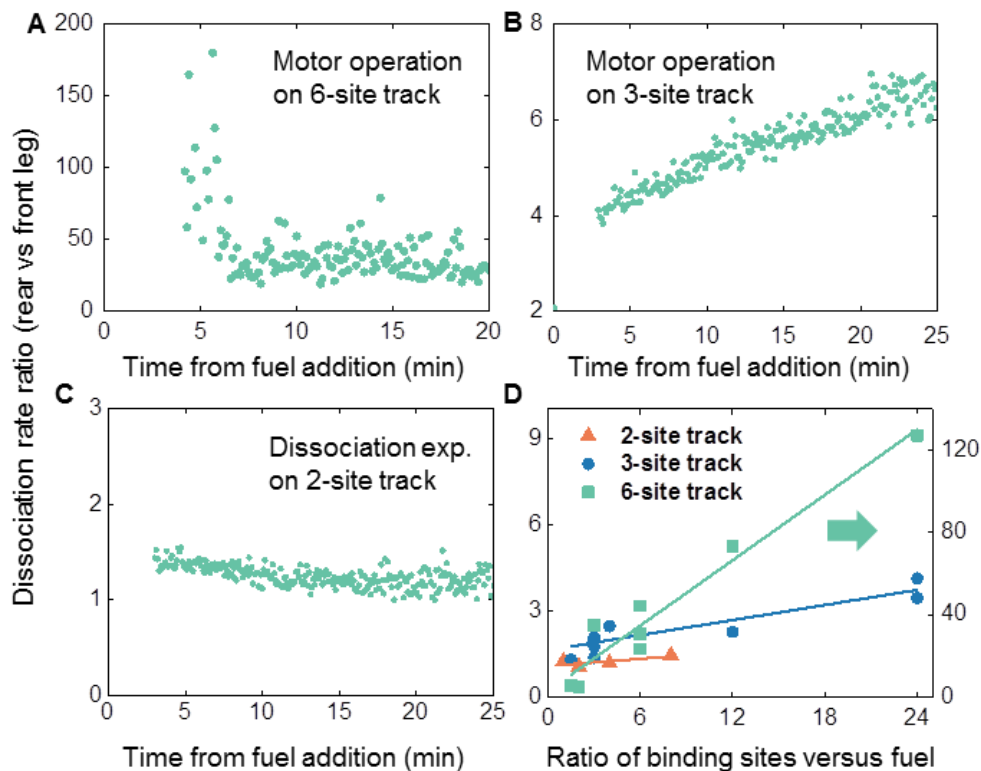
Figure 4.12 Bias for rear leg dissociation. (A-C) Rate ratios extracted from 6-site operation (1:4 fuel-motor ratio), 3-site operation (1:8) as in Figure 4.7 and Figure 4.8 respectively, and from a 2-site dissociation experiment (1:4 fuel-motor, 100 nM motor/track). (D) Average ratio over the first two minutes after fuel addition for the three types of experiments. The left vertical axis is for the 2-site and 3-site data, the right axis for the 6-site data. The lines are linear fits to each type of data.

For a quantitative analysis, the rate ratio of leg dissociation from the minus-end site over the plus-end site was deduced from the fluorescence slopes of the two-site, three-site and six-site experiments (Figure 4.12A-C). The average ratio over the first two minutes after fuel addition for the three types of experiments are summerized in Figure 4.12D. The minus-to-plus dissociation rate ratios deduced from all the three types of experiments are invariably above one in consistence with gating I (Figure 4.12). The highest ratio is above 100, which is the same level as for the motor of Bath et al. (*18*).

The rate ratios scale linearly with the site-fuel ratio for all the three types of experiments (Figure 4.12D), which explains the motor's speed scaling. The scaling is a feature of the ensemble experiments in which two-leg motor-track states occur over the entire track to share the fuel supply, hence reducing available fuels at individual sites.

4.5.5 Preferential forward binding and its dependence on enzyme

To study the leg binding bias, we prepared another motor with one D2 segment mutated to exclusively bind the middle site (mutated accordingly) of a three-site track (Figure 4.13A). This hetero-pedal motor was first mixed with fuels to cover the native leg; the mutated track was then added to bind the motor's mutated leg at the middle site. Adding enzyme triggers the native leg's binding to either plus or minus end.
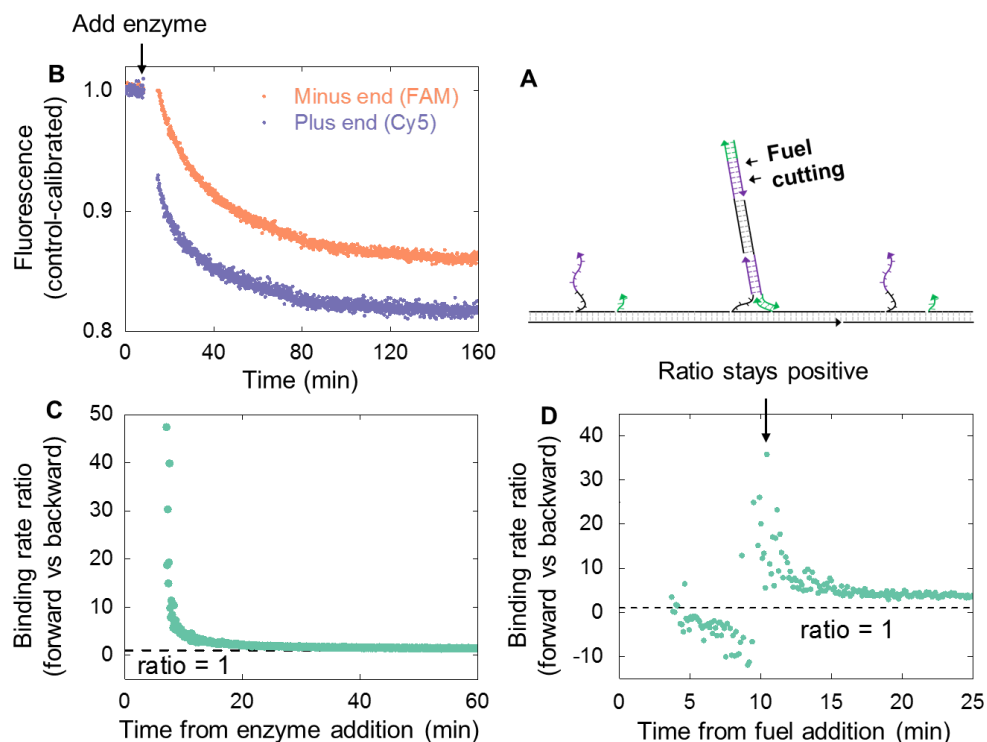
Figure 4.13 Bias for forward leg binding. (A) Illustration of the single-leg binding state of the hetero-pedal motor. (B) Control-calibrated fluorescence data from a binding experiment started from a single-leg state in the middle of a mutated 3-site track (80 nM motor/track, 560 nM enzyme). (C) Leg binding rate ratio of the plus-end site over the minus-end site extracted from B. (D) Rate ratio from 3-site operation as in Figure 4.8 but for 3:4 fuel-motor ratio.

The control-calibrated fluorescence decays faster at the plus end than at the minus end (Figure 4.13B), verifying the forward-biased binding and thereby gating II. The forward-to-backward binding rate ratio extracted from the fluorescence slopes is as high as 50 shortly after the enzyme addition, and drops quickly with decreasing single-leg population (Figure 4.13C). The binding bias is also reflected (*25*) in the different fluorescence decay at the plus and minus ends in the normal three-site operation; the extracted rate ratio has similar magnitude (Figure 4.13D). The binding rate ratio versus enzyme

concentration follows the same Michaelis-Menten-like pattern as for the translocation probability (Figure 4.14A).

4.5.6 Motor variants testing size dependence and fuel control
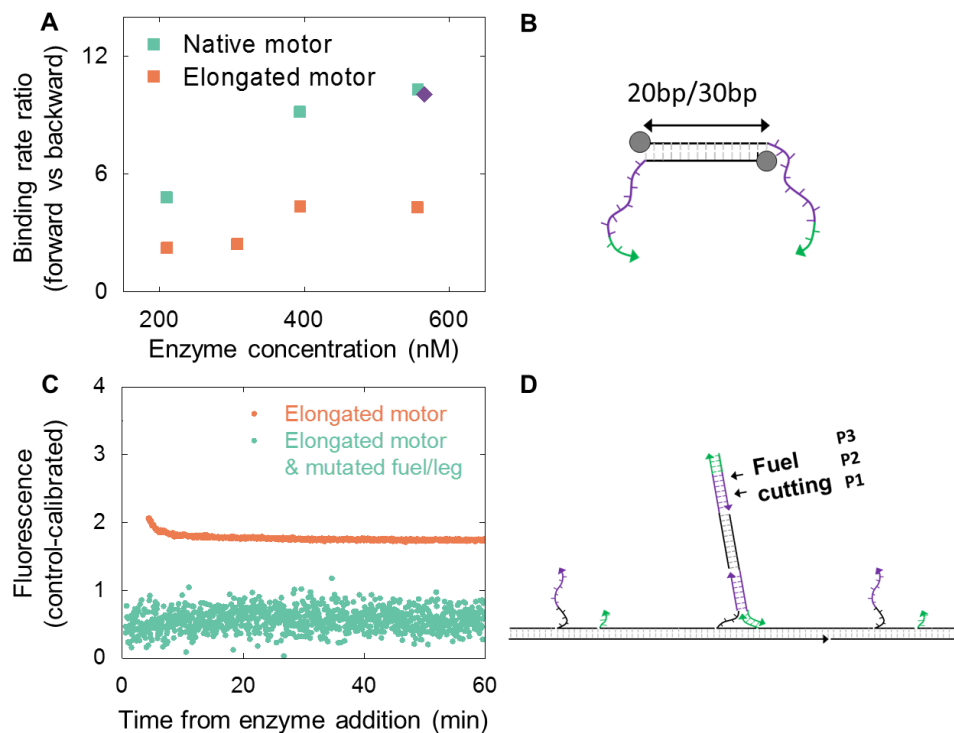
Figure 4.14 Comparisons of the forward leg binding bias of the motor variants with that of the native motor. (A) The average rate ratio (from 3-site operation) over the first two minutes after the rate ratio stabilizes to positive values. Squares are for 3-site operation (1:1 fuel-motor), diamond for the binding experiment in Figure 4.13C. (B) Illustration of the difference between the first motor variant and the native motor. (C) Binding experiments for the elongated variant (80 nM motor/track, 560 nM enzyme) and a second variant losing fuel control (83 nM motor/track, 325 nM enzyme). (D) Illustration of the relative position of the fuel remnants after enzyme cutting; P1 at the 3' end (indicated by arrow) and P3 at the 5' end of the fuel strand.

Three motor variants further elucidate the motor's working mechanisms. In the first variant, the duplex bridge is elongated to 30 bp. The

second variant has the elongated bridge plus mutations in the fuel and related motor-track segments to reverse the product control: P3 becomes the shortest (6 nt), versus a 7 nt-long P1 now and the same P2 as for the native motor. The hybridization free energy is ~ 7.6, 15.2, 13.7 k_BT for P3, P2, and P1 from the nearest-neighbour thermodynamics (*154*), suggesting earlier dissociation of P3 than P1 on average and hence the possibility of a backward leg binding to the D1* overhang.

The first variant has a lower forward binding bias than the native motor (Figure 4.14A), as the longer bridge allows more access to the rearward D2*′ overhang by the diffusing leg. For the variant with a reversed product control, the forward bias is further deteriorated and slightly reverses direction (Figure 4.14C). The bias difference between the two variants is an experimental evidence for effectiveness of the product control and its critical role in generating the forward binding bias.

The third motor variant introduces more flexibility into the two bridge-leg junctions by inserting four extra nucleotides (TTTT) at either junction (Figure 4.15A). This variant shows no improvement of performance (Figure 4.15B, C), suggesting that the mechanical flexibility necessary for the diffusing leg's binding to the track is not from within the motor but from the track-bound leg. The oxDNA simulation (performed by Tee Shern Ren) indeed finds a broad distribution of the D2-D2*' duplex of the track-bound leg under

zero pulling force at the operation temperature. The thermal fluctuations displace the duplex's mobile end (i.e., the end connects to the duplex bridge of the motor) from the mid-point between the D1* and D2*' overhangs up to ~ 5 nm backward and forward along the track. The flexibility is due to the flexible 9nt-long S segment as well as spontaneous breaking and re-formation of the short D1-D1* duplex as found in the simulation.
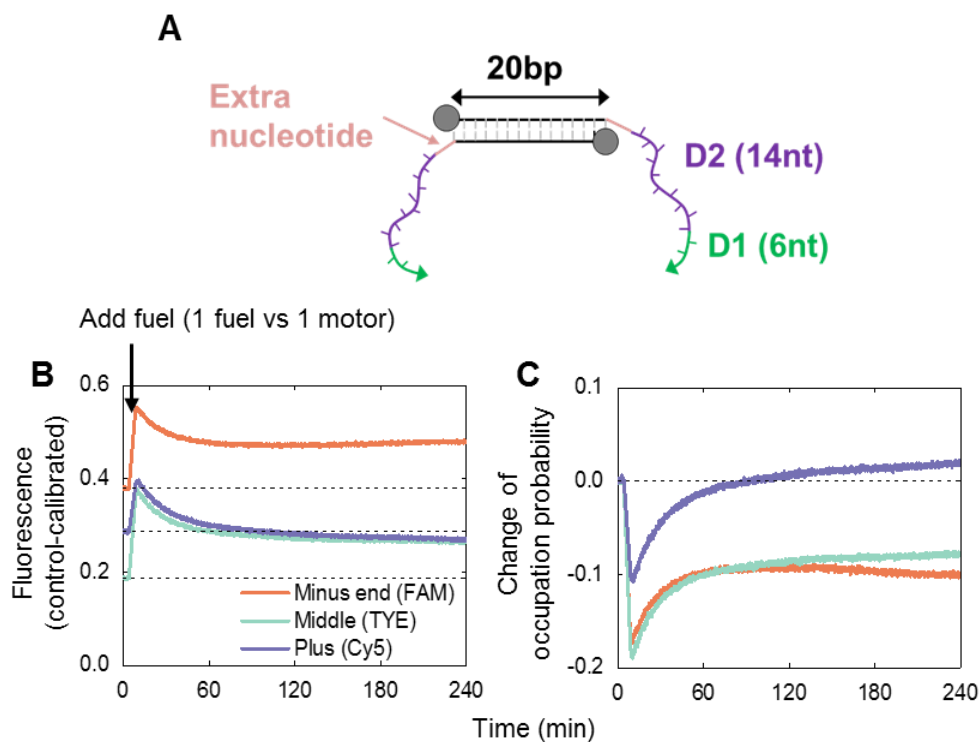
Figure 4.15 Operation of the third motor variant on a 3-site track. (A) Illustration of the third motor variant. (B, C) The operation procedure, fuel-motor ratio, concentrations for motor/track and enzyme are the same as for Figure 4.8B, D except for use of the motor variant.

The average displacement is ~ 1.4 nm backward, suggesting a ~ 20-degree back-tilting of the track-bound leg from the track's normal. However,

the back-tilting does not change the diffusing leg's preferential binding to the front D2*′ over the back one, since the motor, by its small size, hardly reaches either D2*′ at the tilting angle but must fall down to the the track in an almost parallel configuration to form the first 5 bp duplex with a D2*′over its P1* segment. This first contact requires that the remaining 18nt-long segment of the D2*′-S overhang is stretched to ~ 4.6 and ~ 9.7 nm for forward and backward hybridization, which implies a barrier reduction of ~ 10 – 16 k_BT from backward to forward hybridization from a rough estimation using a worm-like chain formula (eq.2 of ref. (*123*), with the previously reported contour length per nucleotide of ~ 0.63 – 0.70 nm (*155*, *163*) and persistence length of ~ 1 nm (*163*, *164*) for single-stranded DNA). A minor influence of the back-tilting is consistent with the observation that the forward binding bias prevails in the elongated motor variant, and becomes only slightly opposite in the variant of reversed fuel control.

4.5.7 Fuel efficiency

The measured dissociation rate ratios are essentially the probability ratio for the motor's rear leg dissociation over the front leg dissociation (α). Likewise, the binding rate ratios are the probability ratio for the dissociated leg to bind the front site over the back site (β). The measured stepping fidelity is the previously proposed concept of directional fidelity (*127*, *149*), which is defined as the probability for a motor's forward step minus that for backward

step divided by the total probability for forward, backward and futile steps. The directional fidelity D can be counted from α and β ratios by a simple stepping statistics: the probabilities for forward, backward and futile steps are $[\alpha/(1+\alpha)]\times[\beta/(1+\beta)]$, $[1/(1+\alpha)]\times[1/(1+\beta)]$, and $[\alpha/(1+\alpha)]\times[1/(1+\beta)]$ + $[1/(1+\alpha)]\times[\beta/(1+\beta)]$ (two terms for futile forward or backward step returning the motor to its previous location). Hence $D = (\alpha\beta-1)/[(\alpha+1)(\beta+1)]$, indicating symmetric and complementary roles of the dissociation and binding biases in producing a motor's direction. With either bias missing (i.e., $\alpha = 1$ or $\beta = 1$), a motor is capped to $D \leq 50\%$ and on average two fuel molecules or more must be consumed per forward step. This important limit, found general for nanomotors by previous studies (*127*), is now broken by our motor: the measured biases are up to $\alpha \sim 100$ and $\beta \sim 50$, potentially affording a D well above the experimentally deduced lower limit of $\sim 60\%$. We note that the necessity to integrate the two complementary biases to break the $D \leq 50\%$ limit does not imply that a power stroke must be included. This is because the forward binding bias ($\beta > 1$) may be realized by an apparently force-generating process (power stroke) or not.

Previous studies (*128*, *129*) found that the 2nd law of thermodynamics requires a least energy price for directional fidelity of isothermal nanomotors. A biomotor with $\sim 100\%$ efficiency evidently (*128*, *129*) exhausts the chemical energy to produce high directional fidelity at the

2nd law-decreed least price, with chemical energy-to-work conversion resulting from load-reduced direction. Hence a vital capability of efficient nanomotors is the effective channelling of fuel energy into directional fidelity, which can be achieved mechanistically via complementary dissociation and binding biases. The present motor powers both biases by a single fuel molecule through three gating mechanisms at major energy-releasing stages of the fuel turnover cycle, resulting in a controlled release of the chemical energy and its effective use for the motor's directional motion before decaying into random heat.

4.6 Summary of Chapter 4

A bio-mimicking enzymatic nanowalker that replicates key mechanistic features of biomotors was developed. The motor powers the two biases by a single fuel molecule through three gating mechanisms at major energy-releasing stages of the fuel turnover cycle, resulting in a controlled release of the chemical energy and its effective use for the motor's directional motion before decaying into random heat. This motor achieves a fuel efficiency of less than two fuel molecules consumed per productive forward step, thereby breaking a general threshold for chemically-powered machines invented to date. Like its biological counterparts, this rationally designed nanowalker realizes multiple gating-like controls over the fuel reaction and mechanical motion, offering rich mechanistic insights into how pure physical

effects enable effective harvest of chemical energy at the single-molecule level. As a genuine enzymatic nanomotor without changing itself nor the track, the walker demonstrates sustained motions on 6-site track. This opens the possibility of replicating the repeatable, efficient and automatic cargo transportation seen in biological intracellular transport but beyond the capacity of current burn-bridge motors.

4.7 DNA strands and sequences

The DNA strands forming the motors and tracks are all marked in Figure 4.16 Below are their sequences given in 5' to 3' direction. The asterisk * marks a complementary sequence.
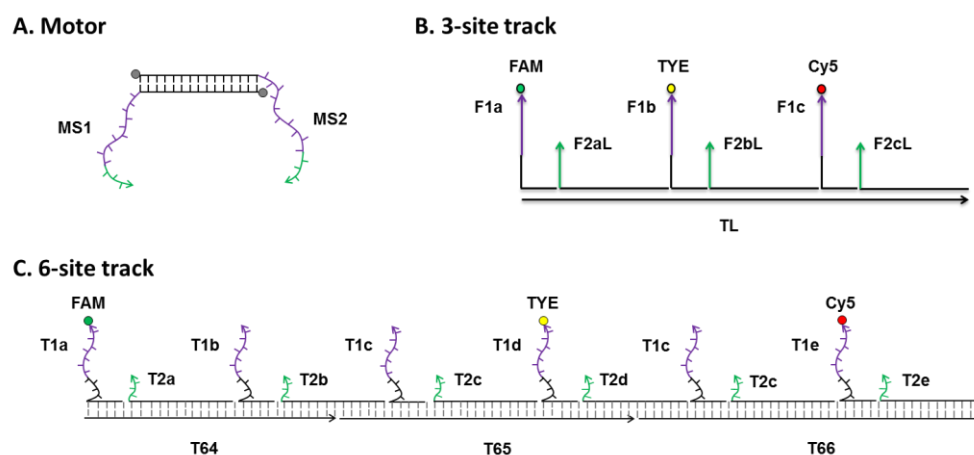
Figure 4.16 DNA strands for motors and tracks.

A. Motor strands

A1. The native motor

MS1 = IBRQ-M-D2-D1 (20+14+6=40mer):

5'-IBRQ-
TTACCATCTAGGTAGAGGCC+GCTGAGGGCTGAGG+TAAACT - 3'

MS2 = IBRQ-M*-D2-D1 (20+14+6=40mer)

5'-IBRQ-
GGCCTCTACCTAGATGGTAA+GCTGAGGGCTGAGG+TAAACT - 3'

A2. Mutated motor for forward binding experiments (Figure 4.13).

MS1 is unchanged but MS2 is mutated into a new strand MS2M = IBRQ-M*-D2M-D1. The mutated sequence is D2M = 5'- GGCGGTATGCATGGG - 3'.

A3. The 1st motor variant with an elongated bridge

MS1V1 = IBRQ-MV1-D2-D1 (30+14+6=50mer):

5'- IBRQ -GAGTTACCATCTAGGTAGAGGCCTCGTACA+GCTGAGGG CTGAGG-TAAACT - 3'

MS2V1 = IBRQ-MV1*-D2-D1 (30+14+6=50mer):

5'- IBRQ - TGTACGAGGCCTCTACCTAGATGGTAACTC+GCTGAGGG CTGAGG-TAAACT-3'

A4. The 2nd motor variant losing product control

MS1V2= IBRQ-MV1-D2-D1 (30+14+6=50mer):

5'- IBRQ – GAGTTACCATCTAGGTAGAGGCCTCGTACA+CTGCTGAG GGCTGA+GGTAAA-3′

MS2V2= IBRQ-MV1*-D2-D1 (30+14+6=50mer):

A5. The 3rd motor variant with extra linkers at leg-bridge junctions

MS1 = IBRQ-M-L-D2-D1 (20+4+14+6=44mer):

5'- IBRQ - TTACCATCTAGGTAGAGGCC+TTTT-GCTGAGGGCTGAGG +TAAACT - 3'

MS2 = IBRQ-M*-L-D2-D1 (20+4+14+6=44mer):

5'- IBRQ - GGCCTCTACCTAGATGGTAA+TTTT-GCTGAGGGCTGAGG +TAAACT - 3'

B. Fuel strand

Fuel= D1*-D2* (6+14=20mer): 5'-AGTTTACC^TCAGCCC^TCAGC-3'

(^ indicates cutting points by the nicking enzyme(*5, 6*) N.BbvC IB, which recognizes the 7-bp CCTCAGC sequence in the fuel-leg helix and catalyses hydrolysis of the fuel strand)

Muted Fuel for the motor variant losing product control:

5'-TTTACC^TCAGCCC^TCAGCAG-3'

C. Track strands

C1. Six-site track

T64 = D3+D4+D5+D6 (15+45+15+25=100mer):

5'-GATTTGCTGCTTTCC+ATTGAGCCTGTTTCTCTGCGCGACGTTCG
CGGCGGCACTTACGGA+GCTAATTCGGTCTCG+CACTTACGGCCAA
TGCTTCGTTTCG - 3'

T65 = D7+D8+D9+D10+D11 (20+15+45+15+25=120mer):

5'-TATCACCGACCGTCTTCTGC+CGTGTTTGTGCATCC+ATCTGGAT
TCTCCTGTCAGTTAGCTTTGGTGGTGTACCTTCTGCT+GTGGCAGTT
GTAGTC+CTGAACGAAAACCTCCAGCGATTGG - 3'

T66 = D12+D8+D9+D13+D14 (20+15+45+15+45=140mer):

5'- CACATTGGCACTTCAGGGCT+CGTGTTTGTGCATCC+ATCTGGAT
TCTCCTGTCAGTTAGCTTTGGTGGTGTACCTTCTGCT+AGAGCGTCA
CCTTCA+GTCAGTGCGTCCTGCTGATGTGCTCAGTATCACCGCCAGT
TGTCG - 3'

T2a = D4* + D1* (45+6=51mer):

5'- TCCGTAAGTGCCGCCGCGAACGTCGCGCAGAGAAACAGGCTCA
AT+AGTTTA - 3'

T2b = D7* + D6*+D1* (20+25+6=51mer):

5'- GCAGAAGACGGTCGGTGATA+CGAAACGAAGCATTGGCCGTAA
GTG+AGTTTA - 3'

T2c = D9* + D1* (45+6=51mer):

5'- AGCAGAAGGTACACCACCAAAGCTAACTGACAGGAGAATCCAG
AT+AGTTTA - 3'

T2d = D12* +D11*+ D1* (20+25+6=51mer):

5'- AGCCCTGAAGTGCCAATGTGCCAATCGCTGGAGGTTTTCGTTCA
G+AGTTTA - 3'

T2e = D14* + D1* (45+6=51mer):

5'- CGACAACTGGCGGTGATACTGAGCACATCAGCAGGACGCACTG
AC+AGTTTA - 3'

T1a = D3* + S + D2*′ (15+9+14=38mer, with underline in the D2*′ sequence marking a point mutation (*6*) that prevents the enzyme from cutting the track.

5'- GGAAAGCAGCAAATC+TTTTTTTTT+C<u>T</u>TCAGCC<u>T</u>TCAGC+FAM-3'

T1b = D5*+S+D2*′ (15+9+14=38mer):

5'- CGAGACCGAATTAGC+TTTTTTTTT+C<u>T</u>TCAGCC<u>T</u>TCAGC - 3'

T1c = D8* + S + D2*′ (15+9+14=38mer):

5'- GGATGCACAAACACG+TTTTTTTTT+C<u>T</u>TCAGCC<u>T</u>TCAGC - 3'

T1d = D10*+S+D2*′ (15+9+14=38mer):

5'- GACTACAACTGCCAC+TTTTTTTTT+C<u>T</u>TCAGCC<u>T</u>TCAGC+TYE - 3'

T1e = D13*+S+D2*′ (15+9+14=38mer):

5'- TGAAGGTGACGCTCT+TTTTTTTTT+C<u>T</u>TCAGCC<u>T</u>TCAGC+Cy5 - 3'

C2. 3-site track

TL = D4 + D3a + D5 + D3b + D6 + D3c (15+45+15+45+15+45=180mer):

5'-
GATTTGCTGCTTTCC+ATTGAGCCTGTTTCTCTGCGCGACGTTCGCG
GCGGCACTTACGGA+CGTGTTTGTGCATCC+ATCTGGATTCTCCTGT
CAGTTAGCTTTGGTGGTGTACCTTCTGCT+GTGGCAGTTGTAGTC+C
TGAACGAAAACCTCCAGCGATTGGCACATTGGCACTTCAGGGCT-3'

F2aL = D3a* + D1* (45+6=51mer)

5'-TCCGTAAGTGCCGCCGCGAACGTCGCGCAGAGAAACAGGCTCA
AT+AGTTTA-3'

F2bL = D3b* + D1* (45+6=51mer):

5'-AGCAGAAGGTACACCACCAAAGCTAACTGACAGGAGAATCCAG
AT+AGTTTA-3'

F2cL = D3c* + D1* (45+6=51mer):

5'-AGCCCTGAAGTGCCAATGTGCCAATCGCTGGAGGTTTTCGTTCA
G+AGTTTA-3'

F1a = D4* + S + D2*′ (15+9+14=38mer):

5'- GGAAAGCAGCAAATC+TTTTTTTTT+CTTCAGCCTTCAGC+FAM-3'

F1b = D5* + S + D2*′ (15+9+14=38mer):

5'- GGATGCACAAACACG+TTTTTTTTT+CTTCAGCCTTCAGC+TYE-3'

F1c = D6* + S + D2*′ (15+9+14=38mer):

5'- GACTACAACTGCCAC+TTTTTTTTT+CTTCAGCCTTCAGC+CY5-3'

C3. 2-site track used for the dissociation experiment (Figure 4.12C)

The track was assembled from strands F1b, F1c, F2bL, F2cL with the template
TL replaced by a truncated strand TBSTL

TBSTL = D5-D3b-D6-D3c (15+45+15+45=120mer):

5'-CGTGTTTGTGCATCC+ATCTGGATTCTCCTGTCAGTTAGCTTTGG
TGGTGTACCTTCTGCT+GTGGCAGTTGTAGTC+CTGAACGAAAACCT
CCAGCGATTGGCACATTGGCACTTCAGGGCT - 3'

C4. Mutated 3-site track for the forward binding experiment (Figure 4.13B, C)

The track has its F1b replaced by a mutated sequence F1bM

F1bM = D5*-S-SD* (15+9+14=38mer):

5'-GGATGCACAAACACG+TTTTTTTTT+CCCATGCATACCGCC+TYE-
3'

Chapter 5 Conclusions and Outlook

5.1 Conclusions

Artificial nanomotors have been developed to mimic the dynamical aspects of biological motor proteins, and their nanotechnological applications are actively pursued. One strategy to advance energy technology and nanotechnology is to replicate the efficient chemical energy utilization in biomotors. Biomotors achieve directional and processive movement through gating mechanisms that coordinate the mechanochemical cycles of the motor's two legs. Particularly important are two controls associated with the gating mechanisms; one is ratchet-like passive control (leg dissociation bias) and the other is power-stroke-like active control (leg binding bias). Biomotors often integrate the two controls to ensure their directionality and this synergic active-plus-passive control is critical to the efficient utilization of energy.

However, it remains a challenge to integrate the two differing types of controls in rationally designed nanomotor systems. Recently a light-powered track-walking DNA nanomotor was developed from a bioinspired design principle that has the potential to integrate both controls. However, it is difficult to separate experimental signals for either control due to a tight coupling of both controls. Here we presented a systematic study of the motor

and new derivatives using multiple fluorescence labeling and specially designed light operations. The experimental data suggest that the motor achieves the two controls autonomously through a mechanics-mediated symmetry breaking. This study presents an experimental validation for the bioinspired design principle of mechanical breaking of symmetry for synergic ratchet-plus-power stroke control. Using the rationally designed DNA motor as a model system and augmenting the data with mechanical modeling, this study provides valuable mechanistic insights that may help advance molecular controls in future nanotechnological systems.

A bio-mimicking enzymatic nanowalker is developed in the second study which brings artificial nanomotors to within striking distance of the biological counterparts designed by Nature herself, and offers rich mechanistic insights into how pure physical effects enable effective harvest of chemical energy at the single-molecule level. This rationally designed motor realizes in a conceptually transparent way three gating-like controls over the fuel reaction and mechanical motion, which closely resemble those of bio-walkers (e.g., myosin V (*76*, *86*), kinesin (*62*, *69*, *71*)) crucial for their efficient fuel use and sustainable motion. The motor breaks the 50% fidelity threshold for fuel-driven motion and powers two complementary directional biases by a single fuel molecule but at different stages of its consumption, thereby controls the release of the chemical energy and effectively channels the chemical energy into productive forward motion before its decay into random heat. The

demonstration of this efficient enzymatic motor and its sustainable motion along a double-stranded track is also a step towards replicating the motor-based repeatable, efficient and automatic transport seen in biological intracellular transport but beyond the capacity of current burn-bridge motors.

5.2   Limitations and Recommendations for future study

The motors in this study have been demonstrated on duplex DNA tracks no longer than six binding sites. Longer and more rigid tracks should be used for further development of these motor systems for long range transport. A good candidate is DNA origami (*22*, *26*, *27*, *96*, *98*, *103*) as have been employed for several nanomotors reported. Moreover, linkage of origami tiles to produce long track for motor operation has also been demonstrated (*98*). This method could potentially enable multiple motor functionalities as each tile can be prepared separately, which is important for future applications. The motors from this study are also suitable for collective transport by a tandem of motors along a long track, which is demonstrated routinely by biomotors but is impossible for burn-bridge motors.

The maximum speed achieved by our motors is ~3nm/s, which is already acceptable for many applications. However, it is still ~ 20 times lower than the fastest burn-bridge motor (*102*). Detailed study is needed to reveal the rate-limiting substeps. One rate-limiting factor noted by us is the slow turnover rate (~ 4.5 minutes per turnover (*145*)) of the enzyme used in this

study. This can be improved by using other enzymes with high turnover rates. For example, nicking enzyme Nt. AlwI has a turnover rate as high as ~30s per turnover (*165*). Another possibility is integrating DNAzymes into the motor legs. In this case, external enzyme is no longer needed and the motor itself acts as the enzyme. The effects of several key parameters on the DNAzymes' kinetics have been studied in details (*102*), which may offer great tunability and controllability of the motor.

The characterization methods used in this study (ie. fluorescence measurement and gel electrophoresis) are ensemble methods. To better understand dynamics and mechanisms of the motors, single molecule studies are needed. Future endeavours should also include developing new mechanisms to achieve a better control of the motor, which is critical to improve its performance, such as speed, directionality and efficiency.

Bibliography

1. K. E. Drexler, Engines of Creation. *London: 4th Estate*, 1990.

2. R. Baum, Drexler and Smalley make the case for and against 'molecular assemblers'. *Chem. Eng. News*. **81**, 37–42 (2003).

3. P. L. Anelli, N. Spencer, J. F. Stoddart, A molecular shuttle. *J. Am. Chem. Soc.* **113**, 5131–5133 (1991).

4. H. Murakami, A. Kawabuchi, K. Kotoo, M. Kunitake, N. Nakashima, A Light-Driven Molecular Shuttle Based on a Rotaxane. *J. Am. Chem. Soc.* **119**, 7605–7606 (1997).

5. A. M. Brouwer *et al.*, Photoinduction of Fast, Reversible Translational Motion in a Hydrogen-Bonded Molecular Shuttle. *Science*. **291**, 2124–2128 (2001).

6. V. Balzani *et al.*, Autonomous artificial nanomotor powered by sunlight. *Proc. Natl. Acad. Sci.* **103**, 1178–1183 (2006).

7. N. Koumura, R. W. J. Zijlstra, R. A. van Delden, N. Harada, B. L. Feringa, Light-driven monodirectional molecular rotor. *Nature*. **401**, 152–155 (1999).

8. T. R. Kelly, H. De Silva, R. A. Silva, Unidirectional rotary motion in a molecular system. *Nature*. **401**, 150–152 (1999).

9. J. V. Hernández, E. R. Kay, D. A. Leigh, A Reversible Synthetic Rotary Molecular Motor. *Science*. **306**, 1532–1537 (2004).

10. S. P. Fletcher, F. Dumur, M. M. Pollard, B. L. Feringa, A Reversible, Unidirectional Molecular Rotary Motor Driven by Chemical Energy. *Science*. **310**, 80–82 (2005).

11. W. B. Sherman, N. C. Seeman, A Precisely Controlled DNA Biped Walking Device. *Nano Lett.* **4**, 1203–1207 (2004).

12. J.-S. Shin, N. A. Pierce, A Synthetic DNA Walker for Molecular Transport. *J. Am. Chem. Soc.* **126**, 10834–10835 (2004).

13. P. Yin, H. Yan, X. G. Daniell, A. J. Turberfield, J. H. Reif, A Unidirectional DNA Walker That Moves Autonomously along a Track. *Angew. Chem. Int. Ed.* **43**, 4906–4911 (2004).

14. J. Bath, S. J. Green, A. J. Turberfield, A Free-Running DNA Motor Powered by a Nicking Enzyme. *Angew. Chem. Int. Ed.* **44**, 4358–4361 (2005).

15. Y. Tian, Y. He, Y. Chen, P. Yin, C. Mao, A DNAzyme That Walks Processively and Autonomously along a One-Dimensional Track. *Angew. Chem. Int. Ed.* **44**, 4355–4358 (2005).

16. S. J. Green, J. Bath, A. J. Turberfield, Coordinated Chemomechanical Cycles: A Mechanism for Autonomous Molecular Motion. *Phys. Rev. Lett.* **101**, 238101 (2008).

17. T. Omabegho, R. Sha, N. C. Seeman, A Bipedal DNA Brownian Motor with Coordinated Legs. *Science*. **324**, 67–71 (2009).

18. J. Bath, S. J. Green, K. E. Allen, A. J. Turberfield, Mechanism for a Directional, Processive, and Reversible DNA Motor. *Small*. **5**, 1513–1516 (2009).

19. M. von Delius, E. M. Geertsema, D. A. Leigh, A synthetic small molecule that can walk down a track. *Nat. Chem.* **2**, 96–101 (2010).

20. M. J. Barrell, A. G. Campaña, M. von Delius, E. M. Geertsema, D. A. Leigh, Light-Driven Transport of a Molecular Walker in Either Direction along a Molecular Track. *Angew. Chem. Int. Ed.* **50**, 285–290 (2011).

21. R. A. Muscat, J. Bath, A. J. Turberfield, A Programmable Molecular Robot. *Nano Lett.* **11**, 982–987 (2011).

22. S. F. J. Wickham *et al.*, Direct observation of stepwise movement of a synthetic molecular transporter. *Nat. Nanotechnol.* **6**, 166–169 (2011).

23. M. You *et al.*, An Autonomous and Controllable Light-Driven DNA Walking Device. *Angew. Chem. Int. Ed.* **51**, 2457–2460 (2012).

24. J. Cheng *et al.*, Bipedal Nanowalker by Pure Physical Mechanisms. *Phys. Rev. Lett.* **109**, 238104 (2012).

25. I. Y. Loh, J. Cheng, S. R. Tee, A. Efremov, Z. Wang, From Bistate Molecular Switches to Self-Directed Track-Walking Nanomotors. *ACS Nano*. **8**, 10293–10304 (2014).

26. H. Gu, J. Chao, S.-J. Xiao, N. C. Seeman, A proximity-based programmable DNA nanoscale assembly line. *Nature*. **465**, 202–205 (2010).

27. K. Lund *et al.*, Molecular robots guided by prescriptive landscapes. *Nature*. **465**, 206–210 (2010).

28. Y. He, D. R. Liu, Autonomous multistep organic synthesis in a single isothermal solution mediated by a DNA walker. *Nat. Nanotechnol.* **5**, 778–782 (2010).

29. B. Lewandowski *et al.*, Sequence-Specific Peptide Synthesis by an Artificial Small-Molecule Machine. *Science*. **339**, 189–193 (2013).

30. H. L. Tierney *et al.*, Experimental demonstration of a single-molecule electric motor. *Nat. Nanotechnol.* **6**, 625–629 (2011).

31. N. Hirokawa, Kinesin and Dynein Superfamily Proteins and the Mechanism of Organelle Transport. *Science*. **279**, 519–526 (1998).

32. R. D. Vale, R. A. Milligan, The Way Things Move: Looking Under the Hood of Molecular Motor Proteins. *Science*. **288**, 88–95 (2000).

33. M. Schliwa, G. Woehlke, Molecular motors. *Nature*. **422**, 759–765 (2003).

34. D. A. Leigh, U. Lewandowska, B. Lewandowski, M. R. Wilson, Synthetic molecular walkers. *Top. Curr. Chem.* **354**, 111–138 (2014).

35. J. Rousselet, L. Salome, A. Ajdari, J. Prostt, Directional motion of brownian particles induced by a periodic asymmetric potential. *Nature*. **370**, 446–447 (1994).

36. R. D. Astumian, Thermodynamics and Kinetics of a Brownian Motor. *Science*. **276**, 917–922 (1997).

37. P. Reimann, Brownian motors: noisy transport far from equilibrium. *Phys. Rep.* **361**, 57–265 (2002).

38. J. Howard, Protein power strokes. *Curr. Biol.* **16**, R517–R519 (2006).

39. H. Linke *et al.*, Experimental Tunneling Ratchets. *Science*. **286**, 2314–2317 (1999).

40. S. Saffarian, I. E. Collier, B. L. Marmer, E. L. Elson, G. Goldberg, Interstitial Collagenase Is a Brownian Ratchet Driven by Proteolysis of Collagen. *Science*. **306**, 108–111 (2004).

41. S.-H. Lee, K. Ladavac, M. Polin, D. G. Grier, Observation of Flux Reversal in a Symmetric Optical Thermal Ratchet. *Phys. Rev. Lett.* **94**, 110601 (2005).

42. A. Yildiz, M. Tomishige, R. D. Vale, P. R. Selvin, Kinesin Walks Hand-Over-Hand. *Science*. **303**, 676–678 (2004).

43. W. Hua, E. C. Young, M. L. Fleming, J. Gelles, Coupling of kinesin steps to ATP hydrolysis. *Nature*. **388**, 390–393 (1997).

44. D. L. Coy, M. Wagenbach, J. Howard, Kinesin Takes One 8-nm Step for Each ATP That It Hydrolyzes. *J. Biol. Chem.* **274**, 3667–3671 (1999).

45. M. J. Schnitzer, S. M. Block, Kinesin hydrolyses one ATP per 8-nm step. *Nature*. **388**, 386–390 (1997).

46. S. M. Block, L. S. B. Goldstein, B. J. Schnapp, Bead movement by single kinesin molecules studied with optical tweezers. *Nature*. **348**, 348–352 (1990).

47. R. D. Vale *et al.*, Direct observation of single kinesin molecules moving along microtubules. *Nature*. **380**, 451–453 (1996).

48. K. Svoboda, S. M. Block, Force and velocity measured for single kinesin molecules. *Cell*. **77**, 773–784 (1994).

49. S. M. Block, Nanometres and piconewtons: the macromolecular mechanics of kinesin. *Trends Cell Biol.* **5**, 169–175 (1995).

50. M. Nishiyama, H. Higuchi, T. Yanagida, Chemomechanical coupling of the forward and backward steps of single kinesin molecules. *Nat. Cell Biol.* **4**, 790–797 (2002).

51. N. J. Carter, R. A. Cross, Mechanics of the kinesin step. *Nature*. **435**, 308–312 (2005).

52. C. Hyeon, J. N. Onuchic, Internal strain regulates the nucleotide binding site of the kinesin leading head. *Proc. Natl. Acad. Sci.* **104**, 2175–2180 (2007).

53. A. Yildiz, M. Tomishige, A. Gennerich, R. D. Vale, Intramolecular Strain Coordinates Kinesin Stepping Behavior along Microtubules. *Cell*. **134**, 1030–1041 (2008).

54. S. Toyabe, T. Watanabe-Nakayama, T. Okamoto, S. Kudo, E. Muneyuki, Thermodynamic efficiency and mechanochemical coupling of F1-ATPase. *Proc. Natl. Acad. Sci.* **108**, 17951–17956 (2011).

55. M. von Delius, D. A. Leigh, Walking molecules. *Chem. Soc. Rev.* **40**, 3656–3676 (2011).

56. S. M. Block, Kinesin Motor Mechanics: Binding, Stepping, Tracking, Gating, and Limping. *Biophys. J.* **92**, 2986–2995 (2007).

57. W. O. Hancock, J. Howard, Kinesin's processivity results from mechanical and chemical coordination between the ATP hydrolysis cycles of the two motor domains. *Proc. Natl. Acad. Sci.* **96**, 13147–13152 (1999).

58. W. R. Schief, R. H. Clark, A. H. Crevenna, J. Howard, Inhibition of kinesin motility by ADP and phosphate supports a hand-over-hand mechanism. *Proc. Natl. Acad. Sci. U. S. A.* **101**, 1183–1188 (2004).

59. I. M.-T. Crevel *et al.*, What kinesin does at roadblocks: the coordination mechanism for molecular walking. *EMBO J.* **23**, 23–32 (2004).

60. T. Mori, R. D. Vale, M. Tomishige, How kinesin waits between steps. *Nature*. **450**, 750–754 (2007).

61. E. Toprak, A. Yildiz, M. T. Hoffman, S. S. Rosenfeld, P. R. Selvin, Why kinesin is so processive. *Proc. Natl. Acad. Sci.* **106**, 12717–12722 (2009).

62. Z. Wang, M. Feng, W. Zheng, D. Fan, Kinesin Is an Evolutionarily Fine-Tuned Molecular Ratchet-and-Pawl Device of Decisively Locked Direction. *Biophys. J.* **93**, 3363–3372 (2007).

63. S. S. Rosenfeld, P. M. Fordyce, G. M. Jefferson, P. H. King, S. M. Block, Stepping and Stretching HOW KINESIN USES INTERNAL STRAIN TO WALK PROCESSIVELY. *J. Biol. Chem.* **278**, 18550–18556 (2003).

64. L. M. Klumpp, A. Hoenger, S. P. Gilbert, Kinesin's second step. *Proc. Natl. Acad. Sci. U. S. A.* **101**, 3444–3449 (2004).

65. N. R. Guydosh, S. M. Block, Backsteps induced by nucleotide analogs suggest the front head of kinesin is gated by strain. *Proc. Natl. Acad. Sci.* **103**, 8054–8059 (2006).

66. S. Rice *et al.*, A structural change in the kinesin motor protein that drives motility. *Nature*. **402**, 778–784 (1999).

67. S. Rice *et al.*, Thermodynamic Properties of the Kinesin Neck-Region Docking to the Catalytic Core. *Biophys. J.* **84**, 1844–1854 (2003).

68. Y. Taniguchi, M. Nishiyama, Y. Ishii, T. Yanagida, Entropy rectifies the Brownian steps of kinesin. *Nat. Chem. Biol.* **1**, 342–347 (2005).

69. D. D. Hackney, Evidence for alternating head catalysis by kinesin during microtubule-stimulated ATP hydrolysis. *Proc. Natl. Acad. Sci.* **91**, 6865–6869 (1994).

70. Y. Z. Ma, E. W. Taylor, Interacting head mechanism of microtubule-kinesin ATPase. *J. Biol. Chem.* **272**, 724–730 (1997).

71. A. Gennerich, R. D. Vale, Walking the walk: how kinesin and dynein coordinate their steps. *Curr. Opin. Cell Biol.* **21**, 59–67 (2009).

72. S. Uemura, S. 'ichi Ishiwata, Loading direction regulates the affinity of ADP for kinesin. *Nat. Struct. Mol. Biol.* **10**, 308–311 (2003).

73. B. E. Clancy, W. M. Behnke-Parks, J. O. L. Andreasson, S. S. Rosenfeld, S. M. Block, A universal pathway for kinesin stepping. *Nat. Struct. Mol. Biol.* **18**, 1020–1027 (2011).

74. A. D. Mehta *et al.*, Myosin-V is a processive actin-based motor. *Nature.* **400**, 590–593 (1999).

75. C. Veigel, F. Wang, M. L. Bartoo, J. R. Sellers, J. E. Molloy, The gated gait of the processive molecular motor, myosin V. *Nat. Cell Biol.* **4**, 59–65 (2002).

76. R. D. Vale, Myosin V motor proteins: marching stepwise towards a mechanism. *J. Cell Biol.* **163**, 445–450 (2003).

77. M. Rief *et al.*, Myosin-V stepping kinetics: A molecular model for processivity. *Proc. Natl. Acad. Sci.* **97**, 9482–9486 (2000).

78. S. Uemura, H. Higuchi, A. O. Olivares, E. M. De La Cruz, S. 'ichi Ishiwata, Mechanochemical coupling of two substeps in a single myosin V motor. *Nat. Struct. Mol. Biol.* **11**, 877–883 (2004).

79. G. Cappello *et al.*, Myosin V stepping mechanism. *Proc. Natl. Acad. Sci.* **104**, 15328–15333 (2007).

80. T. Sakamoto, M. R. Webb, E. Forgacs, H. D. White, J. R. Sellers, Direct observation of the mechanochemical coupling in myosin Va during processive movement. *Nature.* **455**, 128–132 (2008).

81. K. Fujita, M. Iwaki, A. H. Iwane, L. Marcucci, T. Yanagida, Switching of myosin-V motion between the lever-arm swing and Brownian search-and-catch. *Nat. Commun.* **3**, 956 (2012).

82. J. N. Forkey, M. E. Quinlan, M. Alexander Shaw, J. E. T. Corrie, Y. E. Goldman, Three-dimensional structural dynamics of myosin V by single-molecule fluorescence polarization. *Nature.* **422**, 399–404 (2003).

83. A. Yildiz *et al.*, Myosin V walks hand-over-hand: single fluorophore imaging with 1.5-nm localization. *Science.* **300**, 2061–2065 (2003).

84. A. Vilfan, Five models for myosin V. *Front. Biosci.* **14**, 2269-2284 (2009).

85. C. Veigel, S. Schmitz, F. Wang, J. R. Sellers, Load-dependent kinetics of myosin-V can explain its high processivity. *Nat. Cell Biol.* **7**, 861–869 (2005).

86. Y. Xu, Z. Wang, Comprehensive physical mechanism of two-headed biomotor myosin V. *J. Chem. Phys.* **131**, 245104 (2009).

87. K. Shiroguchi, K. Kinosita, Myosin V Walks by Lever Action and Brownian Motion. *Science.* **316**, 1208–1212 (2007).

88. S. S. Rosenfeld, H. L. Sweeney, A Model of Myosin V Processivity. *J. Biol. Chem.* **279**, 40100–40111 (2004).

89. E. M. D. L. Cruz, A. L. Wells, S. S. Rosenfeld, E. M. Ostap, H. L. Sweeney, The kinetic mechanism of myosin V. *Proc. Natl. Acad. Sci.* **96**, 13726–13731 (1999).

90. T. J. Purcell, H. L. Sweeney, J. A. Spudich, A force-dependent state controls the coordination of processive myosin V. *Proc. Natl. Acad. Sci. U. S. A.* **102**, 13873–13878 (2005).

91. E. Forgacs *et al.*, Kinetics of ADP Dissociation from the Trail and Lead Heads of Actomyosin V following the Power Stroke. *J. Biol. Chem.* **283**, 766–773 (2008).

92. Y. Oguchi *et al.*, Load-dependent ADP binding to myosins V and VI: Implications for subunit coordination and function. *Proc. Natl. Acad. Sci.* **105**, 7714–7719 (2008).

93. J. Pan, F. Li, T.-G. Cha, H. Chen, J. H. Choi, Recent progress on DNA based walkers. *Curr. Opin. Biotechnol.* **34**, 56–64 (2015).

94. D. A. Leigh, U. Lewandowska, B. Lewandowski, M. R. Wilson, Synthetic molecular walkers. Top. Curr. Chem. 354, 111–138 (2014).

95. Y. Chen, Y. Xiang, R. Yuan, Y. Chai, A restriction enzyme-powered autonomous DNA walking machine: its application for a highly sensitive electrochemiluminescence assay of DNA. *Nanoscale*. **7**, 981–986 (2014).

96. T. E. Tomov *et al.*, Rational Design of DNA Motors: Fuel Optimization through Single-Molecule Fluorescence. *J. Am. Chem. Soc.* **135**, 11935–11941 (2013).

97. C. Wang, Y. Tao, G. Song, J. Ren, X. Qu, Speeding Up a Bidirectional DNA Walking Device. *Langmuir*. **28**, 14829–14837 (2012).

98. M. Liber, T. E. Tomov, R. Tsukanov, Y. Berger, E. Nir, A Bipedal DNA Motor that Travels Back and Forth between Two DNA Origami Tiles. *Small*. **11**, 568–575 (2015).

99. Z.-G. Wang, J. Elbaz, I. Willner, DNA Machines: Bipedal Walker and Stepper. *Nano Lett.* **11**, 304–309 (2011).

100. R. Pei *et al.*, Behavior of Polycatalytic Assemblies in a Substrate-Displaying Matrix. *J. Am. Chem. Soc.* **128**, 12693–12699 (2006).

101. T.-G. Cha *et al.*, A synthetic DNA motor that transports nanoparticles along carbon nanotubes. *Nat. Nanotechnol.* **9**, 39–43 (2014).

102. T.-G. Cha *et al.*, Design Principles of DNA Enzyme-Based Walkers: Translocation Kinetics and Photoregulation. *J. Am. Chem. Soc.* **137**, 9429–9437 (2015).

103. Y. Yang *et al.*, Direct Visualization of Walking Motions of Photocontrolled Nanomachine on the DNA Nanostructure. *Nano Lett.* **15**, 6672–6676 (2015).

104. P. Yin, H. M. T. Choi, C. R. Calvert, N. A. Pierce, Programming biomolecular self-assembly pathways. *Nature*. **451**, 318–322 (2008).

105. R. Masoud *et al.*, Studying the Structural Dynamics of Bipedal DNA Motors with Single-Molecule Fluorescence Spectroscopy. *ACS Nano*. **6**, 6272–6283 (2012).

106. R. A. Muscat, J. Bath, A. J. Turberfield, Small Molecule Signals that Direct the Route of a Molecular Cargo. *Small*. **8**, 3593–3597 (2012).

107.   M. Liu *et al.*, Autonomous Synergic Control of Nanomotors. *ACS Nano*. **8**, 1792–1803 (2014).

108.   J. Cheng, S. Sreelatha, I. Y. Loh, M. Liu, Z. Wang, A bioinspired design principle for DNA nanomotors: Mechanics-mediated symmetry breaking and experimental demonstration. *Methods*. **67**, 227–233 (2014).

109.   M. von Delius, E. M. Geertsema, D. A. Leigh, D.-T. D. Tang, Design, Synthesis, and Operation of Small Molecules That Walk along Tracks. *J. Am. Chem. Soc.* **132**, 16134–16145 (2010).

110.   E. R. Kay, D. A. Leigh, F. Zerbetto, Synthetic Molecular Motors and Mechanical Machines. *Angew. Chem. Int. Ed.* **46**, 72–191 (2007).

111.   E. R. Kay, D. A. Leigh, Rise of the Molecular Machines. *Angew. Chem. Int. Ed.* **54**, 10080–10088 (2015).

112.   S. Erbas-Cakmak, D. A. Leigh, C. T. McTernan, A. L. Nussbaumer, Artificial Molecular Machines. *Chem. Rev.* **115**, 10081–10206 (2015).

113.   J. M. Abendroth, O. S. Bushuyev, P. S. Weiss, C. J. Barrett, Controlling Motion at the Nanoscale: Rise of the Molecular Machines. *ACS Nano*. **9**, 7746–7768 (2015).

114.   K. Gehring, J.-L. Leroy, M. Guéron, A tetrameric DNA structure with protonated cytosine-cytosine base pairs. *Nature*. **363**, 561–565 (1993).

115.   Y. Dong, Z. Yang, D. Liu, DNA Nanotechnology Based on i-Motif Structures. *Acc. Chem. Res.* **47**, 1853–1860 (2014).

116.   P. Alberti, J.-L. Mergny, DNA duplex–quadruplex exchange as the basis for a nanomolecular machine. *Proc. Natl. Acad. Sci.* **100**, 1569–1573 (2003).

117.   M. L. Bochman, K. Paeschke, V. A. Zakian, DNA secondary structures: stability and function of G-quadruplex structures. *Nat. Rev. Genet.* **13**, 770–780 (2012).

118.   B. Yurke, A. J. Turberfield, A. P. Mills, F. C. Simmel, J. L. Neumann, A DNA-fuelled molecular machine made of DNA. *Nature*. **406**, 605–608 (2000).

119.   D. Y. Zhang, G. Seelig, Dynamic DNA nanotechnology using strand-displacement reactions. *Nat. Chem.* **3**, 103–113 (2011).

120. A. J. Turberfield *et al.*, DNA Fuel for Free-Running Nanomachines. *Phys. Rev. Lett.* **90**, 118102 (2003).

121. S. J. Green, D. Lubrich, A. J. Turberfield, DNA Hairpins: Fuel for Autonomous DNA Devices. *Biophys. J.* **91**, 2966–2975 (2006).

122. G. Seelig, B. Yurke, E. Winfree, Catalyzed Relaxation of a Metastable DNA Fuel. *J. Am. Chem. Soc.* **128**, 12211–12220 (2006).

123. Z. Wang, Synergic mechanism and fabrication target for bipedal nanomotors. *Proc. Natl. Acad. Sci.* **104**, 17921–17926 (2007).

124. G. Oster, H. Wang, Reverse engineering a protein: the mechanochemistry of ATP synthase. *Biochim. Biophys. Acta BBA - Bioenerg.* **1458**, 482–510 (2000).

125. R. F. Fox, Rectified Brownian movement in molecular and cell biology. *Phys. Rev. E.* **57**, 2177–2203 (1998).

126. W. H. Mather, R. F. Fox, Kinesin's Biased Stepping Mechanism: Amplification of Neck Linker Zippering. *Biophys. J.* **91**, 2416–2426 (2006).

127. A. Efremov, Z. Wang, Maximum directionality and systematic classification of molecular motors. *Phys. Chem. Chem. Phys.* **13**, 5159–5170 (2011).

128. Z. Wang, R. Hou, A. Efremov, Directional fidelity of nanoscale motors and particles is limited by the 2nd law of thermodynamics—Via a universal equality. *J. Chem. Phys.* **139**, 035105 (2013).

129. R. Hou, Z. Wang, Role of directional fidelity in multiple aspects of extreme performance of the F_{1}-ATPase motor. *Phys. Rev. E.* **88**, 022703 (2013).

130. U. Feldkamp, CANADA: Designing nucleic acid sequences for nanobiotechnology applications. *J. Comput. Chem.* **31**, 660–663 (2010).

131. M. Zuker, Mfold web server for nucleic acid folding and hybridization prediction. *Nucleic Acids Res.* **31**, 3406–3415 (2003).

132. J. N. Zadeh *et al.*, NUPACK: Analysis and design of nucleic acid systems. *J. Comput. Chem.* **32**, 170–173 (2011).

133. J. Sager, D. Stefanovic, Designing nucleotide sequences for computation: a survey of constraints. *DNA Computing*, **3892**, 275–289. Springer Berlin Heidelberg, 2006.

134. M. Zuker, P. Stiegler, Optimal computer folding of large RNA sequences using thermodynamics and auxiliary information. *Nucleic Acids Res.* **9**, 133–148 (1981).

135. R. M. Dirks, J. S. Bois, J. M. Schaeffer, E. Winfree, N. A. Pierce, Thermodynamic Analysis of Interacting Nucleic Acid Strands. *SIAM Rev.* **49**, 65–88 (2007).

136. H. Asanuma *et al.*, Synthesis of azobenzene-tethered DNA for reversible photo-regulation of DNA functions: hybridization and transcription. *Nat. Protoc.* **2**, 203–212 (2007).

137. X. Liang *et al.*, NMR Study on the Photoresponsive DNA Tethering an Azobenzene. Assignment of the Absolute Configuration of Two Diastereomers and Structure Determination of Their Duplexes in the trans-Form. *J. Am. Chem. Soc.* **125**, 16408–16415 (2003).

138. H. M. D. Bandara, S. C. Burdette, Photoisomerization in different classes of azobenzene. *Chem. Soc. Rev.* **41**, 1809–1825 (2012).

139. H. Rau, E. Lueddecke, On the rotation-inversion controversy on photoisomerization of azobenzenes. Experimental proof of inversion. *J. Am. Chem. Soc.* **104**, 1616–1620 (1982).

140. H. Asanuma, T. Ito, T. Yoshida, X. Liang, M. Komiyama, Photoregulation of the Formation and Dissociation of a DNA Duplex by Using the cis–trans Isomerization of Azobenzene. *Angew. Chem. Int. Ed.* **38**, 2393–2395 (1999).

141. H. Asanuma *et al.*, Enantioselective Incorporation of Azobenzenes into Oligodeoxyribonucleotide for Effective Photoregulation of Duplex Formation. *Angew. Chem.* **113**, 2743–2745 (2001).

142. H. Asanuma, D. Matsunaga, M. Komiyama, Clear-cut photo-regulation of the formation and dissociation of the DNA duplex by modified oligonucleotide involving multiple azobenzenes. *Nucleic Acids Symp. Ser.* **49**, 35–36 (2005).

143. X. Liang, T. Mochizuki, H. Asanuma, A Supra-photoswitch Involving Sandwiched DNA Base Pairs and Azobenzenes for Light-Driven Nanostructures and Nanodevices. *Small*. **5**, 1761–1768 (2009).

144. D. F. Heiter, K. D. Lunnen, G. G. Wilson, Site-Specific DNA-nicking Mutants of the Heterodimeric Restriction Endonuclease R.BbvCI. *J. Mol. Biol.* **348**, 631–640 (2005).

145. S. R. W. Bellamy *et al.*, Cleavage of Individual DNA Strands by the Different Subunits of the Heterodimeric Restriction Endonuclease BbvCI. *J. Mol. Biol.* **348**, 641–653 (2005).

146. K. S. Dickson, C. M. Burns, J. P. Richardson, Determination of the Free-Energy Change for Repair of a DNA Phosphodiester Bond. *J. Biol. Chem.* **275**, 15828–15831 (2000).

147. I. Muiznieks, W. Doerfler, DNA fragments with specific nucleotide sequences in their single-stranded termini exhibit unusual electrophoretic mobilities. *Nucleic Acids Res.* **26**, 1899–1905 (1998).

148. Q. Liu, W. A. Scaringe, S. S. Sommer, Discrete mobility of single-stranded DNA in non-denaturing gel electrophoresis. *Nucleic Acids Res.* **28**, 940–943 (2000).

149. A. Efremov, Z. Wang, Universal optimal working cycles of molecular motors. *Phys. Chem. Chem. Phys.* **13**, 6223–6233 (2011).

150. R. Yasuda, H. Noji, K. Kinosita, M. Yoshida, F1-ATPase Is a Highly Efficient Molecular Motor that Rotates with Discrete 120° Steps. *Cell*. **93**, 1117–1124 (1998).

151. L. P. Faucheux, L. S. Bourdieu, P. D. Kaplan, A. J. Libchaber, Optical Thermal Ratchet. *Phys. Rev. Lett.* **74**, 1504–1507 (1995).

152. J. B. Mills, E. Vacano, P. J. Hagerman, Flexibility of single-stranded DNA: use of gapped duplex helices to determine the persistence lengths of Poly(dT) and Poly(dA)1. *J. Mol. Biol.* **285**, 245–257 (1999).

153. S. A. E. Marras, F. R. Kramer, S. Tyagi, Efficiencies of fluorescence resonance energy transfer and contact-mediated quenching in oligonucleotide probes. *Nucleic Acids Res.* **30**, e122 (2002).

154. J. SantaLucia, A unified view of polymer, dumbbell, and oligonucleotide DNA nearest-neighbor thermodynamics. *Proc. Natl. Acad. Sci.* **95**, 1460–1465 (1998).

155. M. C. Murphy, I. Rasnik, W. Cheng, T. M. Lohman, T. Ha, Probing Single-Stranded DNA Conformational Flexibility Using Fluorescence Spectroscopy. *Biophys. J.* **86**, 2530–2537 (2004).

156. R. D. Astumian, Irrelevance of the Power Stroke for the Directionality, Stopping Force, and Optimal Efficiency of Chemically Driven Molecular Machines. *Biophys. J.* **108**, 291–303 (2015).

157. S. K. Kufer, E. M. Puchner, H. Gumpp, T. Liedl, H. E. Gaub, Single-Molecule Cut-and-Paste Surface Assembly. *Science*. **319**, 594–596 (2008).

158. G. Varani, Exceptionally Stable Nucleic Acid Hairpins. *Annu. Rev. Biophys. Biomol. Struct.* **24**, 379–404 (1995).

159. P. J. Hagerman, Flexibility of DNA. *Annu. Rev. Biophys. Biophys. Chem.* **17**, 265–286 (1988).

160. T. E. Ouldridge *et al.*, Optimizing DNA Nanotechnology through Coarse-Grained Modeling: A Two-Footed DNA Walker. *ACS Nano*. **7**, 2479–2490 (2013).

161. P. Šulc *et al.*, Sequence-dependent thermodynamics of a coarse-grained DNA model. *J. Chem. Phys.* **137**, 135101 (2012).

162. D. M. Gowers, G. G. Wilson, S. E. Halford, Measurement of the contributions of 1D and 3D pathways to the translocation of a protein along DNA. *Proc. Natl. Acad. Sci. U. S. A.* **102**, 15883–15888 (2005).

163. S. B. Smith, Y. Cui, C. Bustamante, Overstretching B-DNA: The Elastic Response of Individual Double-Stranded and Single-Stranded DNA Molecules. *Science*. **271**, 795–799 (1996).

164. O. A. Saleh, D. B. McIntosh, P. Pincus, N. Ribeck, Nonlinear low-force elasticity of single-stranded DNA molecules. *Phys. Rev. Lett.* **102**, 068301 (2009).

165. Y. Xu, K. D. Lunnen, H. Kong, Engineering a nicking endonuclease N.AlwI by domain swapping. *Proc. Natl. Acad. Sci. U. S. A.* **98**, 12990–12995 (2001).